

INFORMATION TO USERS

This manuscript has been reproduced from the microfilm master. UMI films the text directly from the original or copy submitted. Thus, some thesis and dissertation copies are in typewriter face, while others may be from any type of computer printer.

The quality of this reproduction is dependent upon the quality of the copy submitted. Broken or indistinct print, colored or poor quality illustrations and photographs, print bleedthrough, substandard margins, and improper alignment can adversely affect reproduction.

In the unlikely event that the author did not send UMI a complete manuscript and there are missing pages, these will be noted. Also, if unauthorized copyright material had to be removed, a note will indicate the deletion.

Oversize materials (e.g., maps, drawings, charts) are reproduced by sectioning the original, beginning at the upper left-hand corner and continuing from left to right in equal sections with small overlaps. Each original is also photographed in one exposure and is included in reduced form at the back of the book.

Photographs included in the original manuscript have been reproduced xerographically in this copy. Higher quality 6" x 9" black and white photographic prints are available for any photographs or illustrations appearing in this copy for an additional charge. Contact UMI directly to order.

UMI

**A Bell & Howell Information Company
300 North Zeeb Road, Ann Arbor MI 48106-1346 USA
313/761-4700 800/521-0600**

Glacier Geophysics at Taylor Dome, Antarctica

by

David L. Morse

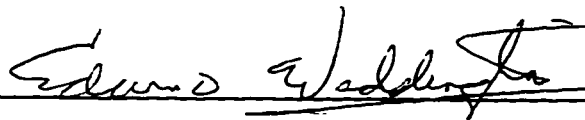
A dissertation submitted in partial fulfillment
of the requirements for the degree of

Doctor of Philosophy

University of Washington

1997

Approved by



(Chairperson of Supervisory Committee)

Program Authorized

to Offer Degree

GEOPHYSICS

Date

8/12/97

UMI Number: 9807005

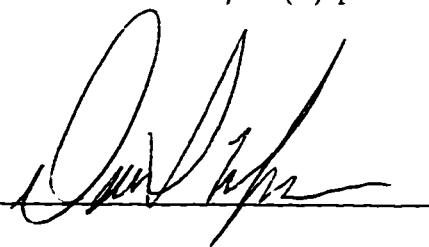
UMI Microform 9807005
Copyright 1997, by UMI Company. All rights reserved.

**This microform edition is protected against unauthorized
copying under Title 17, United States Code.**

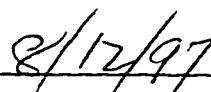
UMI
300 North Zeeb Road
Ann Arbor, MI 48103

In presenting this dissertation in partial fulfillment of the requirements for the Doctoral degree at the University of Washington, I agree that the Library shall make its copies freely available for inspection. I further agree that extensive copying of this dissertation is allowable only for scholarly purposes, consistent with "fair use" as prescribed in the U.S. Copyright Law. Requests for copying or reproduction of this dissertation may be referred to University Microfilms, 1490 Eisenhower Place, P.O. Box 975, Ann Arbor, MI 48106, to whom the author has granted "the right to reproduce and sell (a) copies of the manuscript in microform and/or (b) printed copies of the manuscript made from microform."

Signature

A handwritten signature in black ink, appearing to be "D. J. [unclear]", written over a horizontal line.

Date

A handwritten date "8/12/97" in black ink, written over a horizontal line.

University of Washington

Abstract

Glacier Geophysics at Taylor Dome, Antarctica

by David L. Morse

Chairperson of Supervisory Committee: Research Associate Professor

Edwin D. Waddington

Geophysics Program

Taylor Dome, South Victoria Land, Antarctica, is a small ice dome on a ridge which extends from Dome C to the Transantarctic Mtns. west of McMurdo Sound. At an elevation of 2374 m and centered at $77^{\circ} 47'S$ $158^{\circ} 43'E$, the dome rises more than 100 m above the saddle connecting it with the East Antarctic Ice Sheet. An ice core paleoclimate project was conducted at this site by researchers at the University of Washington. The ice core was drilled to bedrock during 1995.

In this dissertation I present glaciological analysis in support of the ice core paleoclimate project. An extensive program of geophysical surveys were conducted at Taylor Dome, much of that work is chronicled in this dissertation. Surface and bed topography from airborne radar profiling gives the regional setting. Ground-based radar profiles reveal a detailed and complex pattern of internal layering. A strain network provides surface motion data. A borehole temperature profile, along with surface temperatures and accumulation rates complete the suite of glaciological observations. In combination, these data become boundary conditions for numerical flow modeling, which in turn gives an understanding of the ice dynamics regime.

The flow modeling is used to support stratigraphic timescale estimates and geochemically determined layer thickness measurements made in the ice core. These are then combined to give an accumulation rate profile which is compared with that derived by geochemical means. Finally, the radar internal layering, taken to be isochrons, are used to extrapolate the ice core timescale to other locations in the survey region. An inferred temporal change in the spatial pattern of accumulation rate is interpreted as a reversal of storm track direction during the last glacial maximum. The timing of this reversal is related to the advance and retreat of the West Antarctic Ice Sheet.

TABLE OF CONTENTS

List of Figures	v
List of Tables	viii
Chapter 1: Introduction	1
1.1 Geographic setting	1
1.2 Motivation	3
1.3 Goals	6
Chapter 2: Ground Radar Data Collection at Taylor Dome	8
2.1 The radar system	8
2.2 System calibration	9
2.3 Grid line radar surveys at Taylor Dome	14
2.4 Flow line profiles	17
Chapter 3: Ice Deformation Survey	19
3.1 Algorithm for simultaneous solution of survey data	22
3.1.1 The medium-scale domain survey data reduction algorithm, “uvwxyz”	25
3.1.2 The large-domain survey data reduction algorithm, “UVWXYZ”	26
3.2 Formulation of observation types	27
3.3 Reduction of Taylor Dome survey data	30
3.4 The results	36

Chapter 4: Airborne Survey	39
4.1 The CASERTZ platform	39
4.2 Ice thickness map	41
4.3 Surface elevation map	42
4.3.1 Bed elevations	44
4.4 Combining ground and airborne radar data	45
Chapter 5: Ice Temperatures at Taylor Dome	47
5.1 The borehole temperature profile	48
5.2 Regional extension of the 1-D temperature model	50
5.2.1 Surface temperature	51
5.2.2 Accumulation rate	51
5.2.3 Vertical strain-rate profiles	55
5.3 The 1-D temperature field	56
Chapter 6: Inversion of Surface Velocity Field for Ice Rheological Parameters, Part 1: Model Development	58
6.1 The forward problem: finite element modeling of idealized ice divide .	62
6.2 Ice divide model setup	63
6.3 Setting up the minimization problem	64
6.4 Idealized-divide flow law parameter fitting	66
Chapter 7: Inversion of Surface Velocity Field for Flow Parameters: Part 2, Using Real Data	71
7.1 3-D temperature calculation	72
7.2 2-D stress coupling	75
7.3 Parameter inversion	76

Chapter 8: Reflections on Taylor Dome Radar Profiling	80
8.1 Core-site radar	80
8.1.1 Comparison with ice core electrical properties	84
8.1.2 Crystal fabric layers	84
8.2 Divide stability	90
Chapter 9: 2-D Plane Strain Flow Line Modeling	94
9.1 Model setup	94
9.2 Model results and ice core interpretation	98
9.3 Layer thinning profile	100
9.4 Depth-age profile	102
9.4.1 Determination of paleo-accumulation rates consistent with time scale and thinning function	104
9.4.2 Determination of thinning function consistent with time scale and geochemically-determined accumulation rates.	109
9.4.3 Thinning function for non-steady state ice thickness	112
9.4.4 Determination of accumulation rate consistent with time scale and ice sheet thickness variations	115
9.5 Discussion	115
Chapter 10: The Northern-Flank Virtual Ice Core	118
10.1 The ¹⁰ Be snow paleo-precipitation rate gauge	122
10.2 Reversal of accumulation rate spatial gradient	123
Chapter 11: Synopsis	126
11.1 Future work	128
Bibliography	129

LIST OF FIGURES

1.1	Map of Antarctica	2
1.2	Taylor Dome location map	4
1.3	Taylor Dome survey region	5
2.1	Example 5 MHz radar trace	11
2.2	Radiation pattern for loaded-dipole antenna	13
2.3	Map of Ground radar profile paths	15
2.4	2 MHz radar profile	16
2.5	Flowline parallel 7.5 MHz radar profile	18
3.1	The Taylor Dome strain network	20
3.2	Minimization of refraction correction paramater " Γ "	33
3.3	Distribution of unresolved observation discrepancies	35
3.4	Combined GPS and optical survey solution.	37
3.5	Optical survey solution	38
4.1	Airborne survey flight tracks	40
4.2	Ice thickness map	42
4.3	Bed elevation map	44
4.4	Ice thickness in core-site subregion	46
5.1	Borehole temperature profile	48
5.2	Location map of firn temperature measurement. Hatched bands separate micro-climate zones.	52

5.3	Ten-meter firn temperatures	52
5.4	Summary of accumulation rate measurements at Taylor Dome	54
5.5	Bed temperatures from 1-D calculation	57
6.1	Geometry of parallel-sided slab	60
6.2	Profiles of selected parameters for isothermal divides with $\tau_{div} \sim 0.2$ bar and different values of crossover stress.	64
6.3	Relative sensitivity of the velocity misfit parameter to the model param- eters	66
6.4	Surface horizontal velocity discrepancies for four flow law parameter inversions	69
7.1	Location map for flow law parameter inversions	73
7.2	Map-view geometry for 2-D spatial averaging	75
7.3	Surface velocities from motion survey compared with velocities pre- dicted using preferred fit parameters	79
8.1	Radar data from the main core site	81
8.2	Power reflection coefficient of radar reflectors at coresite	83
8.3	Comparison of radar and ice core properties	85
8.4	Z-scope image of polarization experiment data	88
8.5	Polarization experiment amplitudes	89
8.6	Internal layers extracted from flow-line parallel radar profile	92
9.1	Finite element mesh and applied accumulation rate	96
9.2	Particle trajectories intersecting ice core and ice core vertical thinning functions	99

9.3	Eleven-year thickness predicted by flow model compared with ^{10}Be variation wavelengths	101
9.4	Taylor Dome $\delta^{18}\text{O}$ correlated with Vostok δD	103
9.5	Taylor Dome ice core age determinations from stratigraphic correlation.	104
9.6	Accumulation rate profile inferred from timescale	106
9.7	Preferred accumulation rate profile compared with accumulation rates inferred from ^{10}Be and SO_4^{2-} concentrations	108
9.8	Thinning functions implied by ^{10}Be and SO_4^{2-} -derived accumulation rate profiles	111
9.9	Thinning functions for time varying ice sheet thickness driven by accumulation rate variations	114
9.10	Thinning function and accumulation rate profile with time varying ice thickness	116
10.1	Radar internal layers painted by common age	120
10.2	Accumulation rate profile for virtual ice core on northern flank	121
10.3	Comparison of accumulation rate histories inferred from timescale at core site and on northern flank.	123

LIST OF TABLES

4.1	CASERTZ platform device stream sample rates	41
6.1	Results of synthetic data inversion.	68
7.1	Results of surface velocity data inversion	77

ACKNOWLEDGMENTS

First and foremost I would like to express thanks to my advisor Ed Waddington, who made this work possible. Special thanks are due to Bruce Weertman and Al Rasmussen, on whose efforts much of this work was built. Also thanks to my fellow graduate students Anthony Gades, Nadine Nereson and Kurt Cuffey. And finally, thanks everyone who took their turn at the miserable task of driving the radar sled.

This work was supported by NSF-OPP 89-15924 and NSF-OPP 92-20261.

Chapter 1

INTRODUCTION

Ice sheets and glaciers form a major component of the global climate system. Changes in the configuration of the ice sheets can change global circulation patterns (Manabe and Broccoli, 1985). Conversely, changing patterns of temperature and precipitation can alter the size and shape of the ice sheets (Paterson, 1994). The dynamical behavior of the ice sheets must be understood if we are to understand global change on time scales of centuries to millenia. Analogous to the coupling of glacier dynamics and the global climate system, ice core paleoclimate studies and ice dynamics research are interdependent.

In early 1990, researchers at the University of Washington began an ice-core paleoclimate project at Taylor Dome, South Victoria Land, Antarctica. The work was conducted over six successive field seasons. Principal project members included E. Waddington and the author with the Geophysics Program, along with P. Grootes and E. Steig with the Quaternary Research Center. Since its inception, the project's glaciological and paleo-climatological aspects have been intimately integrated. In this dissertation, I focus on the glaciology.

1.1 Geographic setting

The modern Antarctic Ice Sheet, shown in figure 1.1, is composed of two separate parts: the East Antarctic Ice Sheet (EAIS) and the West Antarctic Ice Sheet (WAIS). The smaller WAIS rests on a bed that, even after isostatic adjustment, is largely below

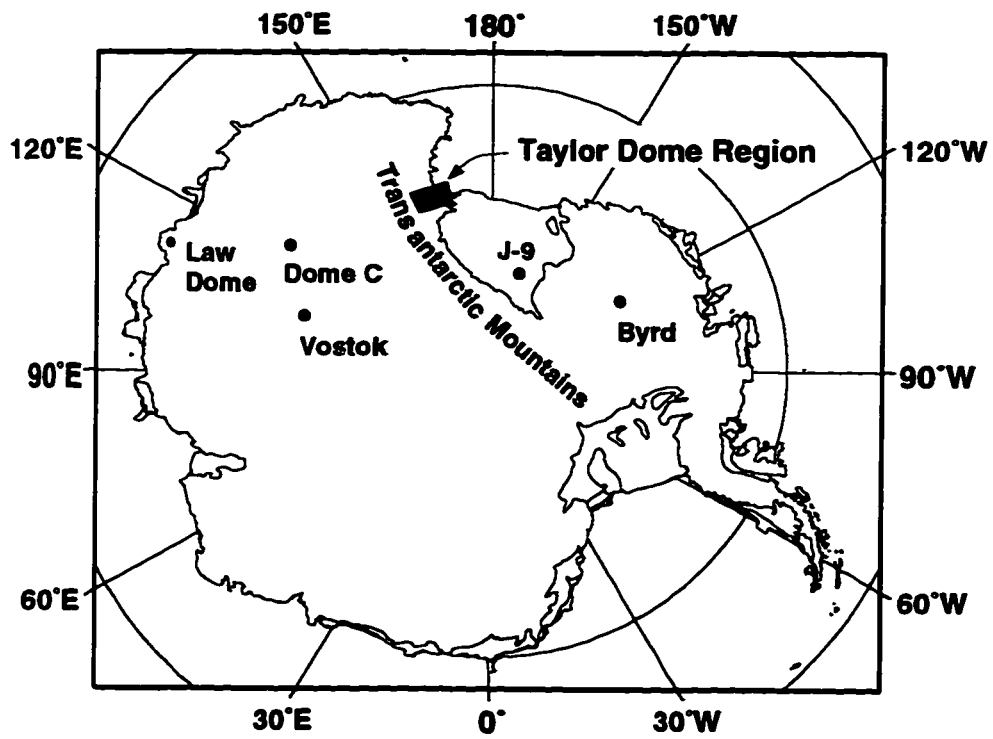


Figure 1.1: Map of Antarctica showing location of Taylor Dome in relation to Transantarctic Mountains, East and West Antarctic Ice Sheets.

sea level (Drewry, 1983). Termed a “marine” ice sheet, the WAIS is thought to be sensitive to sea level variations (Hughes, 1973; Weertman, 1974). In contrast, the surface of EAIS is a high plateau with central domes reaching 3200–4000 m elevation. Should its ice be removed, its bed would be largely above sea level after isostatic adjustment. Dynamics of the EAIS is thought to be largely insensitive to sea level variations (Sugden *et al.*, 1993), though competing hypotheses have been advanced (Barrett *et al.*, 1992).

The Transantarctic Mountains separate the EAIS and the WAIS. The range confines ice flow from the EAIS to several major drainages. A prominent surface ridge extends from Dome C to the Transantarctic Mountains west of McMurdo Sound, which divides flow northward to the David Glacier and southward to the Mulock-Byrd Glaciers. Taylor Dome lies along this ridge at an elevation of 2374 m and centered at 77° 47'S 158° 43'E. The dome rises more than 100 m above the saddle connecting it with the EAIS. Flow line reconstruction by Drewry (1982) shows this dome as a local center of outflow supplying ice to several glaciers entering the Dry Valleys of South Victoria Land, including Taylor Glacier and Ferrar Glacier.

The location of Taylor Dome in relation to the Dry Valleys and McMurdo Sound is shown in figure 1.2. The figure inset shows the extent of the airborne survey region. Figure 1.3 is a closer view of this region, showing the locations of ground-based activities. The coordinate system used in this figure, denoted “MDD”, is adopted throughout this dissertation. The primary travel lines and survey marker locations are shown in this coordinate system.

1.2 Motivation

The motivation for siting an ice-core paleoclimate project at Taylor Dome was several fold. First, it is in the southern hemisphere. The recent Greenland ice cores, GISP2 and GRIP, together provided a high-time resolution record which was primarily sen-

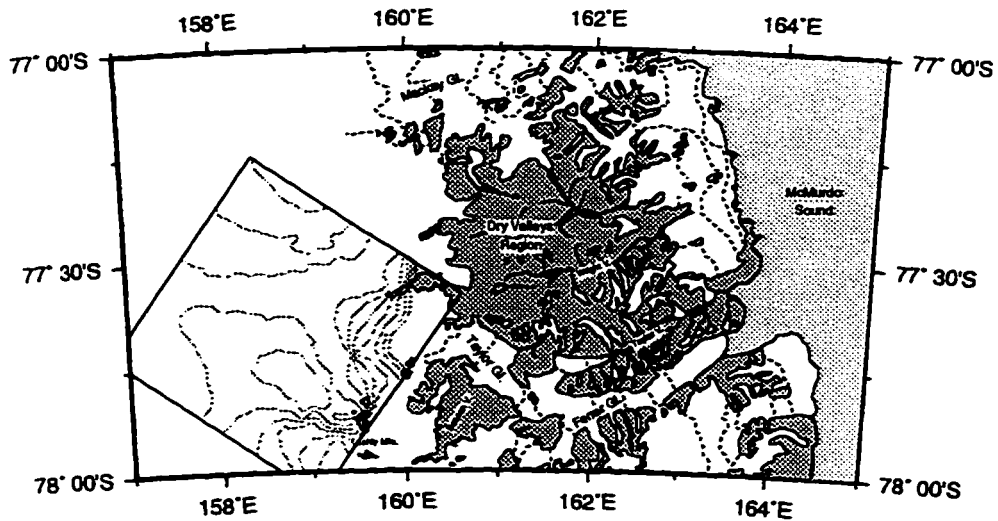


Figure 1.2: Taylor Dome location map. The map projection is Lambert Conformal Conic with standard parallels at $76^{\circ} 40'S$ and $79^{\circ} 20'S$. Inset shows the region covered by the airborne survey and 50 meter surface contour intervals.

sitive to climate over the northern Atlantic Ocean. This record, in combination with many other northern hemisphere records provides a rich and highly variable climate history through the last glacial period. The southern hemisphere, by comparison, has yielded relatively few long climate records. Due to low accumulation rate and thick ice, ice cores from Antarctica should provide very long climate records.

Second, Taylor Dome is near the coast. The global oceanic thermohaline circulation system contributes to global redistribution of heat, thus moderating global climate. Driven primarily by down-welling in the North Atlantic, it is thought to be very sensitive to climate fluctuations and capable of rapid transitions (Oeschger *et al.*, 1984; Broecker *et al.*, 1985). A climate record from the southern hemisphere that is sensitive to oceanic sources is needed to study this circulation system. Sites near the ocean should respond with greater amplitude and rapidity to local oceanic moisture sources, which in turn are affected by larger-scale oceanic circulation. The previous long climate records from Antarctica, Byrd and Vostok, were taken from deep within

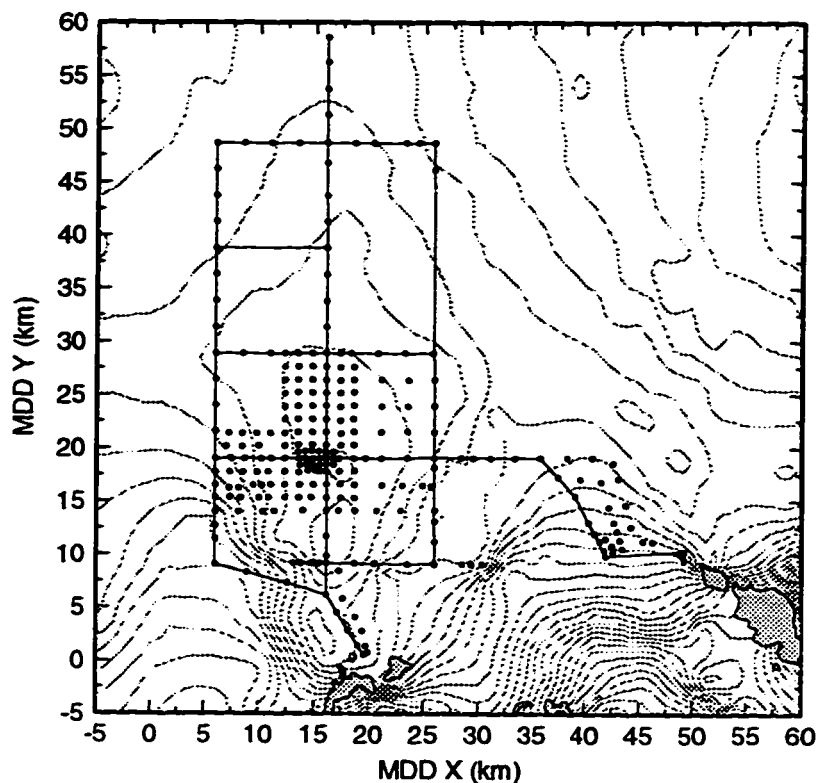


Figure 1.3: Taylor Dome survey region. This area corresponds to inset shown in figure 1.2. The “MDD” coordinate system is rotated 55° from geographic north about its origin at 78°S , 159°E . The contour intervals are 25 meters. The dots indicate the positions of survey markers, the dense cluster near (15,20) surround the core site.

the interior of the continent. These climate records are representative of much of the continent, but they could be relatively insensitive to local oceanic moisture sources.

Third, Taylor Dome is close to the Ross Ice Shelf front. Advance and retreat of the WAIS is thought to be sensitive to sea level. During the last glacial maximum, the global sea level was ~ 120 meters lower than its modern level (Shackleton, 1987). In response, the WAIS advanced into the Ross Embayment, becoming the Ross Ice Sheet. On its western margin, the ice was grounded at least as far north as McMurdo Sound (Stuiver *et al.*, 1981), and perhaps as far as the continental shelf (Anderson *et al.*, 1992; Kellogg *et al.*, 1996). Moisture-bearing storm systems which arrive at Taylor

Dome enter the continent by first passing over the Ross Ice Sheet. Accumulation at Taylor Dome is thus sensitive to the extent of the ice shelf and to sea ice cover beyond.

Fourth, Taylor Dome is near the Dry Valleys. The ice free valleys adjacent to McMurdo Sound reveal a rich history of ice marginal positions over several glacial cycles (Denton *et al.*, 1989; Sugden *et al.*, 1993). The East Antarctic outlet glaciers, small alpine glaciers within the region, and the advanced stages of the Ross Ice Sheet are all represented in this record. The proximity of the Dry Valleys and Taylor Dome allow complementary ice dynamics and paleoclimate studies.

Fifth, Taylor Dome is over a bedrock high. Ice core records from ice domes are more easily interpretable since the ice in the core originated at the same location. Radio-echo sounding profiles by Drewry (1982) indicated that the dome is tied to a local bedrock high. Thus the location of the dome has most likely been stable over time.

1.3 Goals

An extensive program of geophysical surveys was conducted at Taylor Dome. Much of that work is chronicled in this dissertation. Surface and bed topography from airborne radar profiling provide the regional setting, and a strain network provides surface motion data. A borehole temperature profile, along with surface temperatures and accumulation rates complete the suite of glaciological observations. These data are combined to determine the effective ice rheological parameters, and they become boundary conditions for numerical flow modeling. Several sites within the survey region were earlier identified by Drewry (1982) as subglacial lakes, their thermal regime is reexamined using these new geophysical data. Ground-based radar profiles reveal a detailed and complex pattern of internal layering. The primary focus of this dissertation is the interpretation of this pattern, and how it relates to the climate

record. While this work is not solely directed at paleoclimatic interpretation of the ice core record, that objective provides the context and much of the motivation.

Chapter 2

GROUND RADAR DATA COLLECTION AT TAYLOR DOME

Interpretation of radio echo sounding data is a key element of the geophysical work in support of the ice core paleoclimate profile. During the first four field seasons, 1990/91–93/94, the emphasis was on acquiring bedrock and internal layer topography for ice core site selection. The style of data collection for these field seasons may be characterized as exploration and mapping. Once sufficient bed topography data had been acquired, and initial results from the motion survey became available, the data collection mode switched to collection along flow lines. These data are central to the later analyses.

2.1 The radar system

The equipment used for the radar surveys of Taylor Dome evolved over successive seasons. The equipment was originally designed and built by B. Weertman and J. Chin for work on Dyer Plateau, Antarctica. The system was patterned after the light-weight mono-pulse described by (Watts and Wright, 1981). The transmitter delivers a step function to a resistively-loaded dipole antenna. Ideally, the loading prevents ringing, and a single pulse is radiated. The radiation is broad-band; the center frequency is determined by the overall length of the antennas. The range of operation for this system is nominally 1–10 MHz. The receiver consists of a similarly loaded antenna, signal amplifier, and digital oscilloscope. Successive stacked waveforms are stored to disk with a PC-type computer. In the profiling configuration,

the transmitter and receiver were mounted on separate sleds and pulled in-line by a snowmobile. Profiles with center-frequencies of 2, 5, and 7.5 MHz were collected along paths between the strain markers. Data acquisition was triggered at regular intervals along these path by a bicycle wheel counter, and a barometer is used to interpolate elevations. Weertman (1993) provided a detailed description of the hardware and data interpretation techniques. Since then, the receiver has been upgraded with a new digital oscilloscope, new amplifiers, and upgraded data collection software. Also, J. Chin and the author designed and constructed a new transmitter with double the output of the original system. In this dissertation, the earlier and later transmitters will be referred to as MKI and MKII, respectively.

2.2 System calibration

Radars use radio wave propagation time to simply and accurately measure distances. This is the most common mode of operation for ice penetrating radars. Physical properties of a reflector can be inferred by examining the amplitude and phase content of the return. To do so, the radiated power, sensitivity and frequency response of the system must be known. Laboratory calibration of such a radar is difficult, and not necessarily meaningful, since the operating wavelengths are large compared to typical laboratory dimensions and coupling with the room occurs. I have “calibrated” the system’s amplitude and frequency response by measuring reflections from a well characterized target under field conditions.

During the 1992 field season I conducted a series of echo amplitude measurements made on the McMurdo Ice Shelf (Morse and Waddington, 1994). The physics of electro-magnetic wave propagation, and scattering from interfaces are reviewed in appendix A. The electrical conductivity σ of sea water is about 4 S/m, making it a very good conductor at the 5 MHz sounding frequency. The power reflection coefficient of the ice-sea water interface is $R = .99 \approx -0.03$ dB and the reflection

phase shift is $\approx 3 \times 10^{-3}$. The smooth bottom of an ice shelf is thus an excellent target for such a calibration at the range of frequencies used by this radar.

For a radar system, the power returned by reflection from a plane interface is given by

$$P_r = \frac{R P_t}{4\pi(2d)^2} G_a^2 A_r L \quad (2.1)$$

where P_r and P_t are the received and transmitted power, R is the power reflection coefficient (PRC), d is the range to the target, G_a is the transmitter and receiver antenna gains, A_r is the receiver amplifier gain, and L accounts for path and system losses. This treatment is referred to as the “radar equation” (see for example, (Bogorodsky *et al.*, 1985, pp. 48)). By solving (2.1) for P_t and inserting values obtained from ice shelf bottom echos, I obtained an “effective” transmitted power which then can be used to measure reflection coefficients of other scatterers.

To use expressions like (2.1), I must define “power” as measured by a mono-pulse radar. Radars have time varying output, they transmit energy in short bursts separated by relatively long intervals. The output power must be defined in terms of the time interval over which it is measured. Pulse-width modulated carrier-wave radars generate a monochromatic wave train several to many wavelengths long. For such systems, the power is usually defined as an average over a transmitted pulse. However mono-pulse radars generate a pulse which is typically only one and a half wavelengths of their center frequency. The signal is thus necessarily broad-band in character. An example trace is included in figure 2.1 . With a waveform such as this, the times of onset and termination are somewhat arbitrary. I define the power as the square of the the peak to peak amplitude as shown in the figure.

Since these measurements were made under conditions generic to snow-covered polar ice, several of the terms in (2.1) can be treated as constants. Rather than measuring each of them, I lump the constant terms into an effective transmitted

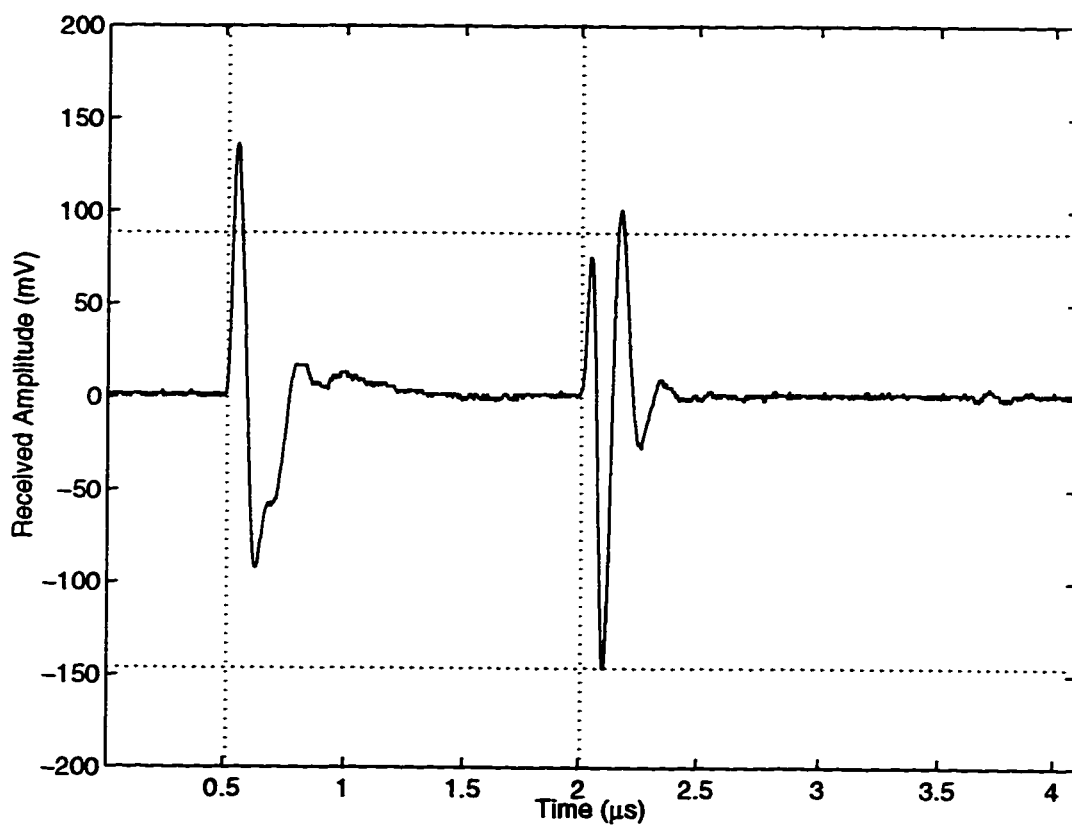


Figure 2.1: 5 MHz radar trace collected on the McMurdo Ice Shelf. The horizontal dotted lines measure the peak to peak amplitude, the vertical lines measure the travel time. A multiple return is observed at 3.7 μs .

power term by rewriting the radar as: equation

$$P_{eff} = \frac{P_r}{R} \left(\frac{d}{LA_r} \right)^2 \quad (2.2)$$

where P_r is the received power as defined above and P_{eff} is the effective “power”. Attenuation in ice is given by $L = \exp(-\sigma d/n_0)$ (derived from expression (A.7)). The waveform shown in figure 2.1 was extracted from a several kilometers long profile which traverses this region and which samples a range of ice thicknesses. At this location, the peak-peak amplitude is 235 mV; and the travel time of 1.5 μ s indicates an ice thickness of 140 m. Letting $R = 1$ and solving (2.2) for constant P_{eff} and L for the length of the profile yields an ice shelf conductivity (σ) of 1.6×10^{-5} S/m, and an effective transmitted “power” of 2.7×10^8 (mV · m)².¹ This value characterized the radar system using 5 MHz antennas and MKI transmitters; in a similar way, other values can be found for different transmitter/antenna combinations. This calibration is used in section 8.1 to evaluate the source of internal scattering which appear as layers in figures 2.4 and 2.5.

This echo strength “calibration” relies upon the reflection characteristics of a planar interface, i.e. specular reflection. If reflectors are rough on the scale of the incident wavelength, then the geometry of the reflectors must be accounted for. Scattering calculations require knowledge of the radiation pattern transmitted into the ice. A standard practice in reflection seismology (and ice radar) is to collect echos over a range of antenna separations. This is known as a “move-out” measurement and is typically used to measure the wave propagation speed in the medium. However, if the ray-paths and angle dependence of reflection are known, then this technique can also be used to measure the radiation pattern. Figure 2.2 shows relative bottom echo amplitudes plotted against nadir take-off angle from three move-out profiles collected

¹ Technically, these are not units of power. These units arise since the potential measured on the antenna leads (Volts) is not a direct measure of the electric field (V/m), i.e. the antenna area is included in the expression for “power”.

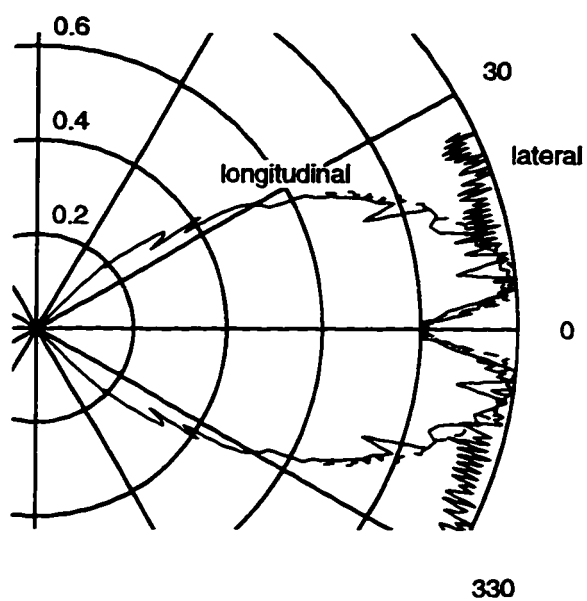


Figure 2.2: Relative amplitude radiation pattern for loaded-dipole antenna on air - snow interface indicated by CMP move-out measurements on McMurdo Ice Shelf. Three curves are shown: a fiberoptic trigger was used for a lateral and a longitudinal move-out, the wider-angle longitudinal measurement relied on airwave triggering.

on the McMurdo Ice Shelf. Since the ice-sea water interface maintains its near unity reflection over all angles, this is a direct measure of the antenna radiation pattern. The beam half width in the longitudinal orientation is $\approx 30^\circ$, but is wider than was measured laterally. The amplitude notch at nadir is a result of parasitic coupling between the closely-spaced antennas. At this point, these data are only presented: scattering calculations are not attempted. Parenthetically, the measured radiation pattern should also be used in migration calculations to avoid creation of inverted hyperbolae from anomalously bright scatterers.

2.3 Grid line radar surveys at Taylor Dome

During the first four field seasons, 1990/91–93/94 seasons, the emphasis was on acquiring bedrock topography data for ice core site selection and subsequent ice flow modeling. The style of data collection for the early field seasons was exploration and mapping. The ice core site needed to be determined. The optimal site would be identified by both ice dynamics and depositional environment considerations. The pattern of internal layering was of principle interest. Our goal was to identify sites where the layering was “simple” in order to provide the best opportunity for an interpretable ice core record.

Profiles were collected along orthogonal grid lines between the motion survey marker poles. Paths corresponding to the grid line profiles are shown in figure 2.3.

An example profile from these surveys is shown in figure 2.4. These data clearly show two of the dominant characteristics of all ground-based radar profile collected at Taylor Dome: rough bed topography, and prominent, complex internal layering. Identifying the final coring location was a process of convergence. Over successive field seasons, the profile line-spacing was decreased. Ultimately a site a few ice thicknesses to the south of the divide crest, which over-lies a bedrock plateau and displays relatively flat-lying internal layering, was identified for coring.

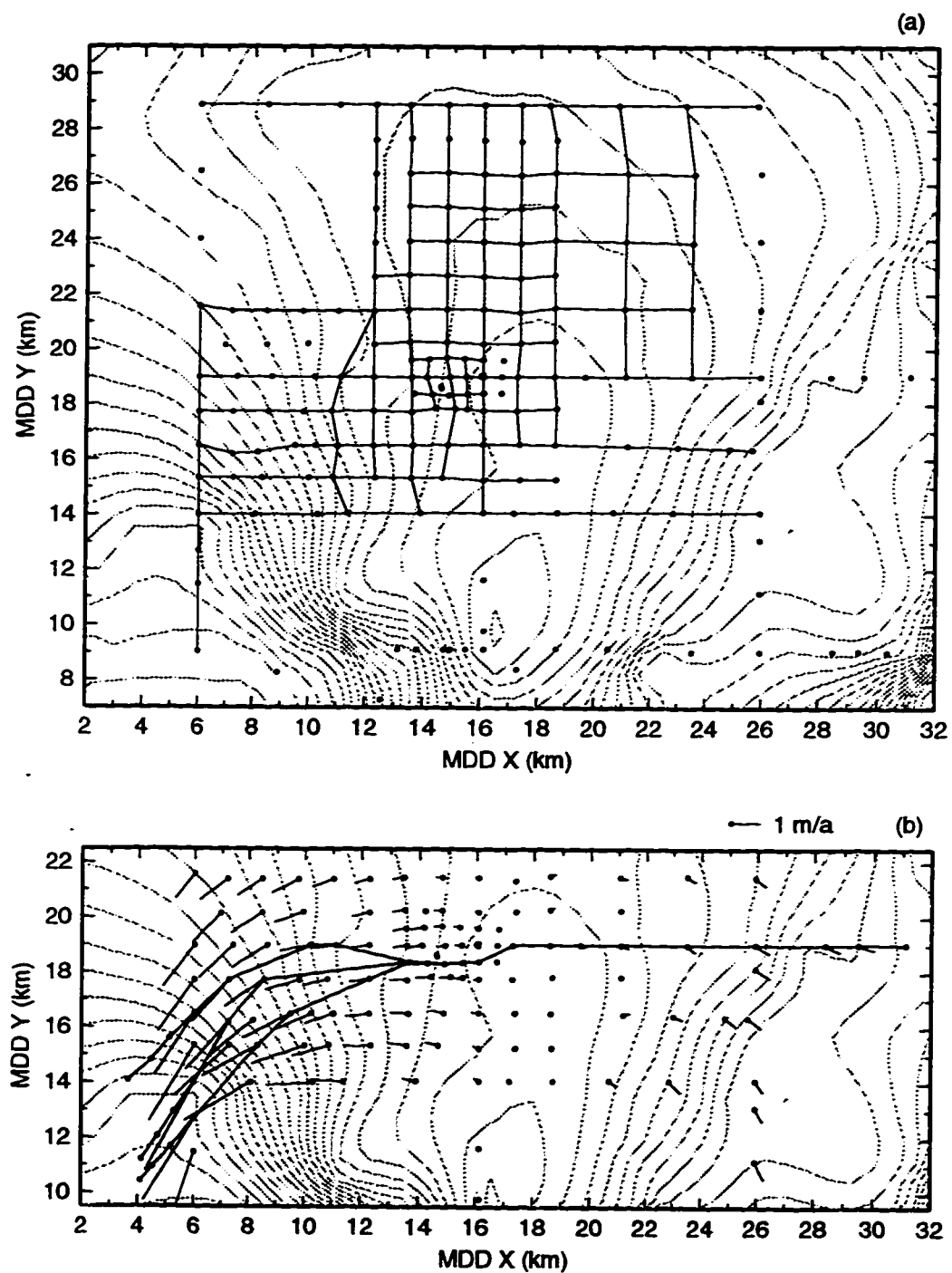


Figure 2.3: Ground radar profile paths, panel (a) shows grid-line mode profiles, and panel (b) shows flow-line mode profiles and motion marker velocities. Surface elevation contour interval is 10 meters.

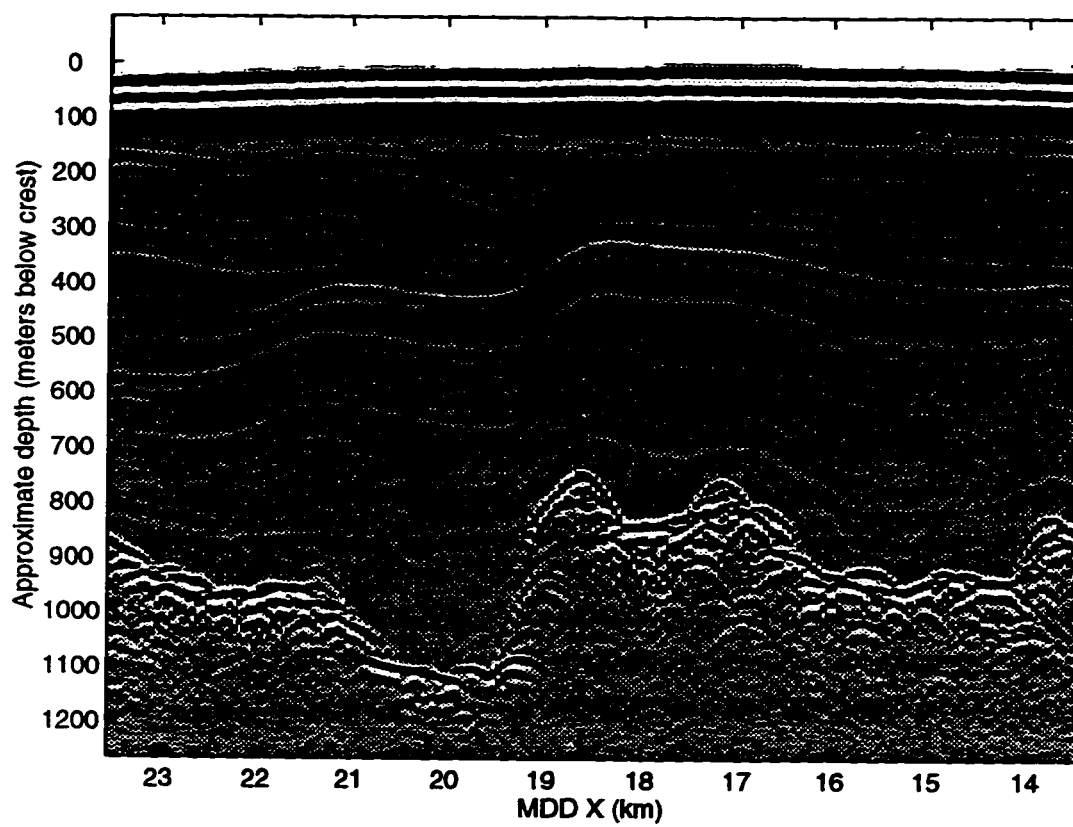


Figure 2.4: Example grid line 2 MHz radar profile.

2.4 Flow line profiles

The ground-based radar surveys may be broadly grouped into two categories, grid-line and flow-line. Gathering radio echo-sounding data on a regular grid is the most efficient way to map the bedrock and internal layers for ice core site selection. However, data collected along the actual ice flow line provide a better opportunity to model the flow field. This was the objective for the 94/95 field season. At the time, the ice motion data (discussed in section 3) had not yet been reduced, so the flow line was only approximately known from preliminary analyses. As shown in figure 2.3, these profiles were gathered along a 30 km profile approximating the ice flow line through the drill site. Three branches were profiled to the south of the core site to bound the flow line. The western branch was subsequently chosen to represent the flow line for later modeling work. The complete flow line profile is shown in figure 2.5. Ice velocity vectors shown in figure 2.4(b) confirm that the path follows the actual flow line fairly well south of km 12. To the north of km 12 the flow deviation increases to nearly 40°.

The grid-line surveys were conducted using essentially the same equipment as was developed by Weertman (1993). Significant equipment improvements were made for the 1994/95 season. In particular, a more powerful transmitter was constructed. This new transmitter allowed operation with at higher center frequency of 7.5 MHz. This, in combination with a new oscilloscope capable of faster (therefore more) stacking and longer record lengths, greatly improved the data quality over the previous seasons. These profiles clearly show the complex pattern of internal layering that exists at Taylor Dome. Interpretation of the pattern shown in figure 2.5 is the central focus of this dissertation. Previewing the concluding analyses (chapter 10), the layer pattern is interpreted as an indication of the spatial and temporal accumulation rate variations which occurred during the last glacial maximum. Several different types of geophysical data must first be combined to arrive at this conclusion.

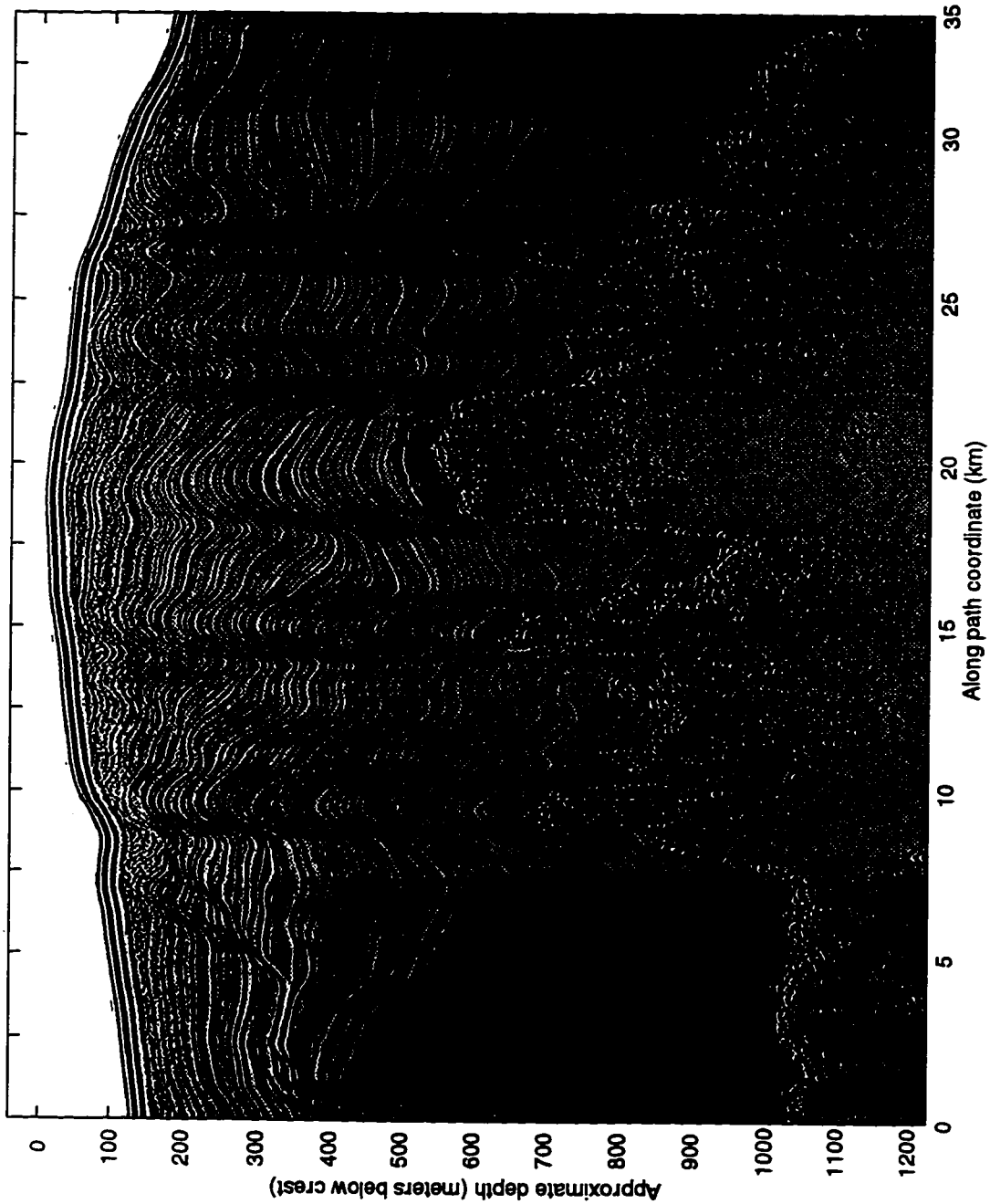


Figure 2.5: Flowline parallel 7.5 MHz radar profile. Since this profile is oblique to the MDD coordinate, it is presented in its own, along-path coordinates. The profile begins at MDD (35.7,19) and travels roughly north-south, coresite is near km 22

Chapter 3

ICE DEFORMATION SURVEY

Measurement of ice deformation has been an integral component of the project at Taylor Dome since its inception. These data provide strain rates needed to tune ice flow models which in turn are used to interpret paleoclimate from the ice core profile. Establishment of the strain network was an evolutionary process. Our early objective was core site selection. Once the site was identified, we focused on obtaining high resolution strain rates in the core vicinity and along the flow-line through the ice core site.

The relative locations of metal marker poles which comprise the strain network are shown in figure 3.1. These poles were surveyed repeatedly over six successive field seasons. Because of the low local accumulation rate, only one of these poles needed to be extended over the duration of the project, otherwise the original pole sections were observed. The poles were surveyed primarily by traditional optical techniques, using a WILD T1000 theodolite and DI5S EDM. Rigid body translation and rotation were constrained by GPS ties to bedrock at two locations.

This work has been described elsewhere (Waddington *et al.*, 1991; Morse and Waddington, 1992). Core site selection would be an iterative process. We needed to know the topography in order to choose the site; thus we needed both surface topography and bed topography from radar sounding. But to put in a high-density network everywhere would be too large a task. We began by laying out a 10 km grid of travel lines, with surveyed markers placed at 2.5 km intervals. These poles are shown in figure 3.1 as open circles. Based on little more than a guess of where the core site should be, we filled in the 10 × 12.5 km sub-region with 2.5 km pole spacing

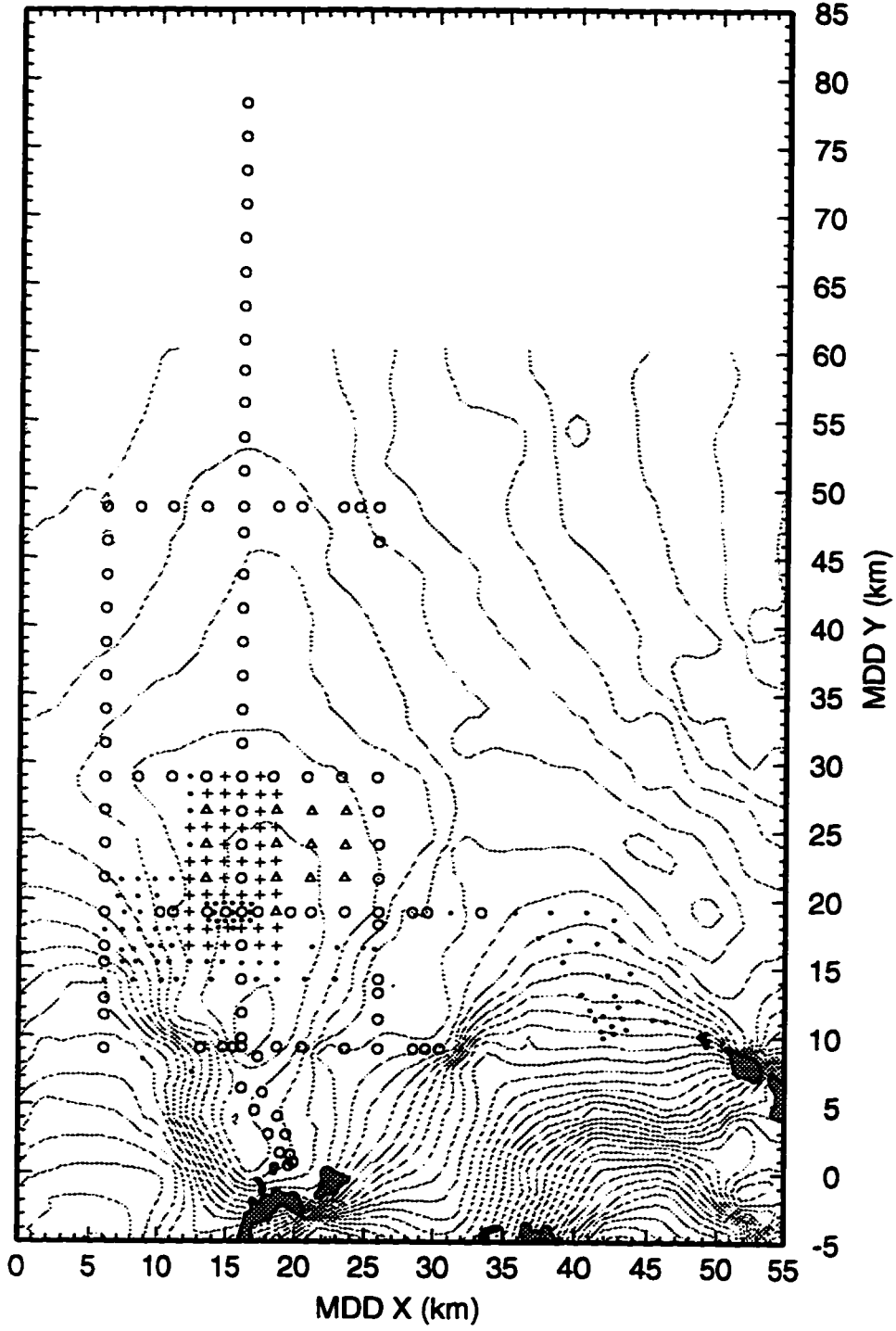


Figure 3.1: The Taylor Dome strain network. The motion poles, indicated by the various symbols are discussed in the text. Surface elevation contour interval is 20 m.

shown in figure 3.1 as open triangles. During the second season, additional poles were filled in with 1.25 spacing along the divide crest. The core site was determined by the third season and we shifted our attention to high-resolution surveys in the vicinity of the core. In addition, markers were located near the “Taylor Mouth” core site, MDD(42,11).

An important component of the the strain network was ties to fixed bedrock markers. These would provide the fixed frame of reference to constrain rigid-body translation and rotation. During the first season, a benchmark was established at (20,0). and during the third season a second bedrock tie was made at (50,10). The fourth season was to be the final surveying season, all of the previous season’s stakes would need to be resurveyed. However, many of the critical stakes, those in the vicinity of the core had only undergone a single year displacement. With typical strain-rates on the order of $10^{-4}a^{-1}$, the relative displacement of poles on ~ 600 meter baselines, would be on the order of a centimeter. With even the most careful optical surveying techniques, their motion would barely be detectable above the noise. However the other stakes which had been in place two or three years should have undergone detectable deformations. In the end, the goal of resurveying all the poles in 1993/94 wasn’t achieved, and over the two subsequent seasons, GPS surveying techniques were employed to complete the survey.

The standard technique for solving strain-net data for velocities is often termed “reduction to epoch”. By this technique, the position of all points is found for two or more distinct times, then they are subtracted to give velocities. Because the initial placement and resurveys of poles were staggered over several seasons, this method would not be practical. For a similar, though smaller, project on Agassiz Ice Cap, Waddington and Rasmussen (in prep.) developed a technique for simultaneous reduction of survey data. By this procedure, they solved for pole positions and velocities which minimize the aggregate observation error in a least-squares sense. Since pole velocities are solved directly, such an approach is ideally suited for the

Taylor Dome strain net data reduction. However, because their algorithm uses a rectangular geometry, crucial long-baseline GPS observations could not be directly utilized. Thus new algorithms were needed to properly integrate the GPS survey data with the optical data. In the following sections, I will present the approach of Waddington and Rasmussen (in prep.), then I present new algorithms, and finally, these algorithms are used to solve the Taylor Dome motion survey data.

3.1 *Algorithm for simultaneous solution of survey data*

Surveying, whether by optical or satellite techniques, provides data which are measures of geometric properties of the coordinates of the observed points. These may be any of

- the horizontal angle θ formed by three points
- the zenith angle ϕ from one point to another
- the distance S between two points
- any of the three spatial coordinates x, y, z of a point
- differences in any of the three coordinates x, y, z of two points

The first four of these are the typical observables of traditional optical surveying techniques, while the final two are typical observables of satellite surveying techniques. Given N_{pts} observed points which comprise a strain net, six trajectory parameters, $\vec{X}_T = X, Y, Z$ and $\vec{U} = U, V, W$ specify each stake's position at time t by

$$\vec{x}(t) = \vec{X}_T + (t - T)\vec{U} \quad (3.1)$$

Some of these parameters may be specified, such as $\vec{U} = 0$ for stationary markers. The remaining N_{adj} free parameters are determined as the solution of a non-linear least squares problem having as its data $N_{obs} > N_{adj}$ observations which are geometric

properties of the points. The quantity to be minimized is the root-mean-square observation discrepancy R given by

$$R^2 = \frac{1}{N_{obs}} \sum_{I=1}^{N_{obs}} \left[\frac{Q_I^o - Q_I}{\sigma_I} \right]^2 \quad (3.2)$$

in which Q_I^o is the observed quantity, and σ_I is the estimated standard error in Q_I^o . The corresponding calculated quantity is $Q_I = Q(P_1, P_2 \dots)$, in which the P_m are the trajectory parameters of the points involved in the observation.

The problem is linearized by first writing the observation equation in the form

$$\frac{Q_I + \Delta Q_I - Q_I^o}{\sigma_I} = 0 \quad (3.3)$$

The increment ΔQ is the amount Q_I would change if the P_m were changed by the amount ΔP_m . A first-order Taylor series expansion yields

$$\Delta Q_I = \sum_{m=1}^{N_{adj}} \frac{\partial Q_I}{\partial P_m} \Delta P_m$$

Here P_m is any of the parameters X, Y, \dots and ΔP_m is any of $\Delta X, \Delta Y, \dots$. When this is substituted into equation (3.3), it may be rearranged as

$$\sum_{m=1}^{N_{adj}} \frac{1}{\sigma_I} \frac{\partial Q_I}{\partial P_m} \Delta P_m = \frac{Q_I^o - Q_I}{\sigma_I} \quad (3.4)$$

Taken together, N_{obs} equations (3.4) make up the over-determined system of linear equations

$$\mathbf{A}\vec{p} = \vec{d} \quad (3.5)$$

in which: (1) the rows of matrix \mathbf{A} are the non-zero, σ -scaled derivatives $\frac{\partial Q_I}{\partial P_m}$, (2) the elements of the N_{adj} -long vector \vec{p} are adjustments to the adjustable parameters \vec{P} , and (3) the weighted observation discrepancy $(Q_I^o - Q_I)/\sigma_I$ is the I -th element of the N_{obs} -long vector \vec{d} . The form of the partial derivatives of Q_I depends upon the type of the observation Q_I^o , which determines how Q_I is expressed in terms of

the trajectory parameters. The formulation of Q_I and $\frac{\partial Q_I}{\partial P_m}$ for the observation types listed above are presented in section 3.2.

Since the elements of the matrix \mathbf{A} depend upon \vec{P} , equation (3.5) cannot be solved directly; the trajectory parameters \vec{P} which minimize R are found by iteration. The process begins with a good first approximation of the trajectory parameters $\vec{P}_{initial}$. From this the Q_I are calculated, giving rise to the matrix \mathbf{A} , the vector \vec{d} , and the performance parameter R . Standard mathematical software is used to solve equation (3.5) for the adjustments \vec{p} that minimize $\|\mathbf{A}\vec{p} - \vec{d}\|$. With \vec{p} , a new \vec{P} is formed which gives rise to new Q_I 's, a new \mathbf{A} , and a new R . The process continues until R ceases to decline.

An advantage of this formulation for simultaneously determining all trajectory parameters is that it minimizes the aggregate of all the observation discrepancies; in so doing, the solution also explicitly takes into account the estimated error in each observation. An estimate of parameter errors can be obtained directly from the observation uncertainties. Equation (3.5) can be rewritten

$$\vec{p} = \mathbf{B} \vec{d}$$

Where the matrix \mathbf{B} is the pseudo-inverse of \mathbf{A} . With \mathbf{B} so constructed, its elements approximate the derivatives $\partial P_I / \partial d_m$. The covariance between trajectory parameters P_i and P_j is given by

$$\text{cov}(P_i, P_j) = \mathbf{B} \text{cov}(d_K, d_L) \mathbf{B}^T \quad (3.6)$$

where $\text{cov}(d_K, d_L)$ are the covariances of the observation errors. Because the observation discrepancies are scaled by their standard errors, the elements of \vec{d} are dimensionless with unit variance, $\sigma_d^2 = 1$. As a consequence, $\text{cov}(d_K, d_L)$ will be normalized also; that is it will be numerically equal to the correlation (-1 to 1) between observations K and L . If the observation errors are uncorrelated, $\text{cov}(d_K, d_L)$ becomes the identity matrix, and equation (3.6) reduces to

$$\text{cov}(P_i, P_j) = \mathbf{B} \mathbf{B}^T$$

In this case, the diagonal elements $\text{cov}(P_i, P_i)$ are the expected parameter errors squared.

3.1.1 The medium-scale domain survey data reduction algorithm, “uvwxyz”

The algorithm presented in the previous section is in fact fairly generic; it may be applied to a range of problems. The details of how it is adapted to a particular application lie in what the parameters represent, and how the observations are expressed in terms of these parameters. In adapting this approach to solve optical survey data for pole positions and velocities, Waddington and Rasmussen considered the first three of the observation type listed at the beginning of section 3.1. This algorithm is later referred to as “uvwxyz”.

A difficulty in dealing with theodolite-measured angles is that they are measured relative to the gravity vector – the theodolite is first leveled with a bubble, then vertical angles are measured relative to its rotation axis, and horizontal angles are measured in the plane normal to this axis. If a very restricted spatial domain is considered, this problem can be ignored since the gravity vector may be assumed to be parallel everywhere, but such a small scale is rarely interesting in glaciology. Instead, Waddington and Rasmussen, constructed a locally defined Cartesian space in which at every point, the gravity vector was assumed to be parallel to the “z” coordinate axis, and an earth-curvature correction was applied to vertical angles. The advantage of this space is that the description theodolite angles with respect to the coordinate system was straightforward. This coordinate system is in a sense conformal, in that great circle paths would map to straight lines with constant “z”-coordinate. This system isn’t appropriate for continental scale surveys, but over the “medium”-scale, *i.e.* a few tens of kilometers, it is acceptable. Errors introduced from distortion of the coordinate system are spread over the network, and are minimized where the data density is highest. However, the advantage of simplicity with this system is lost when integrating satellite based observations, such as from GPS, where single observations

may be over several tens of kilometers. Two problems arise, (1) distortion of the coordinate system becomes significant over long baseline observations, and (2) since the coordinate system is not analytically expressed, it is difficult to interpret the meaning of coordinate type observations. Since the final two season's surveys were done with GPS and these data are crucial for the newest poles in the vicinity of the core site, a new formulation for the survey reduction algorithm, one which properly integrates optical and GPS observations, was required.

3.1.2 The large-domain survey data reduction algorithm, "UVWXYZ"

The difference between the existing algorithm "uvwxyz", and the one presented here "UVWXYZ", lies in the coordinate system in which the solution is formed and, consequently, how the observations are expressed with respect to the coordinates. The limitations of the earlier algorithm stem directly from the assumed coordinate system. By using globe-centered Cartesian coordinates (GCC) – the same coordinate system in which GPS observations are expressed – the incorporation of GPS data becomes trivial. GPS point-position are expressed in GCC, these are used directly as coordinate-type observations: no local coordinate system projections are necessary. GPS baseline data from differential surveys are directly utilized by specifying a newly-defined, coordinate-difference observation type.

Adopting GCC coordinates, however, casts the burden of complexity onto incorporation of theodolite angle data. Additional information is needed, specifically the direction of the gravity vector in the adopted coordinate system. Properly done, this should be obtained from field measurements, or perhaps taken from an established local geoid. However, the geoid is poorly known in the Antarctic, particularly in regions adjacent to the Transantarctic Mountains. But, since the errors introduced from uncertainties in the gravity vector primarily affect the vertical angle measurements, which themselves are of poor reliability for other reasons, the overall survey reduction is fairly insensitive to errors in the specification of the gravity vector. I

have assumed that the gravity vector can be approximated by the normal to the WGS84 ellipsoid. With the local normal vector defined, new formulations for the angle observation type are developed which are referenced to the GCC coordinates.

3.2 Formulation of observation types

In order of increasing complexity, the explicit formulations are presented for the values Q and $\partial Q_I / \partial P_m$, for the observations types discussed in section 3.1, which are used to construct equation (3.5). The minimizations done in the trajectory parameters, therefore, the derivatives of the observations used to form the elements of matrix \mathbf{A} must be done with respect to the trajectory parameters. But the observations are more directly expressed in terms of the point's coordinates at the time of the observations. Expression (3.1) relates the coordinates, at the time of observation, to the parameters: a simple application of the chain rule gives partials with respect to the underlying the parameters.

Coordinate and delta-coordinate observations

The x -coordinate of a marker at station i is computed simply as

$$x = x_i + h_i (\hat{n}_i \cdot \hat{x})$$

where \hat{n} is the normal vector to the gravitational equipotential, and h_i is the height of the marker above point i . Differentiation with respect to the point's coordinates gives

$$\Delta x = \Delta x_i$$

Here, and elsewhere, the small terms in $\partial \hat{n}_i / \partial x_i$ are ignored. A further differentiation, this time with respect to the underlying trajectory parameters gives

$$\Delta x = \Delta X_i + (t - T) \Delta U_i$$

For this example, x is the calculated quantity Q against which the observation Q^o is compared to form the vector \vec{d} . The row of matrix A which corresponds to this observation will contain two non-zero elements, $1/\sigma$ and $(t - T)/\sigma$, in the positions which correspond to the point's trajectory parameters X_i and U_i . Similarly, delta- x -coordinate observations between points i and j are calculated from

$$\delta x = x_i + h_i (\hat{n}_i \cdot \hat{x}) - x_j - h_j (\hat{n}_j \cdot \hat{x})$$

when differentiated this gives

$$\Delta \delta x = \Delta x_i - \Delta x_j$$

From here on, the further derivatives in the trajectory parameters are not presented. Expressions for coordinate and delta-coordinate observations in y and z are analogous and so, too, are not shown.

Distance observations

The slope distance between points j and i , such as is measured by an EDM, is given by the length of the coordinate difference vector

$$S_{ji} = \left\| \vec{D}_{ji} \right\| = \left\| (\vec{X}_i + h_i \hat{n}_i) - (\vec{X}_j + h_j \hat{n}_j) \right\|$$

When differentiated this gives

$$\Delta S_{ji} = \frac{x_i - x_j}{S_{ji}} (\Delta x_i - \Delta x_j) + \frac{y_i - y_j}{S_{ji}} (\Delta y_i - \Delta y_j) + \frac{z_i - z_j}{S_{ji}} (\Delta z_i - \Delta z_j)$$

Vertical angle observations

A theodolite vertical angle is measured between the local normal and the image of the target in the telescope. The scalar product of the instrument normal \hat{n}_j and the coordinate difference vector \vec{D}_{ji} gives the cosine of the angle between them.

$$\cos \phi = \frac{\hat{n}_j \cdot (\vec{D}_{ji} + f(S_{ij} \sin \phi)^2 \hat{n}_i)}{\vec{S}_{ij}} \quad (3.7)$$

The term involving f is a small correction for atmospheric refraction effects, its value is discussed in section 3.3. When differentiated this gives

$$\Delta\phi = \frac{1}{S_{ji}^2 \sin\phi} \left[\begin{array}{l} (\cos\phi(x_i - x_j) - S_{ji}(\hat{n}_j \cdot \hat{x}))(\Delta x_i - \Delta x_j) + \\ (\cos\phi(y_i - y_j) - S_{ji}(\hat{n}_j \cdot \hat{y}))(\Delta y_i - \Delta y_j) + \\ (\cos\phi(z_i - z_j) - S_{ji}(\hat{n}_j \cdot \hat{z}))(\Delta z_i - \Delta z_j) \end{array} \right]$$

Here, small contributions from the refraction term are ignored, This expression is finite, despite containing $\sin\phi$ in the denominator, since $\phi \sim \pi/2$ for these observations.

Horizontal Angle Observations

For each of target and reference, projections of the coordinate difference vectors onto local horizontal plane are given by

$$\begin{aligned} \vec{e}_{ji} &= (\hat{n}_j \times \vec{D}_{ji}) \times \hat{n}_j = \vec{D}_{ji} - (\hat{n}_j \cdot \vec{D}_{ji})\hat{n}_j \\ \vec{e}_{jk} &= (\hat{n}_j \times \vec{D}_{jk}) \times \hat{n}_j = \vec{D}_{jk} - (\hat{n}_j \cdot \vec{D}_{jk})\hat{n}_j \end{aligned}$$

The angle between these vectors is the horizontal angle. From their scalar product

$$\cos\theta = \frac{\vec{e}_{jk} \cdot \vec{e}_{ji}}{S_{jk} S_{ji}} \quad (3.8)$$

differentiated, this gives

$$\Delta\theta = \frac{1}{S_{jk}^2 S_{ji}^2 \sin\theta} \left[\begin{array}{l} (S_{jk}^2 e_{ji1} \cos\theta - S_{jk} S_{ji} e_{jk1}) (\Delta x_i - \Delta x_j) + \\ (S_{jk}^2 e_{ji2} \cos\theta - S_{jk} S_{ji} e_{jk2}) (\Delta y_i - \Delta y_j) + \\ (S_{jk}^2 e_{ji3} \cos\theta - S_{jk} S_{ji} e_{jk3}) (\Delta z_i - \Delta z_j) + \\ (S_{ji}^2 e_{jk1} \cos\theta - S_{jk} S_{ji} e_{ji1}) (\Delta x_k - \Delta x_j) + \\ (S_{ji}^2 e_{jk2} \cos\theta - S_{jk} S_{ji} e_{ji2}) (\Delta y_k - \Delta y_j) + \\ (S_{ji}^2 e_{jk3} \cos\theta - S_{jk} S_{ji} e_{ji3}) (\Delta z_k - \Delta z_j) \end{array} \right]$$

where the numbered subscripts are the three-space components of the coordinate difference vectors. Since these expressions are imprecise when $\theta \sim 0$ and $\theta \sim \pm\pi$.

alternate expressions are used. From the vector product of the coordinate difference vector projections,

$$\sin \theta = \frac{\hat{n}_j \cdot (\vec{e}_{jk} \times \vec{e}_{ji})}{S_{jk} S_{ji}} \quad (3.9)$$

which, when differentiated gives

$$\Delta \theta = \frac{1}{S_{jk}^2 S_{ji}^2 \cos \theta} \left[\begin{array}{l} (S_{jk} S_{ji} e_{jk1} - \sin \theta S_{jk}^2 (n_{j2} e_{ji3} - n_{j3} e_{ji2})) (\Delta x_i - \Delta x_j) + \\ (S_{jk} S_{ji} e_{jk2} - \sin \theta S_{jk}^2 (n_{j3} e_{ji1} - n_{j1} e_{ji3})) (\Delta y_i - \Delta y_j) + \\ (S_{jk} S_{ji} e_{jk3} - \sin \theta S_{jk}^2 (n_{j1} e_{ji2} - n_{j2} e_{ji1})) (\Delta z_i - \Delta z_j) + \\ (S_{jk} S_{ji} e_{ji1} - \sin \theta S_{ji}^2 (n_{j3} e_{jk2} - n_{j2} e_{jk3})) (\Delta x_k - \Delta x_j) + \\ (S_{jk} S_{ji} e_{ji2} - \sin \theta S_{ji}^2 (n_{j1} e_{jk3} - n_{j3} e_{jk1})) (\Delta y_k - \Delta y_j) + \\ (S_{jk} S_{ji} e_{ji3} - \sin \theta S_{ji}^2 (n_{j2} e_{jk1} - n_{j1} e_{jk2})) (\Delta z_k - \Delta z_j) \end{array} \right]$$

In expressions (3.2) and (3.2), small terms involving $\hat{n}_j \cdot \vec{d}_{ji}$ and $\hat{n}_j \cdot \vec{d}_{jk}$ have been neglected. Depending on the value of θ , one or the other of the above expressions for $\Delta \theta$ are used to construct the **A** matrix. However, because of the discontinuity at $\pm \pi$, simple differences ($\theta^\circ - \theta$) are not used to construct \vec{d} . Rather, the angle difference is given by

$$\tan(\theta^\circ - \theta) = \frac{\tan \theta^\circ - \tan \theta}{1 + \tan \theta^\circ \tan \theta} = \frac{\cos \theta \sin \theta^\circ - \sin \theta \cos \theta^\circ}{\cos \theta \cos \theta^\circ + \sin \theta \sin \theta^\circ}$$

where $\cos \theta$ and $\sin \theta$ are given by (3.8) and (3.9), respectively.

3.3 Reduction of Taylor Dome survey data

Reducing optical survey data is a tedious procedure since the data are easily subject to errors. The data are collected under sometimes adverse conditions, and transcription errors can occur at several stages. Such noise sources will be termed operator “blunders”. Each season’s optical data were first “cleaned” of spurious data by multiple iterations of running the reduction program “uvwxyz”, and evaluating the observations with outlying discrepancies. After each of the season’s optical data were cleaned they were combined to form a multiple-season simultaneous solution.

The GPS data were collected using TRIMBLE 4000SST dual-frequency receivers. The data were post-processed using TRIMBLE GPSurvey software. Precise satellite ephemeris, obtained from the U.S. Coast Guard Navigation Center, were used in all of the solutions. Two type of surveys were employed. Long-duration “static” surveys were done of the two bedrock markers and of a reference pole near the core-site. For these, the receivers were run for 6 to 12 hours. A fourth simultaneously running receiver, maintained by the UNAVCO consortium at a geodetic reference position at the nearby McMurdo station, provided position controls for the two bedrock positions. These surveys provide high-precision control for the near-stationary reference pole (628). Multiple other poles were positioned by a series of “fast-static” occupations of typically 10 to 20 minutes each, using pole 628 as the reference position. Two roving receivers were used for these surveys, so that whenever simultaneous occupations occurred, all three baselines were calculated.

Processing of the GPS data was order dependent. A one meter error in the absolute coordinates of the reference receiver introduces a .1 ppm systematic error in differential measurements from that receiver (Remondi, 1984). So care must be taken that for each baseline processed, the reference position used is the best position available. The baselines were processed as follows: (1) the four baselines from the CRAR base-station were averaged to form the coordinates of the two bedrock stations (964 and 610); then (2) in each of the seasons, baselines from the two bedrock point were averaged to give the “best” position for moving marker pole 628 (3) the 628 positions were then used as reference positions for the inter-pole baselines. All of these baselines, and the coordinate observations of the two bedrock points, form the set of GPS observations.

Prior to combining the optical and GPS survey data, two parameters needed to be found, the atmospheric correction coefficient for the vertical angles, and the observation standard errors for the GPS baseline components.

Atmospheric refraction correction

In optical surveying, light path refraction due to temperature gradients in the near surface atmosphere causes observed targets to have an apparent vertical offset. To correct for this effect, a small correction term is applied to the calculation of vertical angles. The coefficient f , in equation (3.7) depends upon the strength of the near-surface temperature gradient. Simultaneous vertical angles observations between two points can be used to determine an instantaneous value of f . However it is impractical to do this for each vertical angle observation for a survey of the scale of Taylor Dome. An effective value was empirically derived using the Taylor Dome 90/91 field season survey data by using the simultaneous reduction algorithm presented above with a range of single values for f . Figure 3.2 shows the resulting R as a function of f . In this plot, the flat bottom is an artifact of field-width precision used in the calculation of R . The minimum is in good agreement with the range of values (-0.86 to $-1.92 \times 10^{-8} m^{-1}$) observed on Columbia Glacier (Rasmussen, 1986). The value $-1.5 \times 10^{-8} m^{-1}$ is thus used for the remainder of the survey data reduction.

Observation standard errors

The simultaneous solution formed is a minimization of the observation errors weighted by the observation standard errors; estimates for observation standard errors are required prior to forming the solution. Formally, each observation can have a unique standard error, in practice this isn't realized since we have little reason to place more confidence on one horizontal angle, for example, than on another. Typically a single standard error value is assigned to each of the observation types. Standard errors for the optical data have been learned through experience with previous networks: the adopted values are 7 arc-seconds for horizontal angles, 20 arc-seconds for vertical angles, and 2.5 centimeters for EDM ranges. These values are larger than typical "bench" standard error values for these instruments since they must accommodate

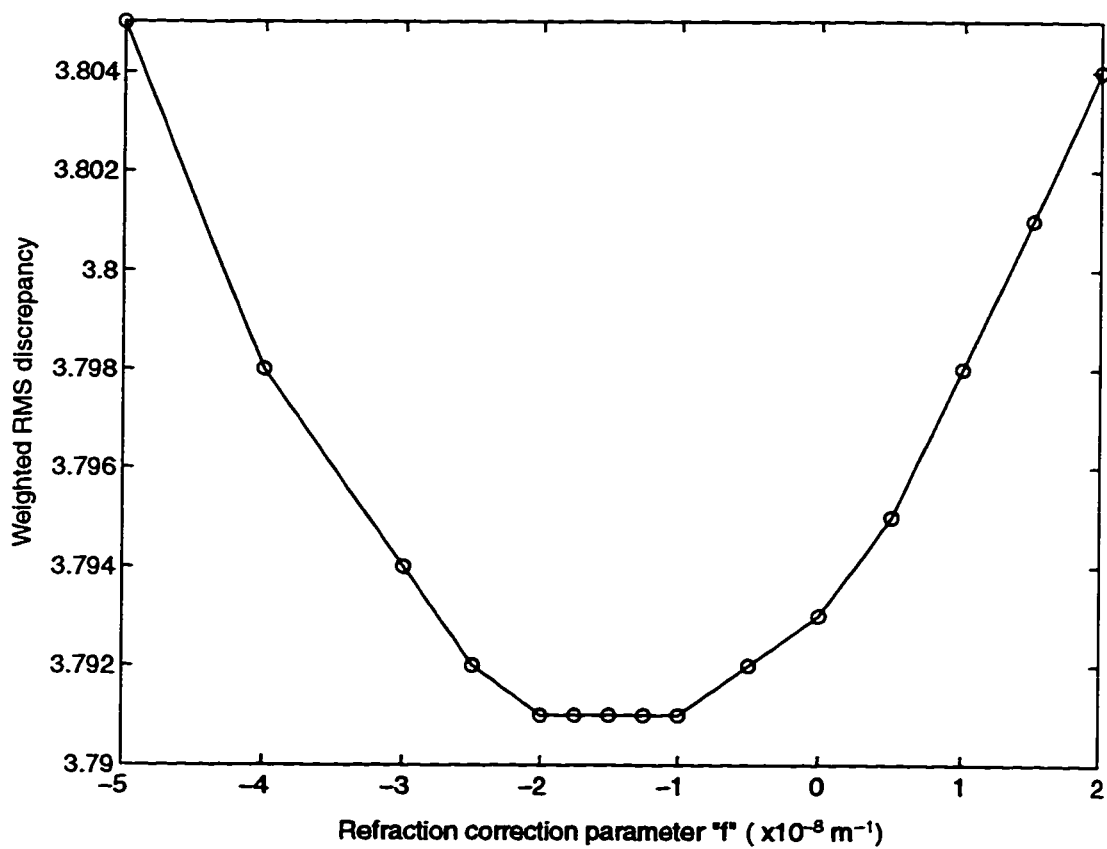


Figure 3.2: Unresolved rms observation discrepancy as a function of refraction correction parameter " f "

both the instrument imprecision (random errors) as well as undetermined number of operator errors. The relative magnitudes of the standard errors determine how important each of the observations are in forming the combined solution. Too small a standard error on the horizontal angles, for example, would yield a solution which is dominated by satisfying the horizontal angle discrepancies with little regard for possibly conflicting observations from other observation types. With GPS surveying, the baseline components “observations” are themselves parameters in a least-squares solution which uses satellite-receiver ranges as data. Trimble GPSurvey post-processing software reports standard error values along with the calculated baseline components; however these are a measure of the data scatter in forming solution, and do not represent systematic errors.

The unresolved observation discrepancies of the final parameter solution can provide a check on how well the standard error estimate represent the observation scatter. This is shown in shown in figure 3.3. Since the observation discrepancies are expressed in units of observation standard errors, the standard deviation of the discrepancies should be nearly unity. Though there are many data values, the data redundancy is in fact low since there are many adjustable parameters. It is therefore acceptable that the standard deviations shown are not exactly unity, and little would be gained in fine tuning the standard errors to force them to be. By this analysis, it was determined that the GPSurvey-reported standard error estimates needed to be scaled by a factor of 20 to give a near unity standard deviation for the delta-component observation discrepancies. As a side note, an indication of the GPS system repeatability can be obtained from the fixed leg of the bedrock ties. The baseline lengths, computed from the delta-coordinate differences in the two seasons, differed by 2 cm. This is in good agreement with the value of 2.8 cm obtained by scaling of the GPSurvey-reported standard error values by 20. Given that the adopted standard errors are acceptable (and the unavoidable assumption that the errors are uncorrelated), equation (3.1) gives the expected parameter errors in units of the parameters.

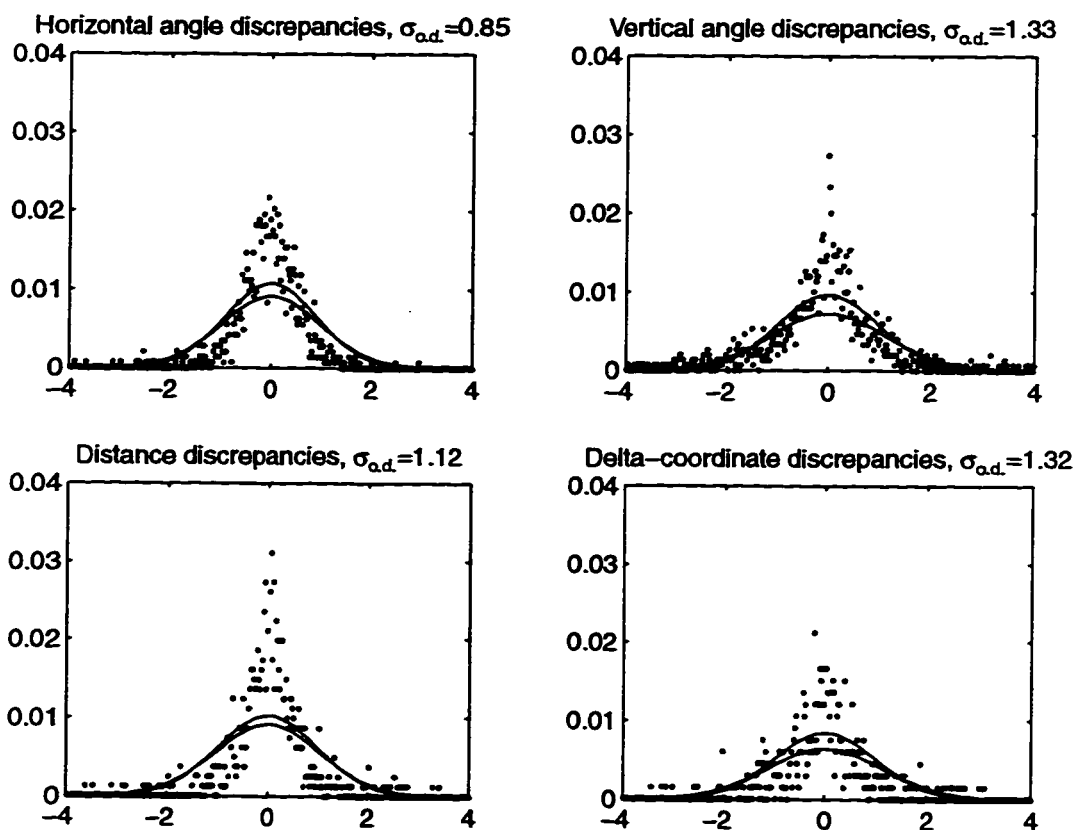


Figure 3.3: Normalized frequency distribution of unresolved observation discrepancies separated by observation type. The standard deviations $\sigma_{o.d.}$ for each of these distributions are shown in their respective title bars. In each panel, a pair of Gaussian curves are plotted, one with width parameter $\sigma = 1$, and the second with width parameter $\sigma = \sigma_{o.d.}$. The upper curve is for $\sigma = 1$ if $\sigma_{o.d.} > 1$.

3.4 The results

Velocities, and their expected errors, for poles in the core-site subregion of the Taylor Dome network are shown for two simultaneous-minimization solutions. Figure 3.4 shows the solution parameters from the combined GPS and optical problem solved using the new algorithm “UVWXYZ”. Figure 3.5 shows velocities for a solution formed with the previous reduction algorithm “uvwxyz” which used the optical survey data combined with only the bedrock to pole 628 GPS baselines expressed as distances. Comparison of the two solutions reveals the solution improvement realized by combining the GPS and optical survey data types. Poles with velocities constrained by GPS observations show significantly reduced parameter error estimated. This improvement is achieved for two reasons: (1) the poles were measured over a longer time span, reducing the signal to noise ratio for any given pole displacement; and (2) the GPS data show higher precision over long baselines than do the optical survey data.

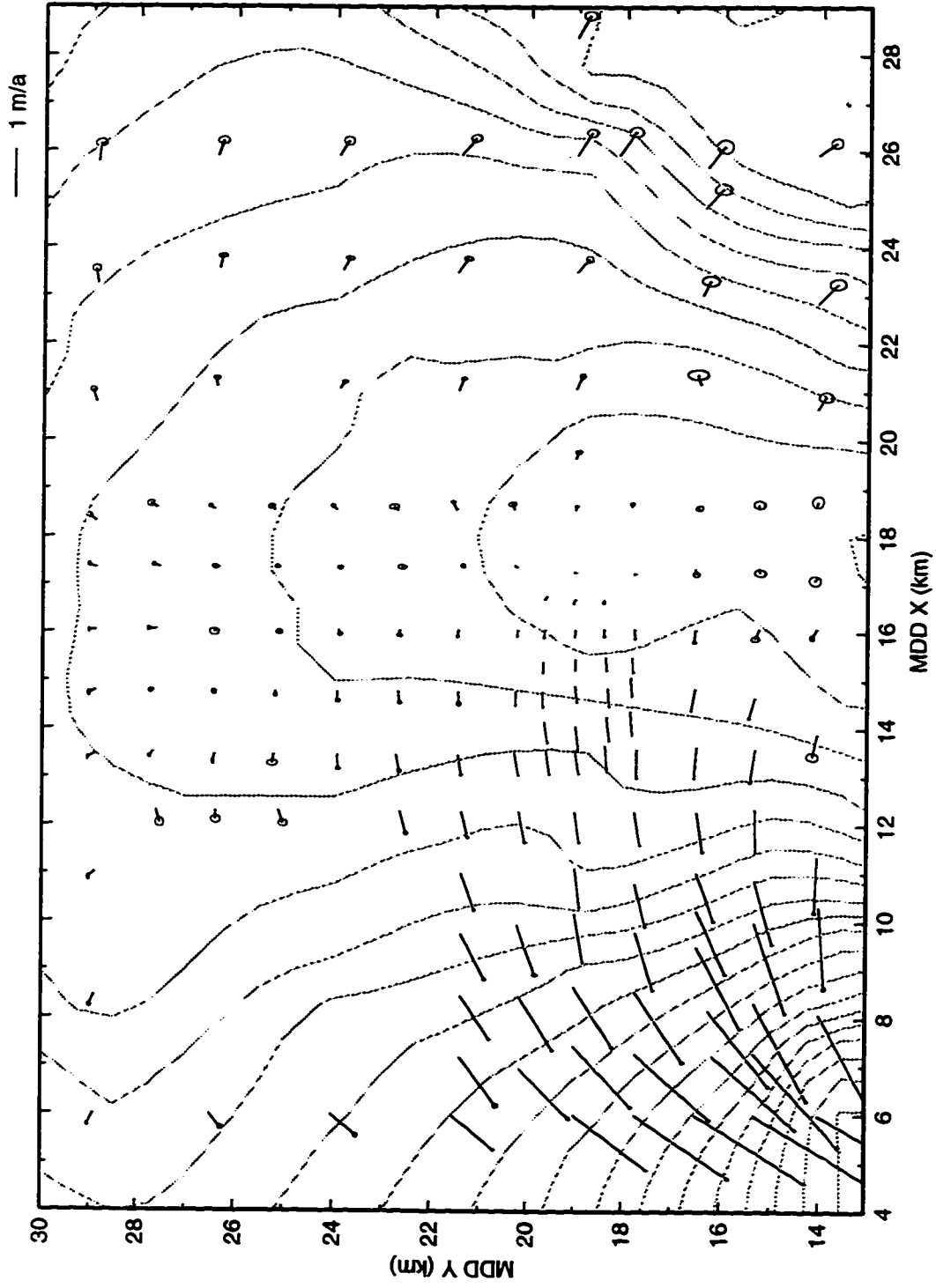


Figure 3.4: Velocities and errors from combined GPS and optical solution. Contour interval is 10 meters and the velocity scale is shown. The velocity parameter errors are indicated by ellipses at the "to" end of the velocity vectors.

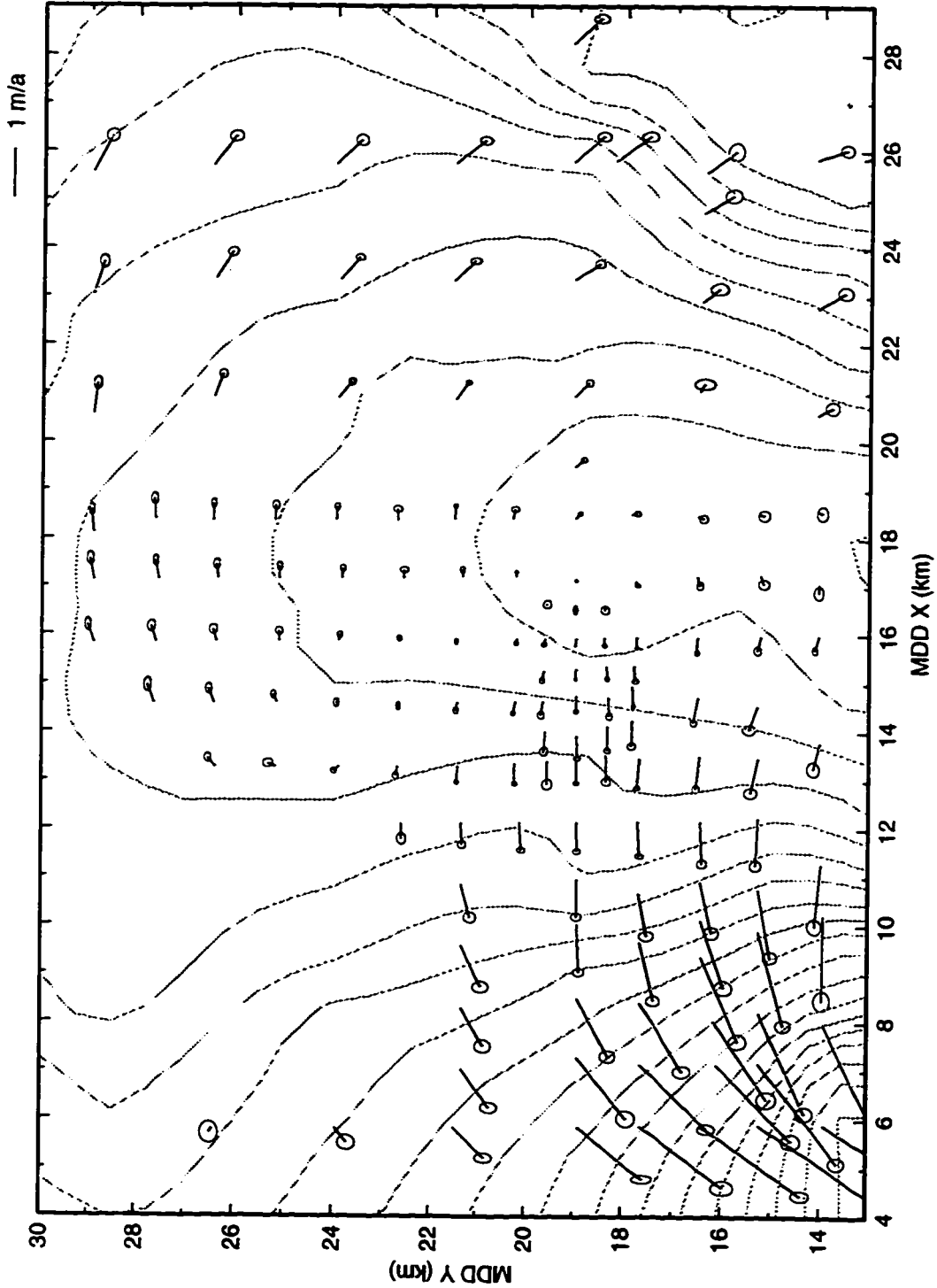


Figure 3.5: Velocities and errors from optical survey solution formed with algorithm "uvwxyz". Here, GPS data have been used to constrain the motion of the central pole.

Chapter 4

AIRBORNE SURVEY

In January, 1991, the CASERTZ¹ platform was used to conduct an airborne survey of Taylor Dome. A 55 × 55 km area was flown with 5 km line spacing. The flight tracks, shown in figure 4.1 are oriented to coincide the primary ground survey lines.

This survey provides a regional-scale surface and bed topography data set which would be difficult to obtain with ground-based techniques.

4.1 *The CASERTZ platform*

Described in Blankenship *et al.* (1994), the principle instrumentation aboard the CASERTZ de Havilland Twin Otter aircraft used for this survey were: ice penetrating radar, laser ranger, pressure altimeter, and GPS receivers. The aircraft uses C/A-code GPS for navigation, and an INS-controlled autopilot to maintain stable on-track flight lines. Kinematic GPS was used to recover precise aircraft positions. Data from the radar, laser, pressure, GPS, and INS data streams were reduced and combined over several visits to the computing facilities at UTIG under the supervision of D. Blankenship. Solution of the carrier phase kinematic GPS data was done with the K&RS software package.

Developed by the Technical University of Denmark, the pulse-width modulated TUD radar transmits 10 kW at 60 MHz. For the Taylor Dome survey, the pulse width was set to 125 ns. The return waveforms are fed through a logarithmic-gain amplifier, digitized at 8 bits, stacked 2048 times and stored at full precision with 24-bit words.

¹ Corridor Aerogeophysical Survey of the Southeast Ross Transect Zone

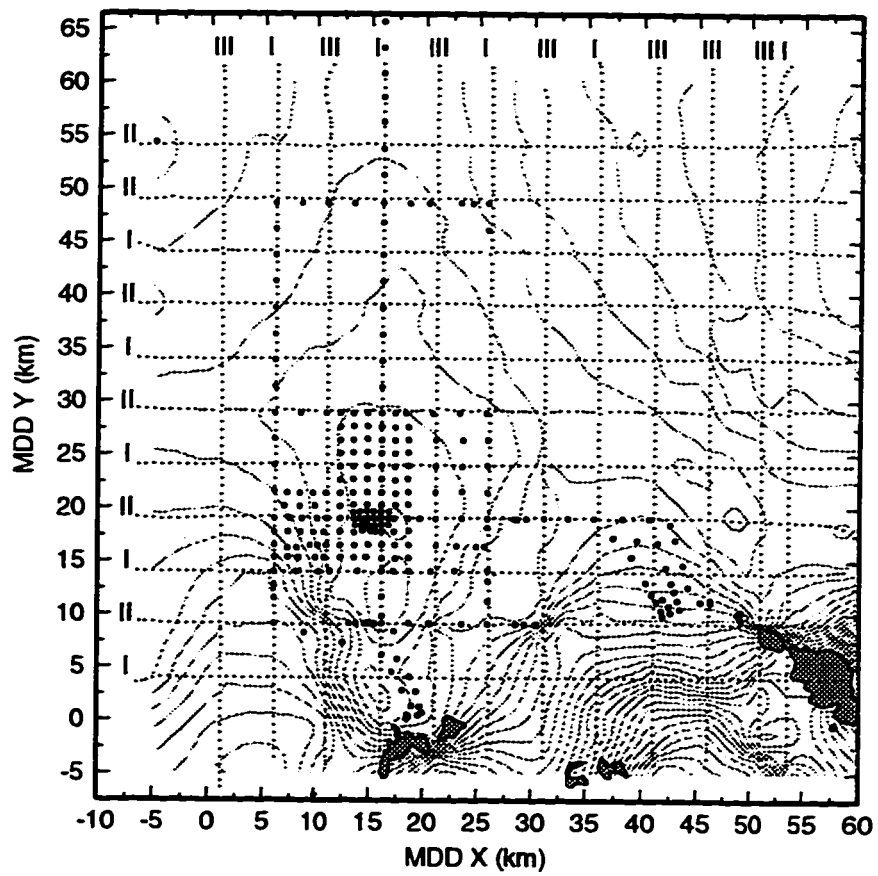


Figure 4.1: Taylor Dome survey network overlaid with airborne survey flight tracks and 25 m surface contours. Labels I, II, and III indicate the three grades of position quality: kinematic, DPR, and C/A, respectively.

Table 4.1: CASERTZ platform device stream sample rates

device stream	sample rate (Hz)
radar	3
laser range	8
pressure	5
GPS	1
INS attitude	3

The resulting 2048 sample records are collected at 3 Hz which, at the typical airspeed of 75 m/s, corresponds to approximately every 25 meters along track. With the 50 MHz sample rate, each 20 ns sample corresponds to 3 meter spatial resolution in air, and 1.7 meters in ice. Table 4.1 lists the data sampling frequency of the various streams. These streams were combined by binning to the lowest common time-base: the 1 second GPS.

4.2 Ice thickness map

For each of the profiles, the times of the outgoing pulse, and surface and bed returns were identified using an automatic signal detection algorithm. Prior to auto-detection, the algorithm's search bounds must be manually set; this is necessary in particular for identifying weak and discontinuous bed returns. The surface and bed arrival time difference are used to compute the ice thickness assuming an ice propagation speed of 169 m/ μ s (Bogorodsky *et al.*, 1985). These data are binned to one second intervals and combined with C/A-code GPS positions to form the ice thickness profiles. Crossover analysis for the profiles gives an rms mismatch of 53 meters, a high, but not surprising number considering the precision of the C/A-code positioning, the bed roughness and that no migration corrections were applied to the bed returns. The profiles were then binned to 750 m intervals using the "blockmean" GMT package (Wessel and Smith, 1995), and then grided with a tensioned bicubic spline using the "surface" GMT

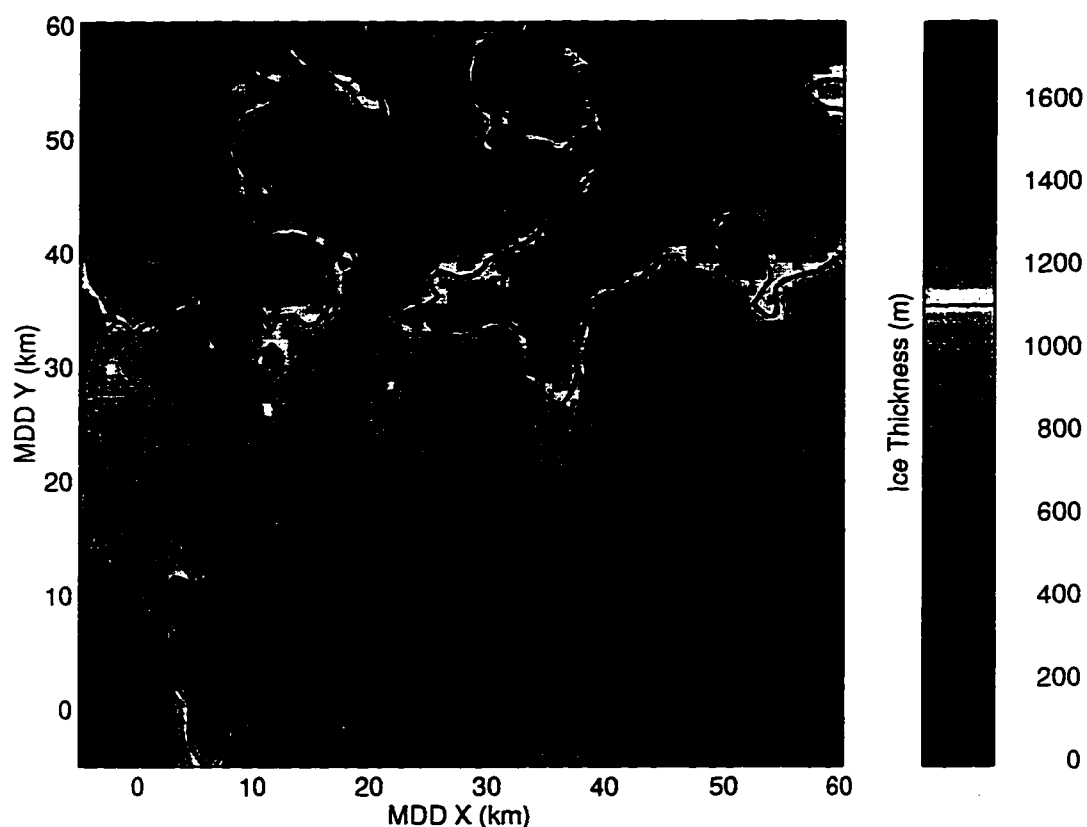


Figure 4.2: Ice thickness map of Taylor Dome region from airborne survey.

package. The resulting ice thickness grid is shown in figure 4.2.

4.3 *Surface elevation map*

The ~ 100 m position accuracy of the C/A-code GPS is sufficient for compiling an ice thicknesses map, but the surface elevations would require more careful integration of the aircraft data streams. Aircraft attitude-corrected laser ranges provide the most precise surface ranges, but there were significant data gaps due to clouds. For this survey, the laser was used exclusively to calibrate the radar surface ranges. The radar showed a range-dependent error which was associated with residual ringing from the outgoing pulse. After removing this effect using an empirical correction formula, the

auto-picker radar surface ranges were shown to be reliable to subsample resolution.

The quality of the GPS data were poor, so the success in solving the kinematic trajectory was disappointing. As a result, three grades of position quality were obtained. In decreasing order of precision, these are: kinematic GPS, differential-pseudo-range (DPR) GPS, C/A-code GPS. For each transect, the “best” position solution was used to calculate the surface elevation. The standard precisions for kinematic GPS is better than 1 meter, while DPR is typically good to 1-5 meters. Barometric pressure was used to define the vertical coordinate for the remaining profiles with only C/A-code positioning.

Figure 4.1 shows the breakdown flight with the three grades of position quality. Fortunately the kinematic GPS positions transects were fairly evenly distributed over the survey. For each of these transects, vertical corrections were found which minimize the surface elevation cross-over discrepancies using a technique similar to Menke (1989, page 190). Vertical corrections for the remaining (poorer position quality) transects were obtained by “bootstrapping”. Next the DPR transects: the GPS solutions were used to interpolate between intersections with the adjusted kinematic transects. Finally, pressures were used to interpolate vertical coordinate for the C/A-code transects between intersections of the adjusted kinematic and adjusted DPR transects. The resulting profiles were grided like the ice thicknesses. Finally, the whole surface was adjusted vertically to correspond to the measured surface elevation at pole 628. This grid was used to generate the contours in figure 4.1 and elsewhere in this dissertation.

Prior to adjusting the kinematic profiles, the rms surface elevation crossover mismatch was 70 cm. Because of the heavy handed vertical coordinate interpolation, which was necessitated by the sparse kinematic GPS coverage, crossover mismatch statistics for the remainder for the survey are useless. Comparing the final surface with elevations measured on the ground at the GPS-survey poles (discussed in section 3) gives an rms discrepancy of 2.7 meters.

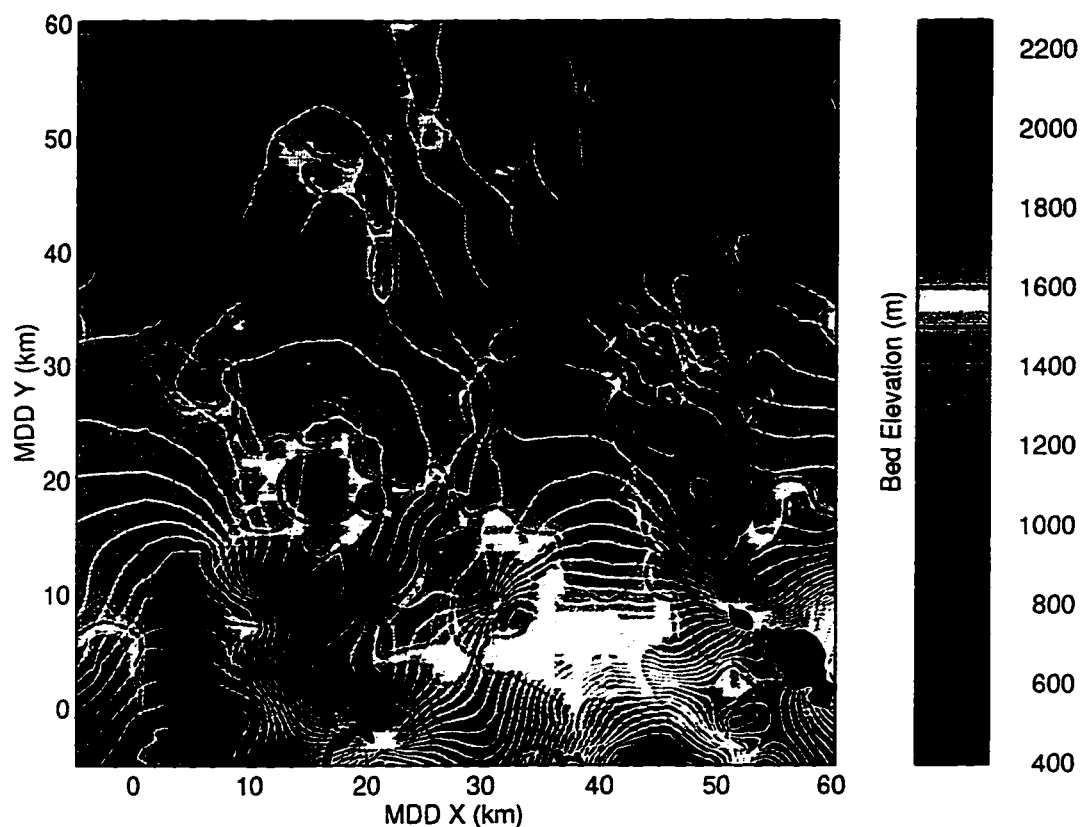


Figure 4.3: Bed elevation map of Taylor Dome region. The surface elevation contour interval is 20 m.

4.3.1 *Bed elevations*

The bed elevation map, shown in figure 4.3, is simply the difference of the surface elevation and ice thickness grids. This map provides a much improved, though smaller scale, view of surface and bedrock topography than was presented by Drewry (1982). The differences stem from the closer line spacing, 5 vs. ~ 15 km, and more precise aircraft positioning. Overall the surface is some 50 meter lower than was previously reported, and the measured topography agrees closely with features visible in LANDSAT imagery (USGS, 1975). Further, the areas of locally steep surface topography coincide with subglacial relief. Referring to figure 4.3, the bed topography clearly

shows that both the Asgard Range (lower right) and the Beacon-Lashly mountain group (bottom center) extend into the east antarctic interior. The Taylor Glacier subglacial trench breaches the Transantarctic Mountains. The saddle at 1500-1600 meters MDD(40,7), separates well developed eastward and westward and troughs. Of the seven sites Drewry identified as subglacial lakes, three are within our survey region, these are discussed in section 5.3. The prominent valley to the north of Taylor Dome, MDD(7,0), does not extend as far west as Drewry indicated, but rather abruptly terminates. This feature is a deep channel which extends into the Portal, and appears to be the western continuation of the Radian lineament identified by Wilson and Bradford (1993).

4.4 Combining ground and airborne radar data

The regional data grids were obtained by fitting a surface to the 5 km spaced profiles and sampling at 750 meter resolution. The ground radar survey was conducted at closer line spacing. In that subregion, higher resolution grids were derived by combining the data sets. The ground profiles have ~30 meter sample spacing, roughly matching the airborne survey. Profiles of ice thickness and surface elevation were combined with equal weighting, binned, fit with a bicubic spline surface, and sampled at 500 meters. These higher resolution grids better resolve the large ice thickness variations present at the ground-based survey region, and are thus used for the flow modeling in the following chapters. Comparing figure 4.4 with the flow-line parallel radar profile (figure 2.5), shows that central subglacial peak over which the core was drilled at MDD(15,19). Down stream from the core, the ice flows over/around another, smaller peak before entering the Portal subglacial trough. Near the eastern edge of the figure, this trough shows 1200 meters of bedrock relief over 5 kilometers.

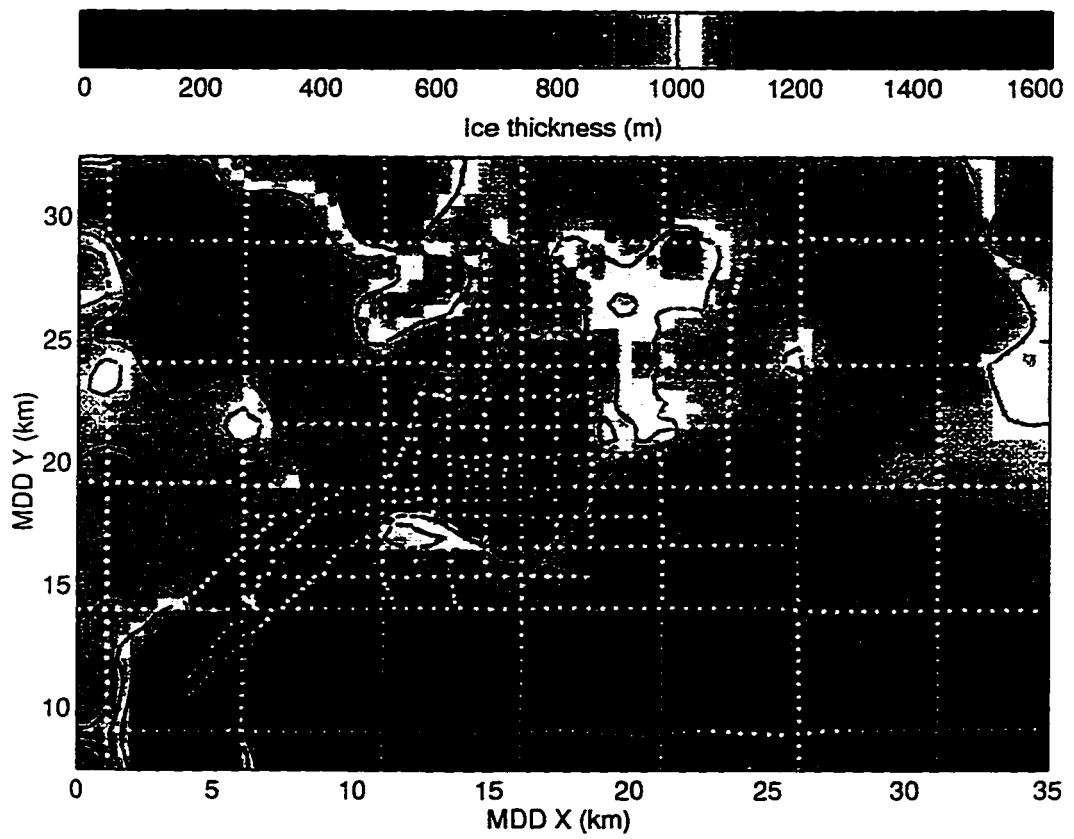


Figure 4.4: Ice thickness and surface elevation of Taylor Dome core-site subregion. Dots show radar profile paths.

Chapter 5

ICE TEMPERATURES AT TAYLOR DOME

In the previous chapters I presented measurement of basic physical parameters fundamental to glaciological research: ice thickness, surface topography, and surface velocity. These are obtained by direct observations of the physical quantities. Another parameter of fundamental importance is temperature. As a direct paleoclimatic indicator, temperatures at depth preserve a record of surface temperature history (Cuffey *et al.*, 1995). The temperature profile in the main borehole was measured in each of the two seasons following drilling (Clow and Waddington, 1996); efforts to directly invert these data for climatic forcing are underway (Clow, *pers. comm.*).

Knowledge of ice temperatures is also required for ice dynamics modeling. Empirical evidence suggests a flow law for secondary creep of ice of the form

$$\dot{\epsilon}_{ij} = A \tau^{n-1} \sigma'_{ij} \quad (5.1)$$

where $\dot{\epsilon}_{ij}$ is the deformation rate, σ'_{ij} is the deviatoric stress, τ is the effective stress, and n is a constant. This is referred to as *Glen's Law*. Reported values for n range from 1.5 to 4.2 (Weertman, 1973). A value of 3 for n is supported theoretically (Alley, 1992), and is usually adopted for large-scale ice flow. The softness parameter, A , depends upon several factors, including temperature, impurity content, and crystal fabric orientation. In temperature, it obeys an Arrhenius relationship; for each 20° C, A changes by about a factor of ten (see for example, Paterson, 1994).

In this chapter, I focus on forward-calculating ice temperatures at depth to provide A estimates for later ice dynamics modeling. Temperature modeling of glaciers has been discussed in many places (eg. Robin, 1955; Paterson and Clarke, 1978).

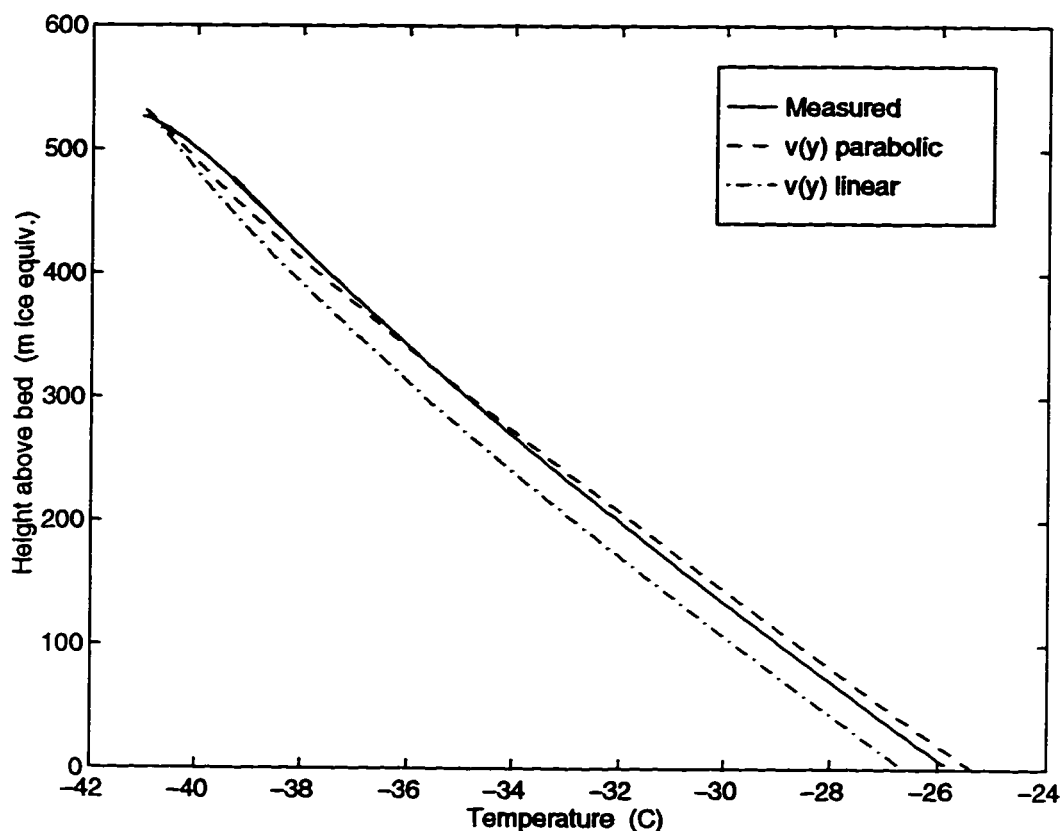


Figure 5.1: Modeled temperature profile compared with borehole measurements (Clow, unpublished data).

What would be an essentially straightforward heat transfer problem is complicated by being coupled with the ice motion equations. While it is possible to solve the problem simultaneously, it is more convenient to separate the dynamics and the thermal equations and solve by iteration. I will apply this approach.

5.1 *The borehole temperature profile*

The Taylor Dome borehole temperature profile is shown in figure 5.1. The downward curvature near the surface is a result of decrease thermal diffusivity in the firn, and plotting in ice equivalent depth units. Otherwise, this profile is nearly linear in depth.

Following the development of Firestone *et al.* (1990), this profile can be modeled in one dimension by assuming that:

- the temperature profile is in steady state
- body source terms, such as strain heating, can be neglected
- the thermal properties are constant in temperature,
- the vertical velocity profile can be approximated by

$$\frac{v(y)}{v_s} = \left[\frac{y}{H} \right]^2$$

where y is the height above the bed, H is the ice thickness, and v_s is the vertical velocity at the surface (equal in magnitude to the accumulation rate).

The one-dimensional steady state heat equation is given by

$$\frac{\partial^2 T}{\partial y^2} - \frac{v(y)}{\kappa} \frac{\partial F}{\partial y} = 0 \quad (5.2)$$

where $\kappa = K/\rho C$, where K , ρ , and c are the thermal conductivity, density, and specific heat capacity, respectively. These quantities are assumed to be constant, their values are taken from Paterson (1994). The integrating factor

$$F(y) = \exp \left[- \int_0^y \frac{v(\xi)}{\kappa} d\xi \right]$$

solves (5.2), which results

$$T(y) = T_s - \frac{Q_g}{K} \int_H^y \frac{1}{F(\eta)} d\eta \quad (5.3)$$

where T_s is the surface temperature and Q_g is the net vertical (geothermal) heat flux at the bed.

The value for Q_g is determined from the temperature gradient at the bed by

$$Q_g = K \left. \frac{\Delta T}{\Delta y} \right|_{y=0}$$

A temperature gradient of $-0.032^\circ/\text{m}$ is observed, which gives a geothermal flux of $77 \text{ mW}/\text{m}^2$. From field observations: $T_s = -41^\circ \text{ C}$, $v_s = .07 \text{ m}/\text{a}$, and $H = 535 \text{ m}$ (ice equiv.). Using these values, equation (5.3) describes the dashed line in figure 5.1. The agreement is very good: the predicted profile is within a degree of the observed throughout the ice column. This is a little surprising since the quadratic profile was determined by Raymond (1983) to be appropriate for isothermal ice divides. Relative to the isothermal case, the softer ice at depth is expected to accommodate increased vertical velocities at depth, increasing the advective cooling. A limiting-case comparison is considered: the profile is calculated assuming constant vertical strain rate. Shown in figure 5.1, this profile is about a degree colder throughout most of the column. The level of discrepancy between these curves would be unacceptable for paleoclimatic inversion, indeed for that application 10 mK-level discrepancies are significant. However considering uncertainty in its tabulated values, a degree is close enough for choosing a value for the rheological softness parameter. As suggested by the linearity of the borehole temperature profile, the thermal regime at Taylor Dome is conduction-dominated, an aspect which is exploited in later calculations.

5.2 Regional extension of the 1-D temperature model

The success of the simple model presented in the previous section at predicting the borehole temperature profile is encouraging. It is now used to estimate ice temperatures throughout the region. To do so, several environmental parameters must be provided: geothermal flux, accumulation rate, surface temperature, vertical strain rate profile, and ice thickness. The geothermal flux obtained from the borehole temperature profile is taken as representative of the entire survey region. The ice thickness is provided by the airborne radar survey (chapter 4). Accumulation rates and surface temperatures are taken from field observations.

5.2.1 Surface temperature

The surface temperature boundary condition is given by the mean annual surface temperature (MAST). Temperature variations at the surface propagate into the firn, decaying in amplitude with depth. For locations with low accumulation rate and no surface melting, the amplitude of the annual temperature signal is generally less than a degree at about 10 meters depth Paterson (1994). Thus 10 meter firn temperatures are taken to be equal to the MAST.

Firn temperatures were measured at the locations shown in figure 5.2. These data are plotted against altitude in figure 5.3. The temperatures span a greater range than expected by considering atmospheric lapse rate effects alone (Waddington and Morse, 1994). In figure 5.2, hashed swipes along topographic crests separate the region into four sectors. Figure 5.3 shows that surface temperatures taken within these sectors fall on separate dry adiabatic lines. Apparently a result of interaction between prevailing weather system directions and local surface topography, distinct climate zones are formed on the different surface-slope facets.

A regional surface temperature map was generated based on surface elevation and local lapse rates. The three lapse-rates shown in figure 5.3 are used in the corresponding sectors of figure figure 5.2. Since no data were collected in the upper right sector, the lapse rate of the upper left sector was used. The temperature discontinuity formed along the divide crest was eliminated by spatial filtering with 10 km wide Gaussian.

5.2.2 Accumulation rate

Observations by field personnel uniformly indicate that surface conditions at Taylor Dome are highly variable, both spatially and temporally. Situated at the edge of the East Antarctic plateau, the site is subject to intense Katabatic winds which funnel through valleys of the Transantarctic Mountains. These winds transport large quantities of snow from the south-west and are primarily responsible for sastrugi for-

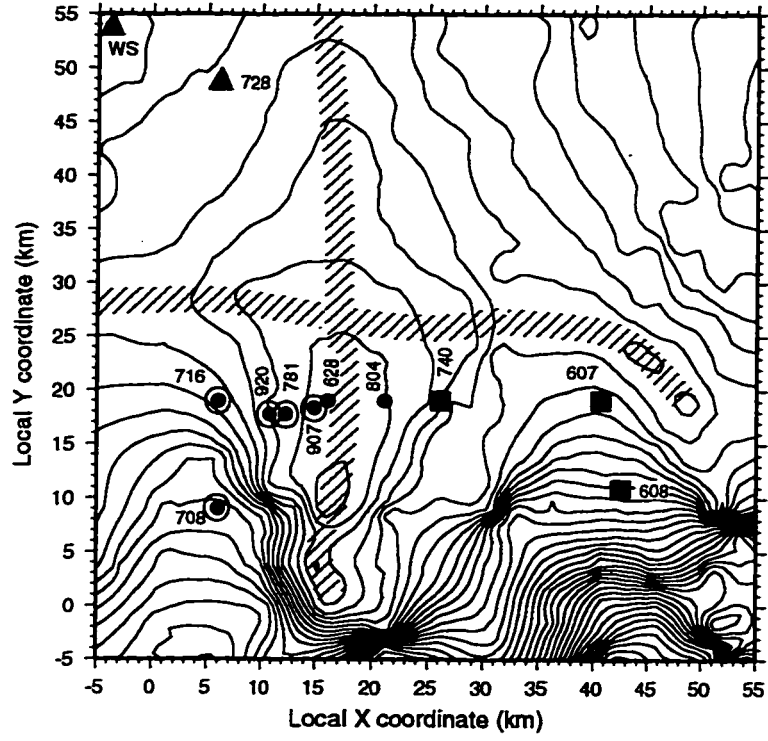


Figure 5.2: Location map of firn temperature measurement. Hatched bands separate micro-climate zones.

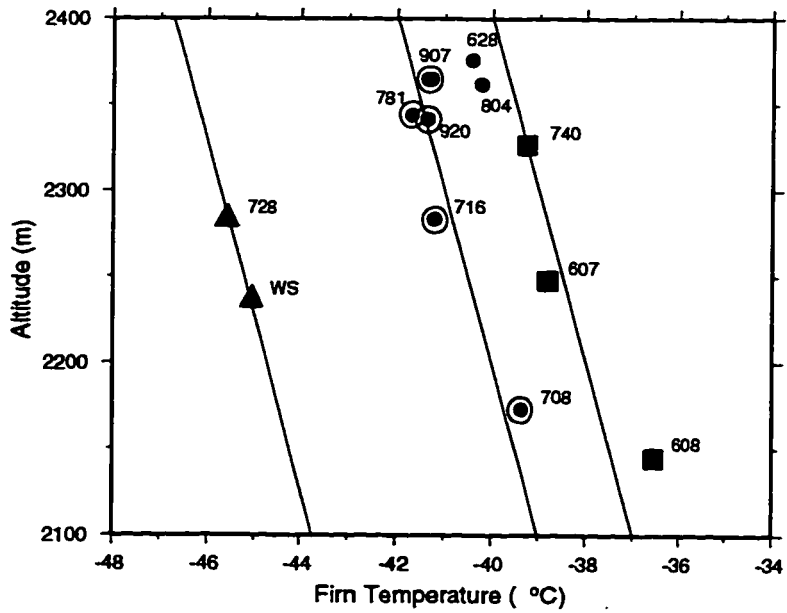
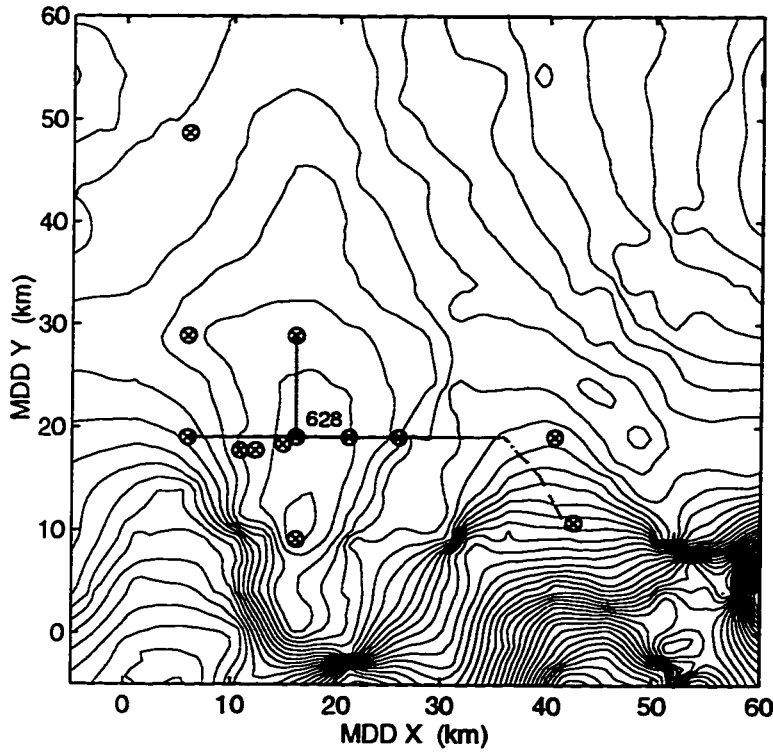


Figure 5.3: Ten-meter firn temperatures

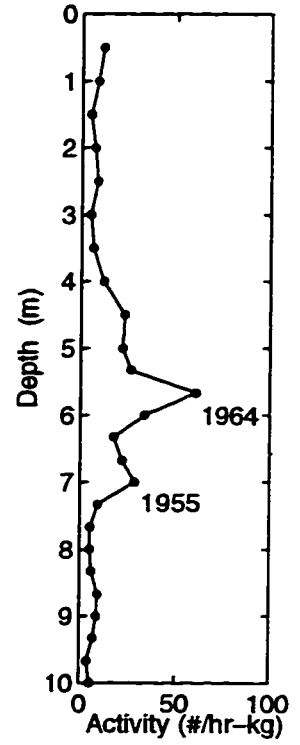
mation and transport. Sometimes they result in net deposition, but most commonly they erode the surface. The primary source of new-snow deposition are synoptic cells which enter the Ross embayment and penetrate the Transantarctic Mtns. from the south. The net annual accumulation is a balance of these two systems. The local topographic "facets" are affected differently by these storm systems. To the south of the dome, the surface is often relatively soft and smooth, suggesting comparatively high accumulation rates. To the north, the surface is characterized by large sastrugi and, in several places, localized patches of net negative balance are present. Consistent with this pattern, shallow radar-internal-layers are relatively deeper to the south than to the north.

As implied by the variable surface character, the accumulation rate is highly variable. This makes measurement of accumulation rate particularly difficult. Accumulation was measured by two different means; the methods, sites, and measured values are summarized in figure 5.4. First, flagged bamboo poles were placed at roughly 300 meter intervals to mark primary travel lines in the survey region. Burial rates of such markers were measured for approximately 50 km of travel lines over successive seasons. Burial depths are converted to ice equivalent accumulation rates assuming a snow density of 0.4 Mg/m^3 . Data from two such lines are shown in figures 5.4(c) and 5.4(d). These data are noisy, likely reflecting very high small-spatial-scale accumulation rate variations, such as the passage of sastrugi.

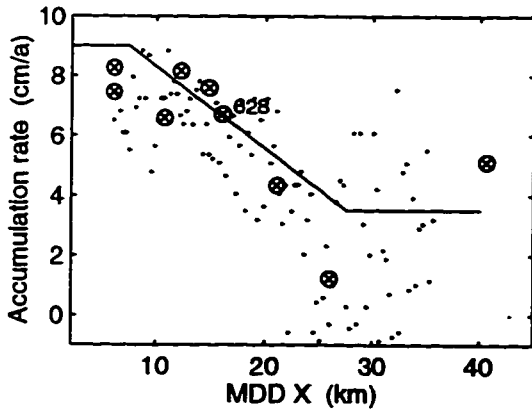
The second means of measuring accumulation rate was by detecting the depth of historic, atmospheric atomic bomb test fallout layers. This is not a new technique for sites with relatively low accumulation rate (*e.g.* Picciotto and Wilgain, 1963). Firn cores, several meters in length, were hand augered at selected sites in the survey region. These were sampled in 0.5 kg sections, melted, and filtered with cation-exchange filters. Peaks in gross- β activity levels of these filters were identified with 1955 initiation and 1964 termination of the bomb test interval. The mass of water above each of the samples was summed, and the accumulation rates were converted



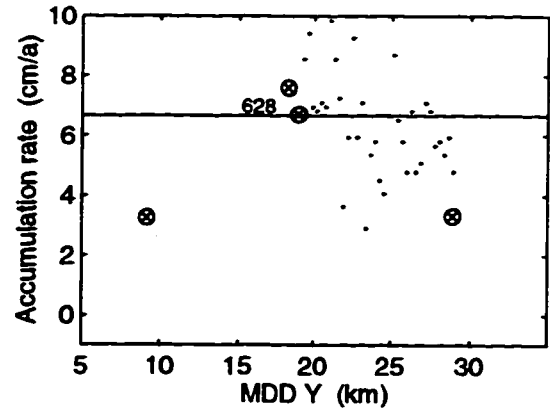
(a) Location map of accumulation rate measurements.



(b) Profile of gross β activity in firn core collected at site 628.



(c) Accumulation rates along Y=19 km.



(d) Accumulation rates along X=16 km.

Figure 5.4: Summary of accumulation rate measurements at Taylor Dome. Dots indicate marker burial rate measurements, and “ \otimes ” show beta activity cores.

to ice equivalent using ice density of 0.92 Mg/m^3 . An example of a β activity profile is shown in figure 5.4(b).

These two methods employed different strategies for coping with the inherently noisy accumulation rate measurement. In the first, spatial filtering was achieved by measuring many markers. In the second, a temporal average is achieved by measuring the total accumulation over the ~ 30 – 40 years since the bomb test era. The two methods yielded consistent results. Figure 5.4(d) suggests decreasing accumulation between $Y=20$ and 30 km, however this is not statistically distinguishable from a spatially constant value. The clearest rate trend is that accumulation rates are high to the south, low to the north. This is demonstrated along the $Y=19$ km line shown in figure 5.4(c). The line drawn through the data in this figure is taken as the accumulation rate function for temperature modeling. It is extended with a constant value below $X=7$ km and above $X=27$ km, where the measurements are less certain or absent. This pattern is assumed to apply at all Y values, which is consistent with other available data (not shown), but is likely simpler than reality. For example, the accumulation rate is likely higher near the entrance to the Portal, and net ablation likely occurs at low elevations where ice enters the Taylor Glacier. However later flow calculations are not sensitive to these errors since surface velocities were not measured in those locations.

5.2.3 Vertical strain-rate profiles

The last element required to extend the 1-D temperature model of section 5.1 over the survey region is the vertical strain rate profile $\dot{\epsilon}_{yy}$. Without the benefit of solving a three-dimensional, fully thermo-mechanical flow model, the vertical velocity profile must be assumed. Raymond (1983) showed that under an isothermal at the divide, the $\dot{\epsilon}_{yy}$ was nearly linear with depth; this led to the parabolic vertical velocity profile used in section 5.1. A variety of other vertical strain rate profiles have been assumed away from the divide (*e.g.* Dansgaard and Johnsen, 1969), the simplest was that of

Nye (1957), who used a profile that was constant with depth. The constant and the linear with depth profiles likely bound the true profile. A comparison of borehole temperature profiles calculated assuming these strain rate profiles is made in section 5.1. The results are similar enough, for the purpose of ice dynamics modeling, to consider them indistinguishable. For simplicity, I assume the constant with depth profile.

5.3 The 1-D temperature field

Using the parameters discussed, the temperature profile model presented in section 5.1 is applied throughout the Taylor Dome survey region. Being a one dimensional model, adjacent profiles are not considered, and the calculation is just repeated at each node using the local environmental parameters. Bed temperatures from the resulting field are shown in figure 5.5, a fairly large range is observed which essentially mirror ice thickness variations.

The borehole profile suggested a geothermal flux of 77 mW/m^2 . This value is consistent with the terrain-corrected value of 80 mW/m^2 reported by Decker and Bucher (1982) for a bedrock borehole at Lake Vida in the nearby Dry Valleys. (They also report, but discount, a higher value of 142 mW/m^2 for the North Fork borehole.) This value is below the range of $100\text{--}146 \text{ mW/m}^2$ reported by Drewry (1982). His calculations relied on an assumed basal melt rate of 2 mm/a at sites he identified as sub-glacial lakes (figure 5.5). Drewry used essentially the same surface temperature, -44° C , and an accumulation rate $\sim 50\%$ higher. But my temperature calculation predicts the bed temperature at site "B" is near -5° C . The vertical thinning profile I use likely errs to make the bed too cold, but only by a few degrees. This in part compensates for fact that temperatures at depth are still responding to the Holocene transition (Clow, *pers. comm.*); the ice is few degrees colder than it would be under steady-state modern conditions. Based on the thermal regime it is not obvious whether basal melting is required at the site. At a depth of 1300 meters, the

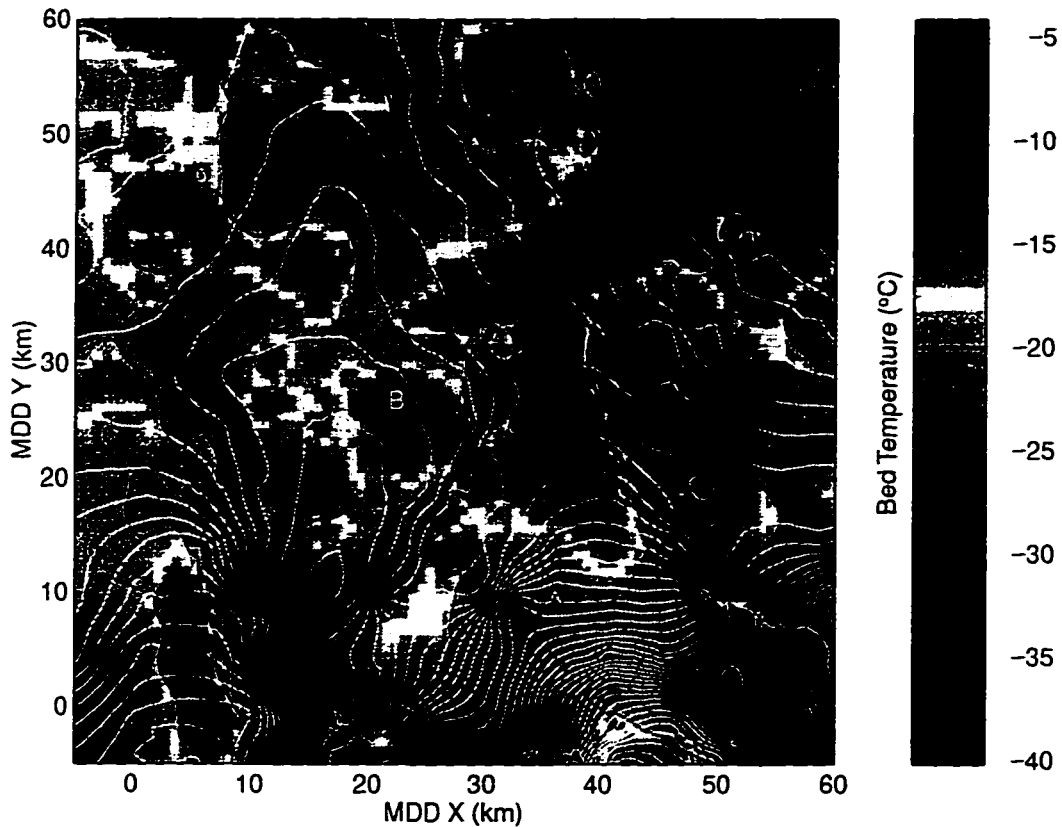


Figure 5.5: Bed temperatures from 1-D calculation. Surface elevations are contoured at 20 meter intervals. Sites “B”, “D”, and “F” correspond to previously identified subglacial lakes.

pressure melting point is about -1°C . The temperature calculation may be in error by the four degrees required for melting. It is also possible that salt concentrations are high enough to further depress the melting point. However, it isn't obvious from the radar profiles that these sites are “lakes”: they are smooth, and perhaps their bed echos are stronger than the surrounding basement, but they aren't flat as Drewry described. As an alternative, it may be that the bed there appears to be a strong reflector purely because it is smooth, likely from ancient warm-based glacial erosion processes, rather than being wet.

Chapter 6

INVERSION OF SURFACE VELOCITY FIELD FOR ICE RHEOLOGICAL PARAMETERS, PART 1: MODEL DEVELOPMENT

A description of ice rheology is fundamental to ice dynamics modeling. The Glen flow law (equation (5.1)) has been empirically confirmed for stresses of 0.5 to 2 bar. While laboratory measurements at stresses lower than 0.5 bar have been reported (Budd and Jacka, 1989), a practical limit is reached in the time required to reliably measure very low strain rates. A conceptual and a mathematical difficulty exists with Glen's Law at very low stresses. In terms of Newtonian fluid mechanics, the quantity, $1/A\tau^{n-1}$, is a viscosity. As the applied stress approaches zero, the viscosity becomes infinite. To overcome this problem, several authors (e.g. Hutter *et al.*, 1981; Lliboutry and Duval, 1985) have suggested a modification to Glen's Law by adding a small constant term which is negligible at large stresses, but which dominates at low stresses.

$$\dot{\epsilon}_{ij} = \frac{A}{1+k^2} (\tau^2 + k^2) \sigma'_{ij} \quad (6.1)$$

In this form, n is taken to be 3, and k has units of stress. I will refer to this as the *generalized* form of Glen's Law. At effective stresses below k , this expression becomes linear in the applied stress with a zero-strain rate viscosity of $(1+k)/2Ak^2$. This relation predicts the same strain rate as (5.1) at an effective stress of one bar.

The two terms in 6.1 have a theoretical basis. Ice primarily deforms by dislocation glide along basal planes. For low stresses, the dislocation density is constant, and linear-viscous behavior is predicted. This is the regime of Harper-Dorn creep (Alley, 1992). Dislocation multiplication occurs at higher stresses. For this regime, Weert-

man (1993) argued that n should be equal to 3. Alley (1992) asserts that “there is little doubt that creep exists with $n = 1$ ”. But it is not clear that linear creep occurs for natural ice. The value of k would determine if linear creep should be observed: if it is greater than about 0.3 bar, then linear creep should be commonly observed, both in nature and in the laboratory; if it is much less than about 0.1 bar, then linear creep would be a nearly insignificant contribution to total deformation.

Ice flow divides provide a natural laboratory for testing the applicability of the generalized flow law since the effective stress there can be very low, below the range of laboratory measurements. An ice divide may be characterized by its stress state, given by

$$\tau_{div} = (2AH/\dot{b})^{-1/3}$$

(Waddington *et al.*, 1996). If $k > \tau_{div}$, then the flow should behave as a linear fluid, if $k < \tau_{div}$ then the flow is non-linear. Raymond (1983) showed that the formation of a region below the divide with reduced vertical strain rate was a consequence of non-linear rheology. This is the familiar “Raymond Bump” which has been discussed by several authors (e.g. Nereson *et al.*, 1996). If such isochron bumps were prevalent features at ice divides, then a strong case would be made for dominance of non-linear rheology at low stress. But at many divides, evidence for such bumps remain equivocal. Such a bump isn’t obvious at Taylor Dome; however two effects may obscure its presence: spatially variable accumulation rate and rough bedrock topography.

A wealth of surface strain rate and geometry data have been collected over six successive field seasons at Taylor Dome. I will use these data to test the generalized form of the flow law. In particular, assuming the value of n to be 3, the parameters A and k are found which best predict the observed surface flow field. To proceed, a model is required which predicts the flow field given the ice sheet geometry. Unfortunately, the very rough bedrock topography at Taylor Dome confounds attempts at ice flow modeling. Presumably a three dimensional, fully coupled thermo-mechanical

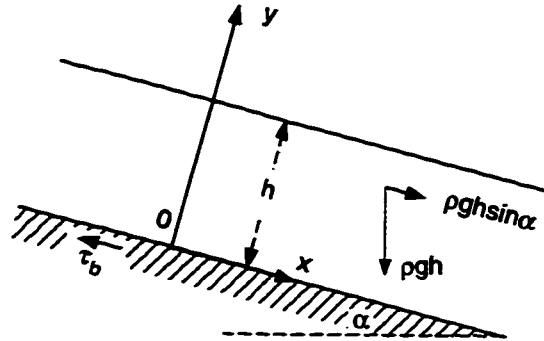


Figure 6.1: Geometry of parallel-sided slab. *Figure adapted from Paterson (1994).*

model could be applied. However, uncertainties in many required input conditions would likely defeat the point of using such a sophisticated model. In any case, such a model would be too computationally cumbersome to be useful as a kernel for an inverse problem: a simpler model is sought.

At the other extreme of complexity, “Laminar flow” is perhaps the most basic and widely used flow approximation used in glaciology (e.g. Paterson, 1994). The configuration is shown in figure 6.1. The glacier is assumed to be an infinite parallel-sided slab, resting on an inclined plane with no slip at the interface. The y -axis is surface normal, zero at the bed and positive up; the x -axis is surface parallel, positive down slope. Since the only stress is bed-parallel, *i.e.* $\tau = \tau_{xy}$, the ice deforms by simple shear. Combining with $2\dot{\epsilon}_{xy} = du/dy$ and the generalized flow law (6.1) yields

$$\frac{1}{2} \frac{du}{dy} = \frac{A}{1+k^2} [\tau_{xy}^3 + k^2 \tau_{xy}] \quad (6.2)$$

At intermediate depths, the shear stress is given by

$$\tau_{xy} = \rho g (h - y) \sin \alpha$$

where ρ is density, g is gravity, h is the slab thickness, and α is the slope. Substituting

into (6.2) and integrating gives the surface velocity

$$u_s = \frac{A}{1+k^2} \left[\frac{\tau_b^3 h}{2} + k^2 \tau_b h \right] \quad (6.3)$$

where $\tau_b = \rho g h \sin \alpha$ is the bed shear stress.

The parallel-sided slab approximation is attractive in its simplicity, but how useful is it for predicting flow over rough topography? Budd (1968) showed that for cases where h or α vary appreciably over spatial scales less than ~ 20 ice thicknesses, the laminar flow predictions poorly match observed surface velocities. Clearly, for short spatial scales, longitudinal stresses associated with bed and/or surface undulations must become important, and the approximation will fail. Several researchers (e.g. Budd, 1968; Bindschadler *et al.*, 1977) have suggested that this difficulty may be overcome by spatial averaging.

Kamb and Echelmeyer (1986) developed a theory for longitudinal stress coupling in one dimension. They showed that the surface velocity along the centerline of a valley glacier could be calculated using laminar flow theory if the local slope α is replaced with an effective slope α^* obtained by a weighted spatial average of the local slopes. Their analytic treatment yielded an exponential-in-distance filter function, which could be approximated by a triangular weighting scheme. Dropping the channel “shape factor” term, their eq. 33 is reproduced here.

$$\alpha^*(x) = \frac{1}{2\ell h(x)^{(1+1/n)}} \int_{-2\ell}^{2\ell} \alpha(x) h(x)^{(1+1/n)} \left[1 - \frac{|x' - x|}{2\ell} \right] dx' \quad (6.4)$$

Kamb and Echelmeyer derive a theoretical coupling length, ℓ , which involves a depth averaged ice rheology. Their expression is inappropriate for application to the current problem for at least two reasons. (1) It would need to be modified for the generalized flow law. And (2), their development was a perturbation expansion in small variations of h and α , which is clearly not the case for Taylor Dome. Nevertheless, the form of (6.4) seems physically reasonable even for large depth and slope variations. Instead of calculating a theoretical coupling length, ℓ , I will solve for it as another minimization parameter along with A and k .

The model proposed above contains highly simplified physics. Both the laminar flow and the stress coupling components assume that shear stresses dominate. The laminar flow approximation using only the local surface slope will certainly fail at the divide since the surface slope goes to zero. Further, the longitudinal stress coupling theory breaks down for spatial scales less than 2–4 ice thicknesses (Jóhannesson, 1992). Despite these weaknesses, I will examine whether longitudinal stress coupling improves the surface velocity predictions of the laminar flow equations at flow divides. Specifically, I test whether the surface velocity calculated by these equations is sufficiently sensitive to the crossover stress k , the softness parameter A , and the coupling length ℓ , that they can be used to invert for those parameters given a measured surface velocity field. To do so, I first use a finite element model to calculate the velocity field for an ice divide with known rheological parameters. Then I invert these “synthetic data” for the underlying rheological parameters.

6.1 The forward problem: finite element modeling of idealized ice divide

The flow field in the vicinity of ice divides was examined by Raymond (1983). For this work, Raymond developed a finite element algorithm which solves for the flow field which satisfies the stress-balance equations. Later, Waddington adapted this code to evolve the surface profile to equilibrate geometry and flow field with an input accumulation rate. Schøtt *et al.* (1992) adapted the code’s viscosity subroutine to the generalized flow law as formulated in (6.1). This finite element model was used to forward-calculate the detailed flow pattern and steady-state geometry in the region of an ice divide. These profiles are used as “data” to test the sensitivity of the inverse model to the input rheological parameters.

6.2 Ice divide model setup

To generate the synthetic data to test the inversion, I did not attempt to simulate a particular divide, but rather I used a fairly “generic” geometry; the ice thickness, H , was about 1 km, the accumulation rate, \dot{b} was set at a constant value of .1 m/a, and the ice was isothermal at -20° C. For this divide, $\tau_{div} \sim 0.2$ bar, which is essentially the same as that for Taylor Dome. This value is appropriate for Siple Dome as well. To avoid the influence of the boundary, the divide was centered in a 20 km wide region. In the vertical direction, 15 nodes were logarithmically-spaced with increasing density toward the bed. The horizontal nodes were at 100 m intervals, providing high spatial resolution in the divide region. Equal spacing avoided a characteristic of this code to produce surface slope and velocity discontinuities at step-changes in node spacing.

A series of model runs were performed using a range of cross-over stresses which span a range that might be observed in nature: $k = 0, 0.1, 0.2, 0.3,$ and 0.4 bar. The models were run forward in time to allow the surface shape to come to equilibrium with the accumulation rate. One year time steps were required to avoid numerical instabilities resulting from the close horizontal node spacing. A computational expedient was achieved by supplying on input a surface profile which was “close” to the eventual equilibrium shape. For the first model run, the input geometry was derived from a Vialov (1958) profile. For subsequent runs, the equilibrated geometry of the preceding run was used. Typically after 300 model-years, the maximum rate of surface elevation change was less than 10^{-4} m/a, and the surface was assumed to be in steady state.

Selected properties from the model runs are shown in figure 6.2. Expectedly, higher k runs evolved to noticeably flatter profiles. Within about one ice thickness of the divide, the surface slope and velocities show that for runs with $k \lesssim 0.2$ bar, a distinct region exists which is indicative of the “divide flow” region noted by Raymond (1983). This is where isochron “bumps” would occur at depth.

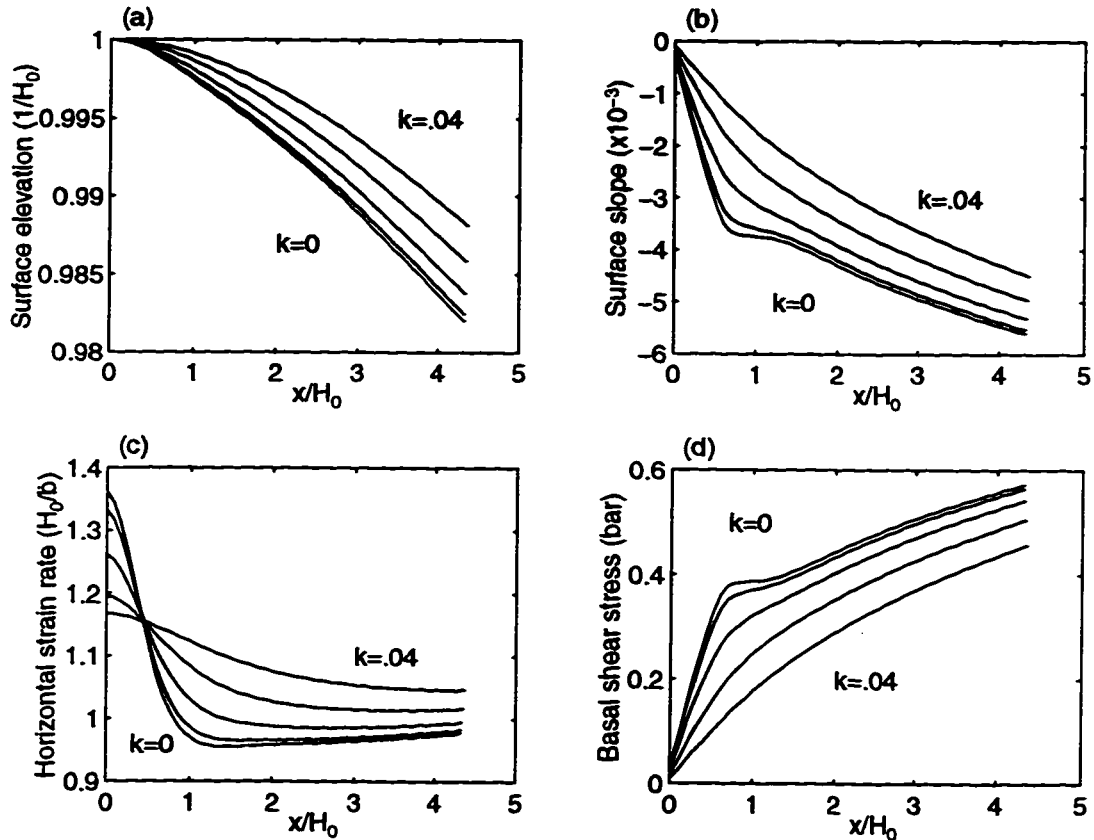


Figure 6.2: Profiles of selected parameters for isothermal divides with $\tau_{div} \sim 0.2$ bar and different values of crossover stress: (a) surface elevation, (b) surface slope, (c) surface horizontal strain rate, and (d) bed shear stress.

6.3 Setting up the minimization problem

Using these profile geometries and surface velocities, I now use the stress-coupled laminar flow model discussed above to invert for the specified ice rheology and effective coupling lengths. The equations for laminar flow using the generalized Glen flow law (6.3) and spatial filtering (6.4) are combined to form a function which predicts surface velocity given ice sheet geometry and flow law parameters. In the terminology of

Parker (1994), this is the *data kernel*, and may be expressed in the generic form

$$u_i^p = \mathcal{G}_i(\mathcal{A}, k, \ell) \quad (6.5)$$

where the data u_i are the surface velocities at points i . For numerical stability, the flow law parameter is non-dimensionalized by its known value, $\mathcal{A} = A/A_{known}$. The stress-coupling length is non-dimensionalized by the ice thickness. The difference between the surface velocity predicted by the FEM calculation (observed) and the velocity predicted by the data kernel, \mathcal{G} , at each evaluation point, i , gives the velocity residual function

$$R = \sum_{i=1}^j u_i^o - u_i^p \quad (6.6)$$

The set of model parameters, \mathcal{A}, k, ℓ , are sought which minimize the root-mean-square velocity residual. This non-linear least squares minimization problem is solved by an iterative, Levenberg-Marquardt algorithm as implemented by the MATLAB optimization toolbox function *leastsq*.

The form of R gives relatively low weighting to velocity discrepancies close to the divide. This was desired since, as noted above, the physical assumptions underlying the data kernel fail at the divide. The sensitivity of the residual function to the model parameters may be evaluated by considering its numerical derivatives in the j model parameters m .

$$J_{ij} = \frac{\Delta R_i}{\Delta m_j} \quad (6.7)$$

Columns of the Jacobian matrix, J are plotted in figure 6.3. Qualitatively these plot show the relative sensitivity of the data kernel to the model parameters, and how that sensitivity varies with distance from the divide. For each of the profiles, the sensitivity of the kernel to \mathcal{A} are nearly the same, each show increasing sensitivity to \mathcal{A} with increasing distance from the divide. The sensitivity to k is similar in form, suggesting that these parameters are coupled, which is apparent by inspection of (6.1). But there are differences in the curves, particularly at low k , suggesting that

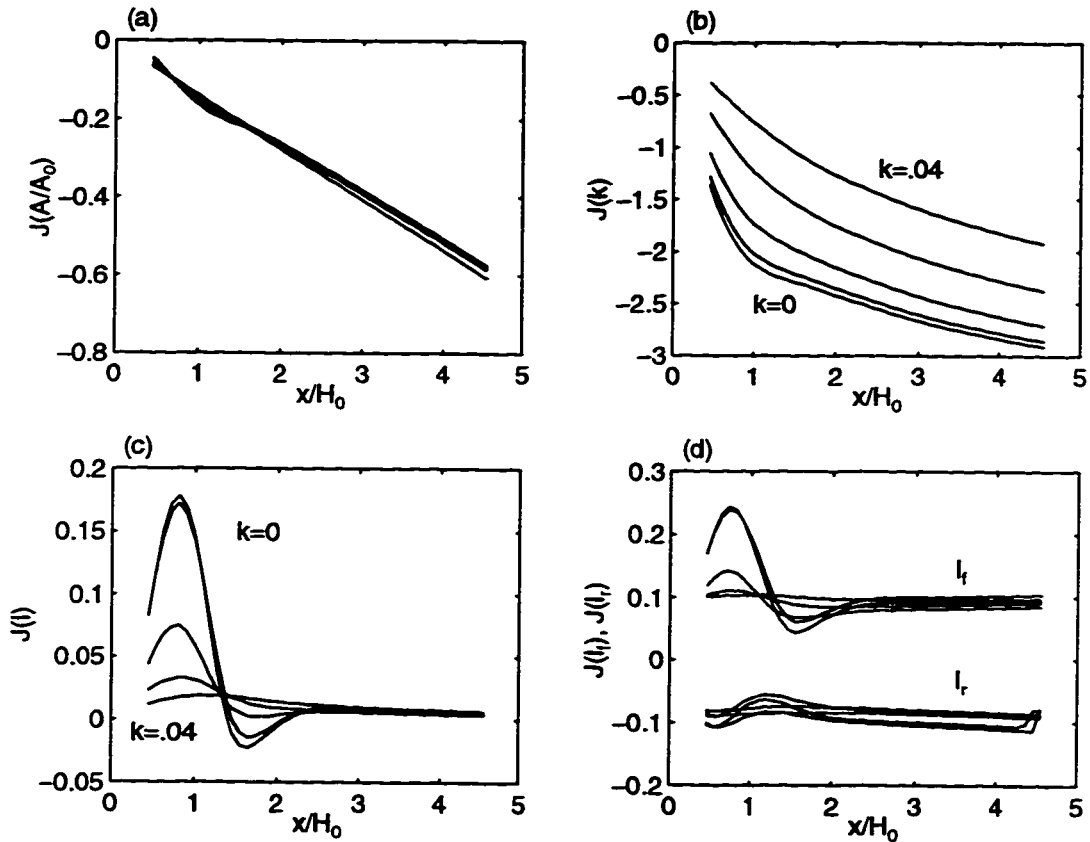


Figure 6.3: Relative sensitivity of the velocity misfit parameter (6.6) to the model parameters: (a) the softness parameter \mathcal{A} , (b) crossover stress, (c) symmetric coupling length, (d) forward and reverse coupling lengths.

a unique solution is possible. For low values of k , the fit has a peak in sensitivity to coupling lengths at about one ice thickness from the divide.

6.4 Idealized-divide flow law parameter fitting

Independence of the parameters was explored by comparing the result of inversion performed by holding some of the parameters fixed and solving for the remaining ones. First, the best fitting \mathcal{A} is found, while holding k and ℓ fixed at zero. Then \mathcal{A} and k are found simultaneously, again with $\ell = 0$. Then k and ℓ are found with $\mathcal{A} = 1$.

In the fourth run, R is minimized in all three parameters, \mathcal{A} , k , and ℓ . Finally, the spatial filtering algorithm is modified to allow two filter lengths corresponding to the up-flow and down-flow directions (ℓ_f, ℓ_r). These two coupling lengths are found while holding \mathcal{A} and k to the values of the fourth inversion run. These five inversions were run for each of the five synthetic profiles. In each of the inversion runs, the surface velocities are fit at each of the FEM model grid points in the range of .25 to 5 H from the divide. Confidence intervals for the model parameters are given by the product of the misfit and the model resolution matrix. This algorithm is implemented using the MATLAB function *confint*. The results of these inversions are listed in table 6.1. Several features are shown in this table:

1. The \mathcal{A} parameter is well determined in all cases other than the \mathcal{A} -only inversions.
2. The cross-over stress parameter k is poorly resolved for $k \leq 0.1$ bar. This is not too surprising since the modeled divide has an effective stress of 0.2 bar: the divide is non-linear for $k < 0.2$. Both the profiles in figure 6.2 and the model sensitivities in figure 6.3 show that there is little difference between the $k = 0$ and $k = 0.1$ curves.
3. For $k \geq 0.1$, the parameter is well determined. However the coupling of k and \mathcal{A} is shown in the better k values when \mathcal{A} is fixed at its known value of 1.
4. Allowing two coupling lengths did not yield a significantly better fit than the single coupling length model.
5. Stress coupling was more effective at improving the velocity fit for low k 's than for high k values.

Table 6.1: Results of synthetic data inversion for FEM input parameters. For each of the runs, several inversions were done with different combinations of free parameters. Softness parameter, \mathcal{A} , is normalized by the input value. The crossover stress, k , is in units of bars. Coupling lengths, ℓ , are in units of local ice thickness. The symmetric, forward and reverse coupling lengths are ℓ , ℓ_f , and ℓ_r , respectively. Discrepancy, R is in $10^{-4} m^2/a^2$. Dittos (") indicate value is fixed from row above. Parentheses on values indicate 95% confidence intervals on the least significant digit.

run	free	\mathcal{A}	k	ℓ	$\ell_f \ell_r$	R
k = 0	\mathcal{A}	1.037(3)				165
	\mathcal{A}, k	1.090(9)	(-)			156
	k, ℓ	$\equiv 1.00$	0.083(2)	0.42(1)		97
	\mathcal{A}, k, ℓ	1.010(7)	0.07(2)	0.41(1)		96
	ℓ_f, ℓ_r	"	"		0.44 0.42	95
k = 0.1	\mathcal{A}	1.101(2)				120
	\mathcal{A}, k	1.082(7)	0.049(9)			119
	k, ℓ	$\equiv 1.00$	0.124(0)	0.42(1)		81
	\mathcal{A}, k, ℓ	1.016(6)	0.114(4)	0.40(1)		80
	ℓ_f, ℓ_r	"	"		0.43 0.41	79
k = 0.2	\mathcal{A}	1.314(5)				238
	\mathcal{A}, k	1.068(4)	0.173(3)			55
	k, ℓ	$\equiv 1.00$	0.206(0)	0.42(1)		49
	\mathcal{A}, k, ℓ	1.036(4)	0.190(2)	0.31(1)		43
	ℓ_f, ℓ_r	"	"		0.35 0.35	43
k = 0.3	\mathcal{A}	1.76(1)				541
	\mathcal{A}, k	1.061(2)	0.275(1)			20
	k, ℓ	$\equiv 1.00$	0.299(0)	0.491(7)		22
	\mathcal{A}, k, ℓ	1.039(2)	0.284(1)	0.33(1)		15
	ℓ_f, ℓ_r	"	"		0.34 0.34	15
k = 0.4	\mathcal{A}	2.59(4)				872
	\mathcal{A}, k	1.051(1)	0.377(0)			7.9
	k, ℓ	$\equiv 1.00$	0.398(0)	0.565(6)		7.0
	\mathcal{A}, k, ℓ	1.027(1)	0.387(0)	0.408(6)		3.2
	ℓ_f, ℓ_r	"	"		0.42 0.42	3.2

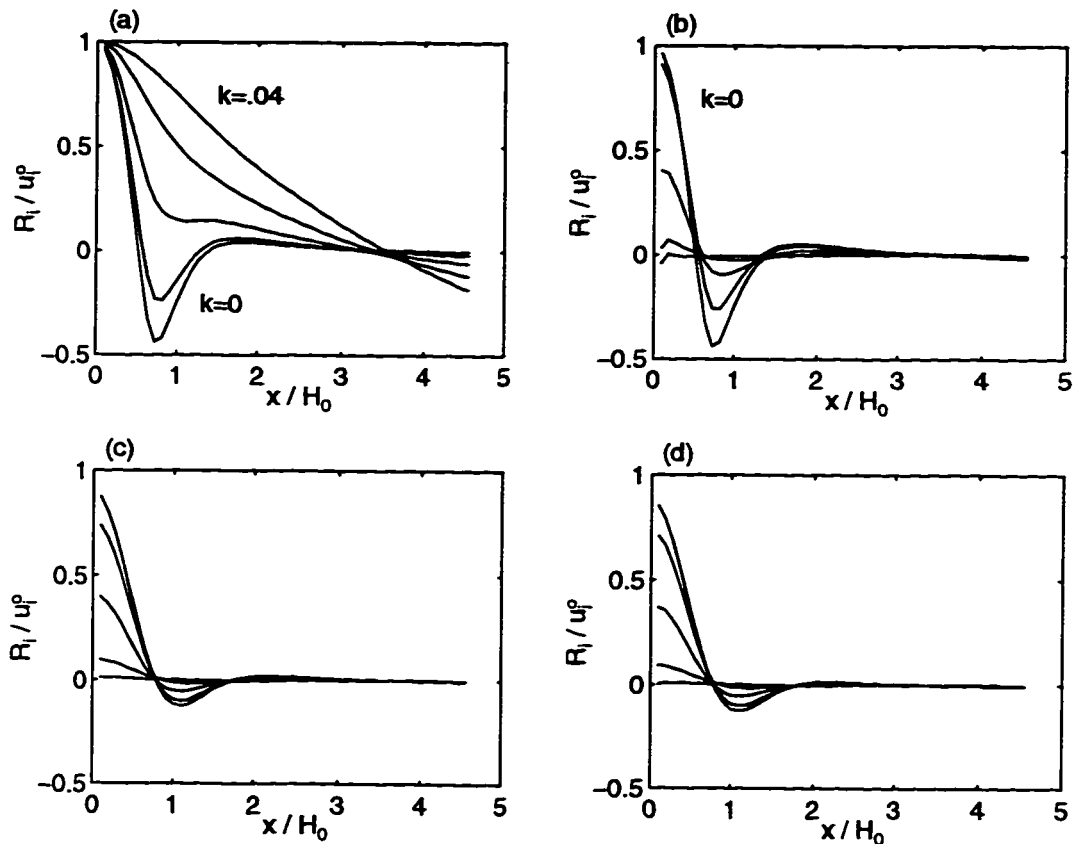


Figure 6.4: Surface horizontal velocity discrepancies for four flow law parameter inversions. Panel (a) is for \mathcal{A} only; (b) is for \mathcal{A} and k ; (c) \mathcal{A} , k , ℓ ; (d) \mathcal{A} , k , ℓ_f , ℓ_r .

6. The stress coupling parameter ℓ was essentially the same for all inversions and k values. The value of $\sim 0.4H$ is less than expected (Kamb and Echelmeyer, 1986).
7. In nearly all cases, the confidence intervals were optimistically small.

The minimized velocity residuals computed for four of these inversions runs are shown in the figure 6.4. In all cases, the velocity predictions were poor for locations within one ice thickness of the divide. For each of the k profiles, the fit using stress coupling was acceptable at distances greater than one ice thickness from the divide.

The agreement of the inverted flow parameters with input values confirm that the proposed model can be used as a data kernel for flow law parameter inversion in the vicinity of an ice divide.

Chapter 7

INVERSION OF SURFACE VELOCITY FIELD FOR FLOW PARAMETERS: PART 2, USING REAL DATA

In the previous chapter, I presented an algorithm for inversion of the surface velocity data for ice rheological parameters at an idealized ice divide. Flow law parameter inversion Taylor Dome is considerably more complicated. First, the bed topography is rough, but filtering should account for these longitudinal stresses. A more fundamental difference lies in the ice rheology itself. Ice is strongly non-isotropic, being nearly an order of magnitude softer to basal plane glide relative to randomly-oriented polycrystalline ice. Non-isotropic flow laws have been proposed (*e.g.* Azuma, 1994), but other than in the ice core itself (see section 8.1.2), the fabric at Taylor Dome is unknown. A fabric development model would be required to predict the fabric away from the core site, and such an endeavor is beyond the scope of this work.

The synthetic data inversion presented in the previous chapter was for an isothermal divide, but at Taylor Dome the bed is roughly 20° warmer than the surface. Explicit inclusion of temperature variations is important for the flow law parameter inversion since ice at depth is roughly a factor of 10 softer than at the surface. In laminar flow theory, the surface velocity is obtained by an integration over depth. The derivation of 6.3 was simplified by assuming that A was a constant. Generalizing 6.3 for temperature-dependent A , the surface velocity is given by

$$u(y) = \frac{2\mathcal{A}}{1+k^2} \int_0^y A(T(y)) [(\rho g \sin \alpha(y-h))^3 + k^2 \rho g \sin \alpha(y-h)] dy \quad (7.1)$$

In this form, I have introduced a new scaling parameter \mathcal{E} , and I have assumed that k is independent of temperature.

I will use 7.1 as the data kernel to invert the Taylor Dome surface velocity data for the crossover stress, k and the enhancement factor \mathcal{E} . The local surface slope and ice thickness in 7.1 are replaced with spatial averaged quantities, thus introducing several additional longitudinal coupling parameters similar to ℓ in 6.4. Thermal modeling will provide estimates of the temperature field. These results will give values of temperature dependent softness parameter, $A(T)$, as tabulated by Paterson (1994). Errors introduced by poorly known temperatures, inaccurate tabulated A values, and other effects such as crystal fabric enhancement will each contribute to the value of \mathcal{E} .

7.1 3-D temperature calculation

I presented a one-dimensional calculation of the temperature field at Taylor Dome in chapter 5.3. Because of the large ice thickness variations over short spatial scales, this solution has horizontal temperature gradients which rival the vertical gradients in magnitude. The flank and divide subregions shown by the dashed outlines in figure 7.1(b) are the focus areas for flow law inversion. Since temperature estimates in these regions are crucial, the dimensionality of the model is increased to three in order to include the horizontal conduction and advection terms which would tend to reduce these gradients.

The finite difference method is used to solve the steady-state heat equation

$$\kappa \nabla^2 T - (v \cdot \nabla) T = 0 \quad (7.2)$$

where κ is the thermal diffusivity, v is velocity, and ∇ is the vector differential operator $(\frac{\partial}{\partial i} \hat{i}, \frac{\partial}{\partial j} \hat{j}, \frac{\partial}{\partial k} \hat{k})$. Rewriting using central differences, this becomes

$$\left\{ \begin{array}{l} (\kappa/\Delta_i^2) (T_{i+1,j,k} + T_{i-1,j,k} - 2T_{i,j,k}) - (U_i/2 \Delta_i) (T_{i+1,j,k} - T_{i-1,j,k}) + \\ (\kappa/\Delta_j^2) (T_{i,j+1,k} + T_{i,j-1,k} - 2T_{i,j,k}) - (U_j/2 \Delta_j) (T_{i,j+1,k} - T_{i,j-1,k}) + \\ (\kappa/\Delta_k^2) (T_{i,j,k+1} + T_{i,j,k-1} - 2T_{i,j,k}) - (U_k/2 \Delta_k) (T_{i,j,k+1} - T_{i,j,k-1}) \end{array} \right\} = 0 \quad (7.3)$$

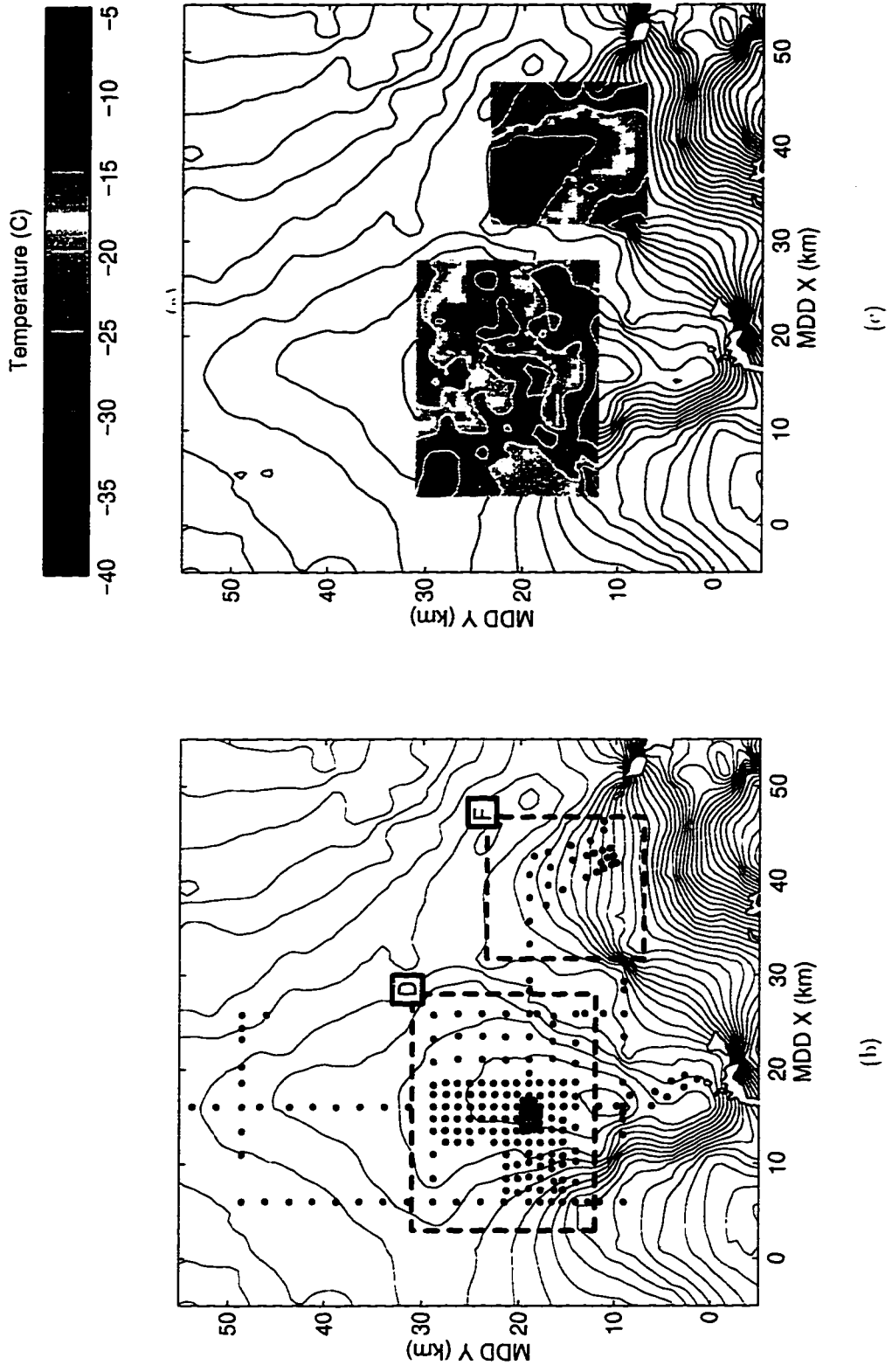


Figure 7.1: Divide and flank subregions used for flow law parameter inversions, Left panel shows motion-marker positions within regions, and right panel shows bed temperatures from 3-D calculation.

Here, the central node is subscripted (i, j, k) , the adjacent node in the $+i$ direction is subscripted $(i + 1, j, k)$, and the distance between these is Δ_i . The regions are already gridded in the horizontal domain with the nodes spaced at 500 meters for the divide grid, and 750 for the flank. Ten equally spaced nodes are used in the vertical direction. This non-orthogonal coordinate system is analogous to “ σ -coordinates” commonly used for atmospheric modeling (*e.g.*, Phillips, 1957). The formulation of correction terms which must be applied to the horizontal derivatives is straightforward. As before, the surface boundary condition is a specified temperature, and the bed boundary has a specified vertical gradient. The vertical boundaries have zero gradient. Equation 7.3 is written for each node in the domain. Together these comprise a system of linear equations which are solved simultaneously using standard MATLAB routines.

The temperature field solution was obtained with an imposed velocity field. In section 5.1 I showed that this is an acceptable approach since the temperature field is dominated by conduction. A “horizontal” velocity profile was given by the laminar flow equations. The profile was resolved into components in the coordinate-system vertical and horizontal directions so the velocity was surface-parallel at the surface, and bed-parallel at the bed. In addition, a constant vertical strain rate was imposed to match the local accumulation rate. The crossover stress was assumed to be 0.2 bar. The resulting bed temperatures are shown in figure 7.1(c), not surprisingly, these look like a filtered version of the 1-D bed temperature map. Under the divide the temperatures are unchanged, while away from the divide the bed topographic highs are warmed and the lows are cooled. The largest temperature differences are of a few degrees on the flanks of steep bed topography.

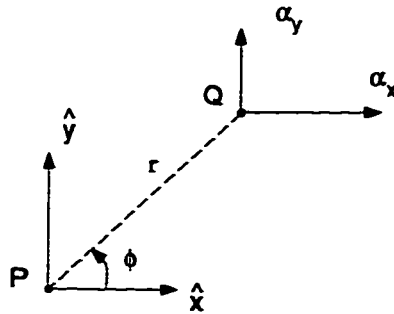


Figure 7.2: Map-view geometry for 2-D spatial averaging. The components of surface slope at Q are α_x and α_y . The effective slope at point P is the direction and distance weighted average slope of all points Q for which $r < 2\ell$.

7.2 2-D stress coupling

Spatially averaged ice thicknesses and surface slopes are used in (7.1) to predict surface velocities. The filter function is patterned after the longitudinal stress coupling theory developed by Kamb and Echelmeyer (1986) in which the weighting decreases linearly to zero at distance 2ℓ . The scheme is generalized to two dimensions by allowing two coupling lengths, ℓ_l and ℓ_t for longitudinal and transverse stresses, respectively. First I define a shorthand notation for the slope spatial filter function given by (6.4) as $\alpha^* = \mathcal{F}(\alpha, \ell)$. Depicted in figure 7.2, the surface slope at nearby points Q is decomposed into components (α_x, α_y) . The slope components are filtered with both longitudinal and transverse weighting and added by

$$\begin{pmatrix} \alpha_x^* \\ \alpha_y^* \end{pmatrix} = \begin{pmatrix} \mathcal{F}(\alpha_x, \ell_l) \cos^2 \phi + \mathcal{F}(\alpha_x, \ell_t) \sin^2 \phi \\ \mathcal{F}(\alpha_y, \ell_l) \sin^2 \phi + \mathcal{F}(\alpha_y, \ell_t) \cos^2 \phi \end{pmatrix} \quad (7.4)$$

This expression reduces to (6.4) for $\ell_l = \ell_t$. The expression for filtering ice thickness is analogous to 6.4.

7.3 Parameter inversion

The flow enhancement parameter \mathcal{E} , the crossover stress k , and the coupling lengths ℓ are found for which eq. (7.1) best matches the observed surface velocities. The minimization is achieved by the same procedure that was presented in the previous chapter. In this case, a 2-D velocity residual function for N observations is given by

$$R = \sum_{i=1}^N [(u_x^o - u_x^p)^2 + (u_y^o - u_y^p)^2]_i \quad (7.5)$$

The “ o ” and “ p ” superscripts indicate observed and predicted values. The least-squares minimization was done separately for the 24 markers contained within the flank subregion, and for the 153 markers in the divide subregion. The resulting parameters are shown in table 7.1. Several inversions were performed by allowing various combinations of free parameters. As expected, inversions with more free parameters gave lower velocity residuals.

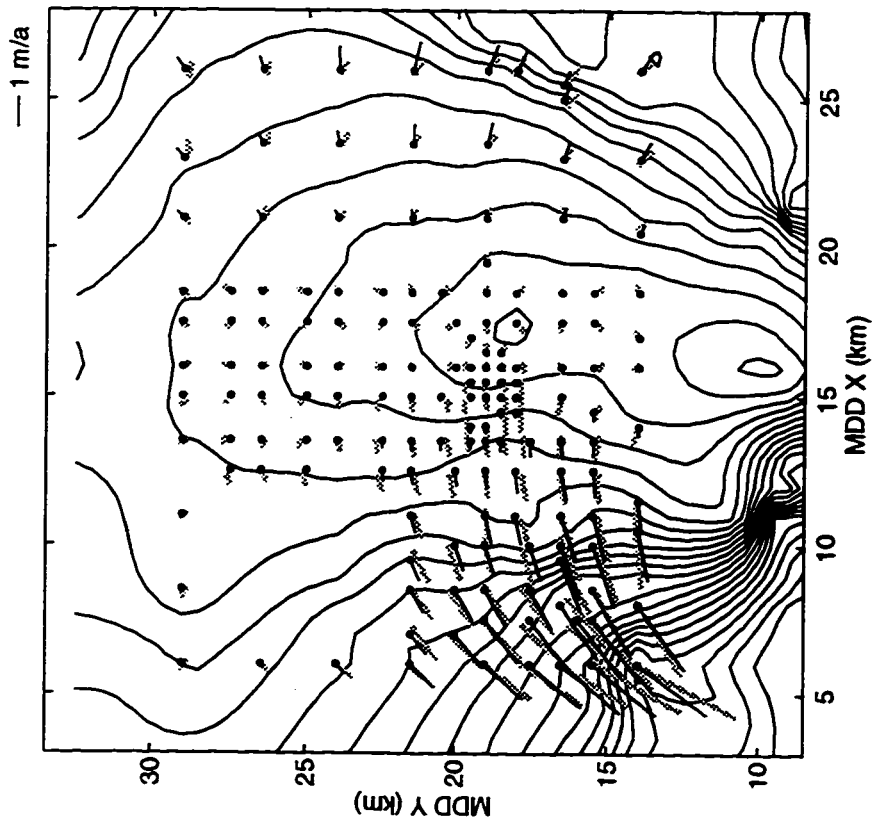
1. The lower values of tabulated misfit parameter, R , argue that both ice thickness and surface slope should be filtered. This is perhaps not surprising in that Kamb and Echelmeyer (1986) filter a combination of h and α . In fact, several of the inversion runs which did not include ice thickness filtering resulted in non-physical (imaginary) values for k .
2. When both slope and ice thickness were filtered, allowing three free parameters, ℓ_i, ℓ_t, ℓ_h didn't achieve an appreciably better fit than just allowing a single coupling parameter. Taking this latter case (inversion run # 6 in the table) as the preferred solution, the rate factor \mathcal{E} for the divide (2.8) and for the flank (3.4) were similar. The slightly higher value for the flank is suggestive of a more strongly developed fabric. The crossover stress of 0.23 and 0.26 bar, respectively, are consistent with expectations (Waddington *et al.*, 1996), and are not taken as distinct.

Table 7.1: Results of surface velocity data inversion. Format is similar to table 6.1. Parentheses grouping free parameters are held equal. \mathcal{E} is unitless, k is in bars, coupling lengths are in units of ice thickness. (Formally, the value of k^2 was determined in the inversion, values of k are also shown for clarity of discussion.)

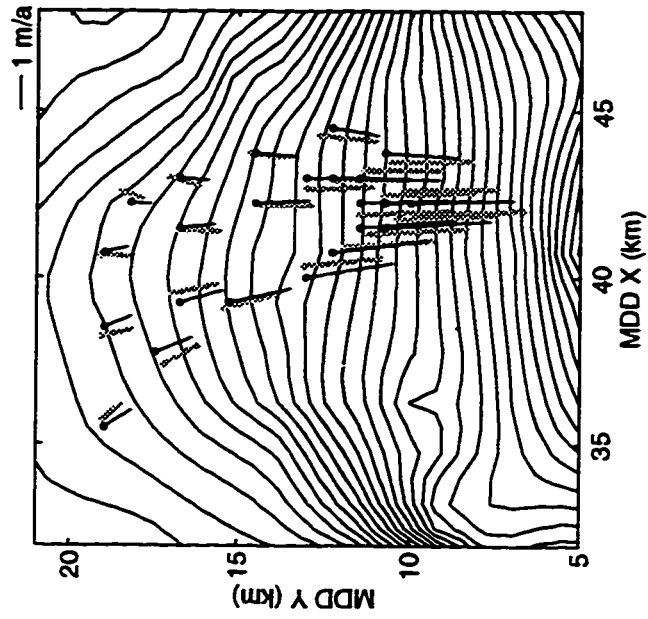
#	free parameters	\mathcal{E}	k^2	k	$l(l_i, l_t)$	l_h	R
Divide							
1	\mathcal{E}	0.43(1)					79.4
2	\mathcal{E}, k	0.62(1)	4.0(6)	2.0			50.7
3	$\mathcal{E}, (l, l_h)$	3.35(5)			4.60(5)	l	8.34
4	\mathcal{E}, k, l	0.94(2)	0.57(5)	0.75	2.12(7)		26.1
5	\mathcal{E}, k, l_h	0.71(2)	4.1(7)	2.0		2.1(2)	47.1
6	$\mathcal{E}, k, (l, l_h)$	2.84(5)	0.054(5)	0.23	4.31(5)	l	7.70
7	\mathcal{E}, k, l_i, l_t	0.91(1)	0.63(4)	0.79	0.80(9), 2.22(7)		27.8
8	\mathcal{E}, k, l, l_h	3.02(6)	0.042(5)	0.20	4.41(5)	3.8(1)	7.60
9	$\mathcal{E}, k, (l_i, l_h), l_t$	2.94(6)	0.060(5)	0.24	4.82(6), 3.48(7)	l_i	7.14
10	$\mathcal{E}, k, l_i, l_t, l_h$	3.07(5)	0.053(5)	0.23	4.81(5), 3.67(5)	4.2(1)	7.04
Flank							
1	\mathcal{E}	0.98(3)					18.6
2	\mathcal{E}, k	0.98(4)	0.00(6)				18.6
3	$\mathcal{E}, (l, l_h)$	3.61(7)			8.9(1)	l	1.22
4	\mathcal{E}, k, l	1.35(5)	-0.17(3)		2.3(2)		12.0
5	\mathcal{E}, k, l_h	2.7(2)	-0.04(2)			9(1)	11.6
6	$\mathcal{E}, k, (l, l_h)$	3.35(6)	0.070(7)	0.26	9.05(9)	l	0.82
7	\mathcal{E}, k, l_i, l_t	1.37(4)	-0.06(2)		8.0(3), 0(2)		6.09
8	\mathcal{E}, k, l, l_h	3.68(5)	0.064(6)	0.25	8.82(8)	13(1)	0.64

3. Since τ_{div} for Taylor Dome is 0.2–0.3 bar, the linear and non-linear terms both contribute to the flow, and a small “Raymond Bump” should be present.
4. The coupling length of about $4H$ is comparable to averaging lengths determined elsewhere Bindschadler *et al.* (1977); Kamb and Echelmeyer (1986), but the coupling length of $\sim 9H$ at the flank seems long.
5. The transverse coupling length is expected to be shorter than the longitudinal coupling length Raymond (1996). There is a tendency for relatively smaller values of ℓ_t . However, the minimization procedure had difficulty with separate coupling lengths. For example, the divide run # 7 appears to have identified a local minima. Thus I have little confidence in this result.

Surface velocities predicted using the preferred values for \mathcal{A} , k and ℓ , are compared with the measured stake velocities in figure 7.3. There is a systematic direction discrepancy in the upper-left portion of the divide site map. Measurements show that the flow is at about 45° to the right of maximum surface slope, toward the Taylor Glacier drainage. The longitudinal stress coupling was unable to predict this direction for any combination of coupling lengths. Otherwise, the visual agreement of the predictions with the observed motion is very good (except, of course for the very low velocities at the divide.)



(a) Measured and "best" fit velocity vectors at divide site.



(b) Measured and "best" fit velocity vectors at divide site.

Figure 7.3: Surface velocities from motion survey (thick) compared with velocities predicted using preferred fit parameters (thin). The motion poles are shown in their relative locations, the predicted velocities are shown at the nearest corresponding grid point.

Chapter 8

REFLECTIONS ON TAYLOR DOME RADAR PROFILING

Presentation of radar data in the chapter 2 emphasized measurement of bedrock topography. Site selection was motivated by “simple” internal layer structure. In the next chapter, the pattern of the internal layering is used to infer spatial and temporal accumulation rate variations. This chapter presents a semi-quantitative analysis of several interesting aspects of the radar profile. These are interesting in their own right, and they provide some support for the later analyses.

8.1 Core-site radar

The location for the main core was established during the 92/93 field season. An approximately 100 meter square area was marked with flagged bamboo poles to identify the site. In that season, the opportunity was taken to collect radar profiles of the core site prior to staging of drilling equipment. Profiles were collected along the perimeter and across the two diagonals with ~ 2 meter record spacing using 5 MHz antennas. Because of such dense sampling, these profiles are the best data obtained at Taylor Dome with which to compare with properties measured in the core.

One such diagonal profile is shown in figure 8.1. The right panel shows the full profile in “ \mathcal{Z} -scope” form; the left, “ \mathcal{A} -scope”, trace was formed by stacking the center 20 waveforms of the profile. An analog filter stage on the receiver preamplifier had a pass-band of 1–10 MHz. An artifact of this filter stage is that the first approximately $1.5 \mu\text{s}$ of the record are obscured by saturation effects. The bottom echo arrives at

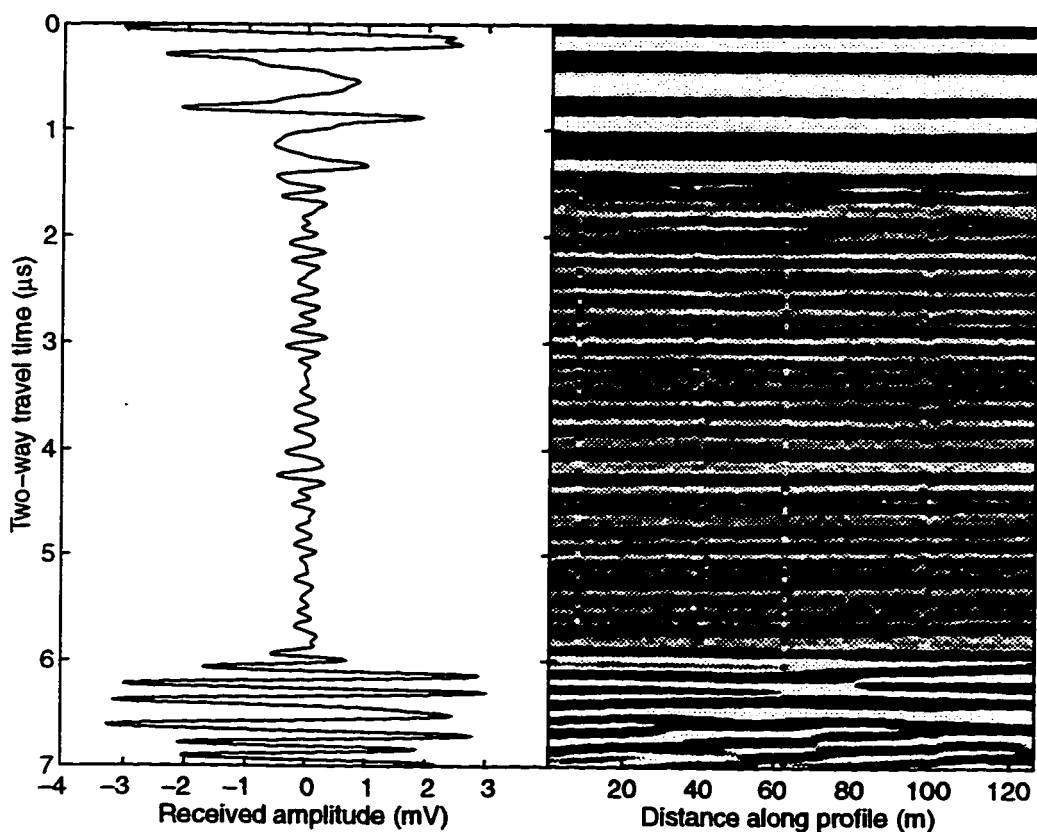


Figure 8.1: Radar data from the main core site. In the left image, the vertical axis is travel time, and the horizontal is received amplitude. Time zeros is defined by the arrival of the direct (air) wave. The right image is a profile of 78 adjacent traces collected on a ~ 140 meter diagonal traverse the core site. In this image, received amplitudes are interpreted as colors. (These display formats are called “A-scope” and “Z-scope”, respectively.)

approximately 6 μs , corresponding to an ice thickness of about 530 meters. Prominent internal reflecting horizons are evident right down to the bed.

Considerable attention has been devoted to investigating the cause of the ice electrical properties variations which result in these internal reflections (Gudmandsen, 1975). Conductivity variations resulting from acidic fallout of volcanic events (Paren and Robin, 1975) are widely thought to be the most likely cause. However at Dome C, Antarctica, Millar (1981) showed that ice density variations could be responsible for layers as deep as ~ 1500 meters. Additionally, crystalline ice is birefringent; Fujita and Mae (1994) showed that variations of crystal fabric orientation can produce layer reflection coefficients comparable to those from conductivity and/or density variations. Widespread radar profiling of the Greenland and Antarctic ice sheets reveals extensive internal layers with power reflection coefficients (PRC) in the range of -60 to -85 dB being typical (Harrison, 1973; Gudmandsen, 1975; Neal, 1976).

The core-site profiles were collected with the same equipment configuration as was used on McMurdo Ice Shelf, only the amplifier gain was changed. The "effective power" calibration from the ice shelf measurements (section 2.2) can be used to estimate the reflectivity of horizons observed on Taylor Dome. To accomplish this, a value for bulk ice conductivity is required to correct for attenuation. Bottom echo amplitudes were measured for 70 kilometers of profiles with ice thicknesses ranging from 500 to over 1500 meters. By the procedure outlined in the earlier section, the slope of a linear fit of amplitude vs. thickness yields an effective ice conductivity of 8.7 $\mu\text{S}/\text{m}$. This value is about a factor of 2 smaller than was measured on the ice shelf, and it agrees well with the value of 10 $\mu\text{S}/\text{m}$ that Glen and Paren (1975) measured in polar ice. Using this value, and (2.2), the echo amplitudes of selected continuous reflectors visible in figure 8.1 are used to calculate the PRC values shown in figure 8.2.

The estimated PRC values for internal layers at Taylor Dome are consistent with layers observed elsewhere. This does serve to validate the system calibration proce-

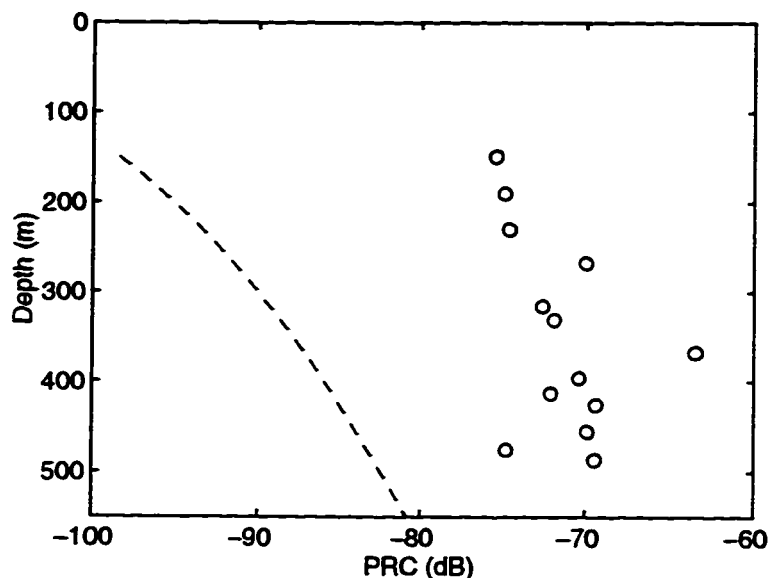


Figure 8.2: Power reflection coefficient of radar reflectors at coresite. The dashed line is the PRC at the noise threshold.

ture; however, the observed PRC values provide little constraint on the reflector's physical characteristics. Indeed, these reflection coefficients are quite small, and only subtle variations in ice properties are needed to cause them. Such variations are common in ice cores. Using the Fresnel reflection equations outlined in appendix A, Weertman (1993) calculated a PRC of -72 and -74 dB for reasonable variations in conductivity and density, respectively. Moore (1988) developed a technique for measuring high-resolution profiles of dielectric properties in ice cores. In principle, such measurements could identify the cause of individual reflectors; however, in practice such attempts have been frustrating. An important difficulty is that the radar samples a much larger region of space than the ice core. The wavelengths are long compared to the scale of variations in ice properties, thus a radar-observed "layer" likely represents a sum of reflections from multiple interfaces.

8.1.1 Comparison with ice core electrical properties

Qualitative comparison of the radar data with ice core properties is made in figure 8.3.

In this figure, the radar profile of figure 8.1 is reproduced along with the other, intersecting diagonal profile. These profiles are compared with the direct current (ECM) and 1 MHz (DEP) electrical conductivity profiles (Taylor *et al.*, 1996), the sulfate concentration profile (Mayewski, unpublished data), and the sonic velocity profile (Fitzpatrick, 1994). In addition, the $\delta^{18}\text{O}$ profile is shown for visual reference to the climatic period. Conductivity spikes, such as near 170 m are attributed primarily to acidic fallout associated with volcanic events, and have corresponding SO_4^{2-} concentration spikes. Qualitatively, several radar internal reflections appear to be associated with observed variation of other core properties. The prominent reflecting horizon between 350 and 400 meters appears to be coincident with the Holocene transition, which occurs at 374 meters. This is perhaps not surprising since the crystal fabric and the core chemistry change dramatically at that horizon. Another prominent reflector at about 270 meters appears to correspond to a large DEP spike. However, corresponding ECM and SO_4^{2-} spikes are not impressive. Indeed, other ECM, DEP and SO_4^{2-} spikes are not obviously identified with radar echos. Independent attempts by the author, and by K. Taylor were unsuccessful at convincingly identifying radar "layers" with the measured electrical properties profiles (Taylor *et al.*, 1996, in prep.). A significant contributor to these difficulties was the poor core quality below about 350 meters, measured value discontinuities at the core breaks were, in many cases, as large as signal variations measured within intact sections. The density profile was not measured continuously, so reflection coefficients could not be calculated.

8.1.2 Crystal fabric layers

The radar data do not distinguish density from conductivity layers, but they can, under certain conditions, identify fabric layers. Single crystal ice has a *p*-wave ultrasonic

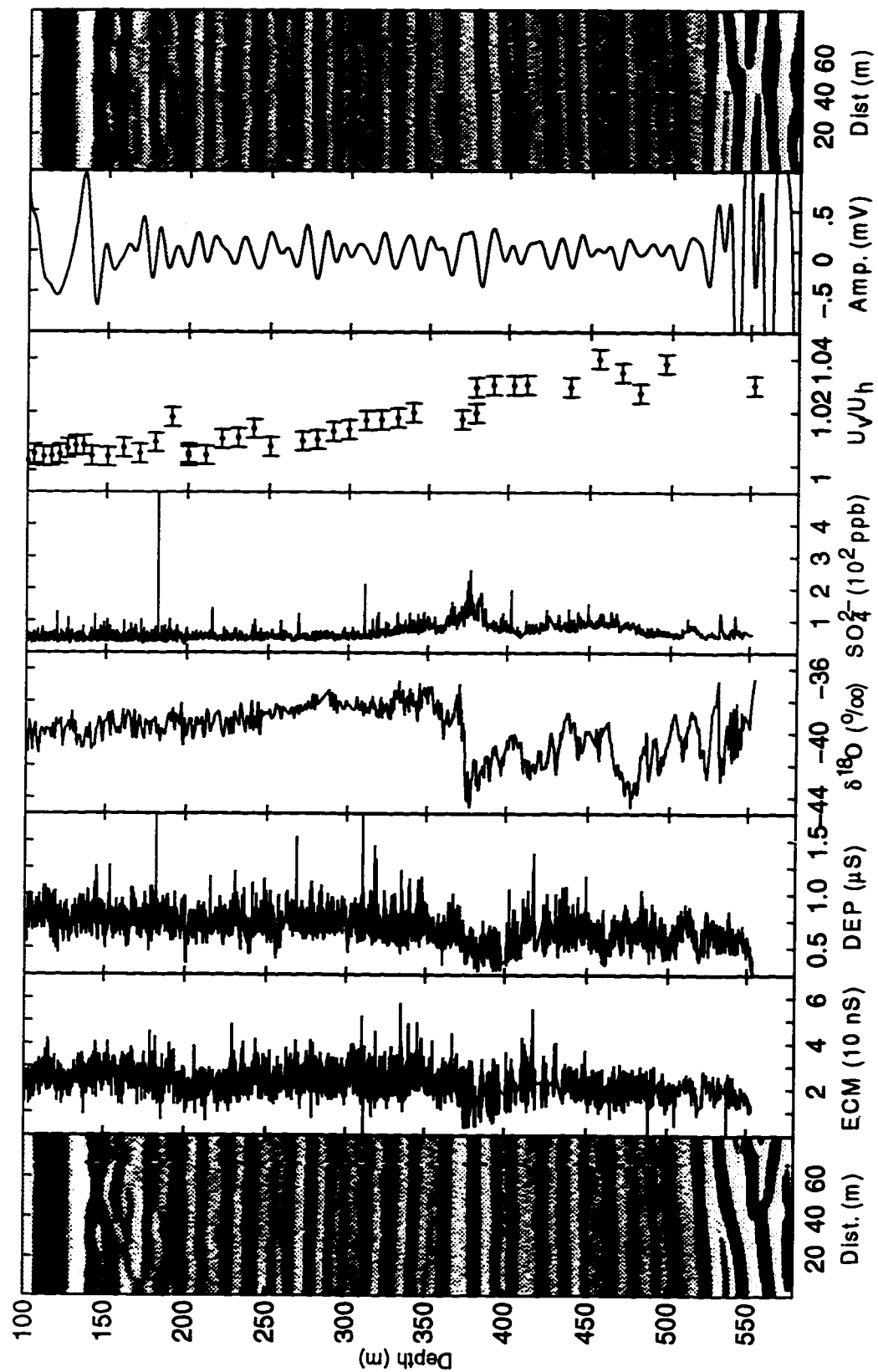


Figure 8.3: Intersecting core-site 5 MHz radar profiles compared with profiles of: ice core electrical properties (ECM and DEP Taylor *et al.*, 1996, in prep.), $\delta^{18}\text{O}$ (Grootes *et al.*, 1996, in prep.), SO_4^{2-} (Mayewski, unpublished), and sonic velocity ratio (Fitzpatrick, 1994).

velocity anisotropy of about 4% (Anandakrishnan *et al.*, 1994). Ultra-sonic velocity measurements (Fitzpatrick, 1994), shown in figure 8.3, have vertical/horizontal p -wave velocity ratios near 1.03. This suggests the presence of highly oriented fabric deep in the core. Depths showing sharp transitions in fabric are the most likely candidates for fabric-caused radar reflections. These are the spike at ~ 180 meters, and the Holocene transition at 374 meters. The spike near 180 meters does not correspond to a “bright” internal layer. Indeed, three radar internal layers near that depth have nearly equal PRC. Moreover, the strongest PRC other than at the transition, occurs at about 230 meters, where there is no sharp fabric transition.

The bright reflection coincident with the Holocene transition is more problematic. The electric permittivity of ice normal to the c -axis differs by about 1% from the c -axis parallel value. The interface of perfectly oriented, c -axis vertical and c -axis horizontal half-spaces would have a PRC of about -50 dB. The reflection which occurs at the Holocene transition is well within the range of what could be caused by the crystal fabric variations. But, the reflection coefficient of a fabric interface will depend upon the polarization of the incident wave relative to the fabric. Fujita and Mae (1993) reported that the detection of internal layering near Mizuho Station depended upon antenna polarization.

Under a radial divide, a fabric is formed which is axially symmetric about the vertical Alley (1992). Variations of the cone-angle of such a “girdle” fabric would give rise to internal layers with a reflection coefficient that is insensitive to the horizontal-plane radio-wave polarization. However, if the divide isn’t radially symmetric, then longitudinal extension along one direction dominates, and an asymmetric fabric develops. A fabric profile of the GISP2 core (Anandakrishnan *et al.*, 1994) shows a maximum cone angle eccentricity of 0.7. If radar internal layers are caused by variations of such a fabric, then these layers would show polarization-dependent internal layering.

The surface strain rate pattern between the divide and the core site at Taylor

Dome is dominantly extensile along flow (see figure 3.4). A complete crystallographic profile of the Taylor Dome core has yet to be completed; however, preliminary analysis (Fitzpatrick, *pers. comm.*, 1997) suggests that a flow-oriented fabric transition occurs at the 375 meter depth. If this fabric interface is responsible for the reflections associated with the Holocene transition, then the reflection strength should be sensitive to the radar polarization. During the 92/93 field season, a polarization experiment was performed at the core site in an attempt to observe such an effect. A series of radar traces were collected while stepping the transmitter and receiver orientations by 15° increments through a full 180° rotation. A “Z-scope” image of these data are shown in figure 8.4. Each of the internal reflecting horizons shown in figure 8.1 are evident in this suite. Amplitudes of returns from selected layers are shown figure 8.5.

The examined internal layers did not show an obvious change in “brightness” of the varying polarization. This suggests, but does not conclusively prove, that the layers are not caused by fabric. Indeed the considerable amplitude scatter is evident, and the signal may be lost in the noise. Detailed fabric analysis are required before reliable estimates of expected PRC variation with polarization can be made.

At this point, the physical properties which give rise to the radar internal layering have not been identified. The difficulty is not in finding a possible cause of the reflection. Rather, the reflection coefficients are very small, and it is easy explain the reflections by several means. Later analyses do not depend on the cause of the internal reflections, only their relative spacing. Specifically, in the next chapter I assume that whatever their cause, the internal layers are constant time horizons. If the reflectors result from depositional processes, such as conductivity variations due to chemical composition, or density variations perhaps caused by accumulation rate or surface temperature variations, then this assumption is likely valid. If however, the reflections are caused by post-depositional processes, in particular if the layers are from fabric, then the assumption may be questionable. This is because ice crystal fabric and the flow field are coupled. Oriented fabric is formed as the ice undergoes

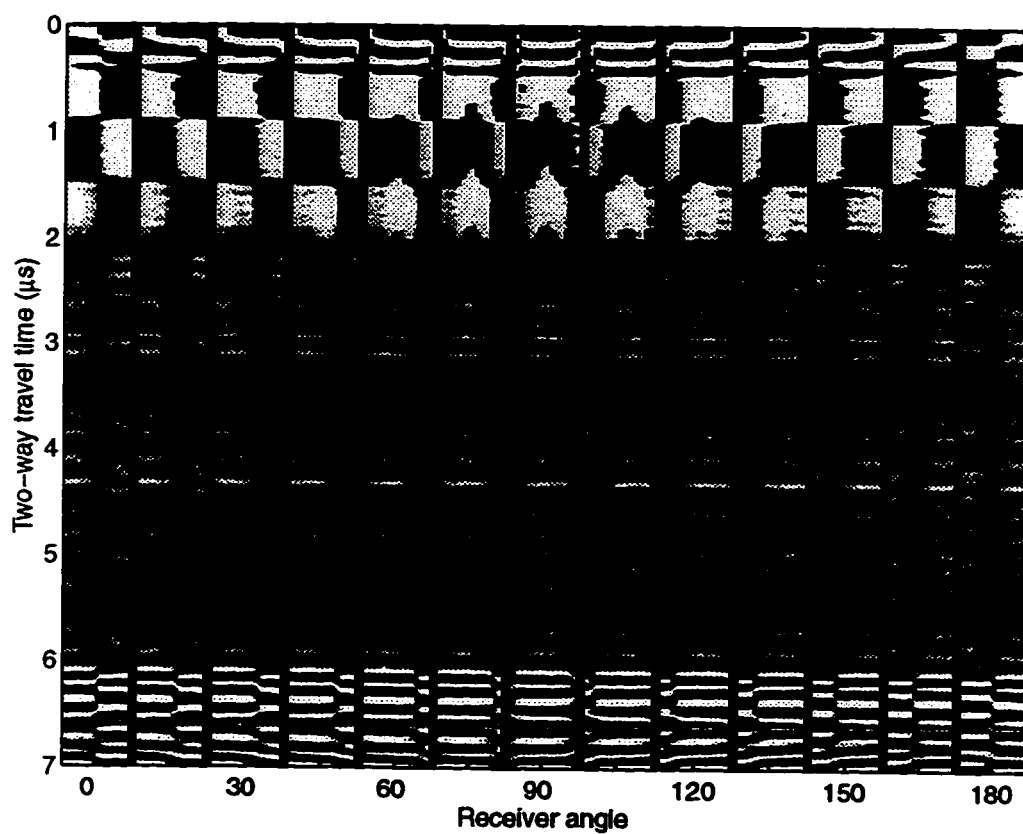


Figure 8.4: Z -scope image of 5 MHz polarization sweep at core site. The data are grouped by common receiver angle, within each segment the transmitter angle is swept through 0 – 180° in 15° increments. The 0 and 180° panels correspond to flowline-parallel receiver polarization; for these angles, antenna cross-polarization occurs in the center of the segment.

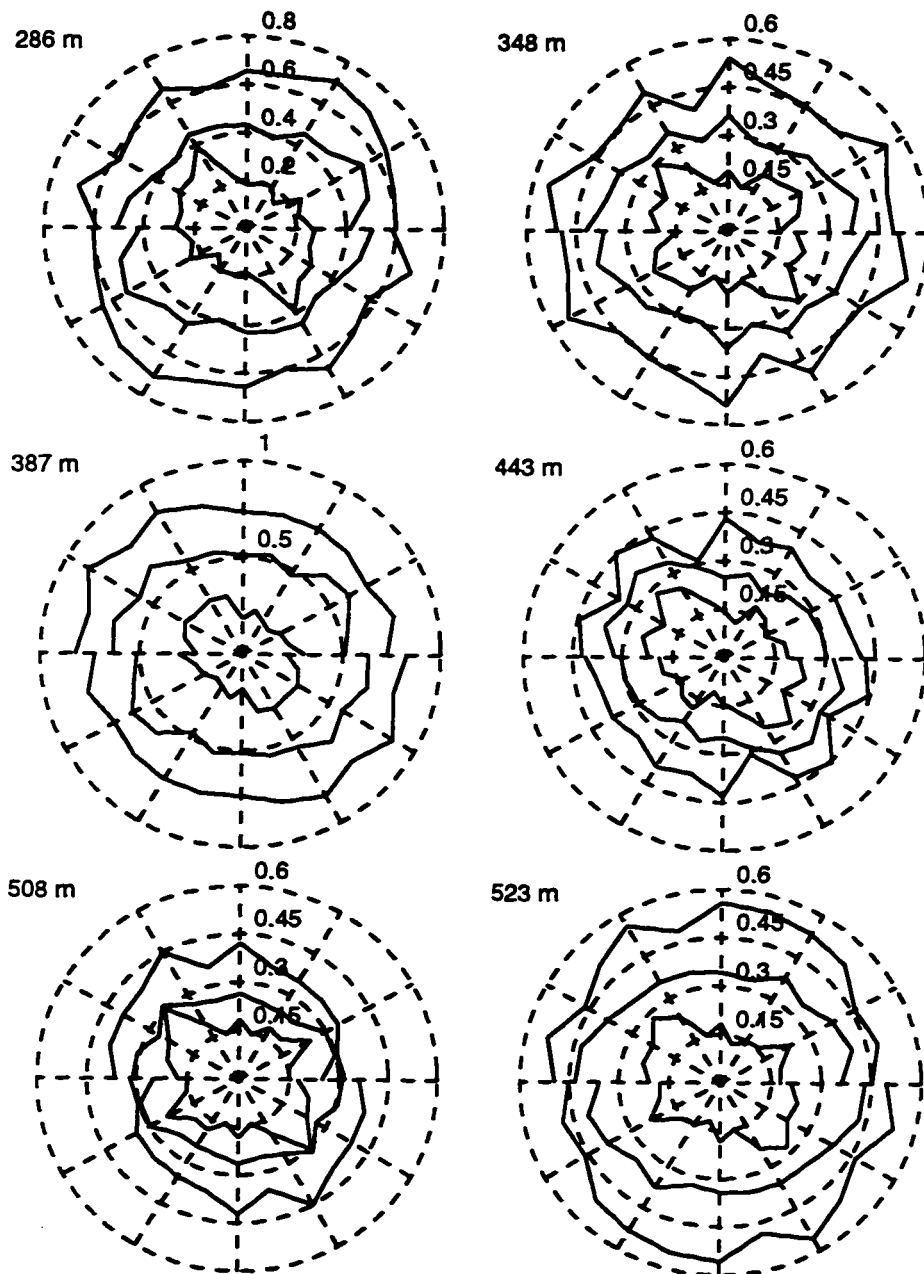


Figure 8.5: Polar diagrams of received amplitude (in mV) for selected internal layers. The data are reflected across the horizontal axis which corresponds to flowline-parallel receiver polarization. Curves for three constant depolarization angles are shown: the outermost curves are means of transmitter angles within 15° of the receiver angle, the innermost curves are means of transmitter angles within 15° of cross-polarization, the intermediate curve is for $45 \pm 15^\circ$ depolarizations.

large (>10%) strain. The rheology of highly oriented fabric is anisotropic by about a factor of 10. The flow field which leads to the fabric development is thus influenced by the fabric. The polarization experiment suggests that either the layers are not caused by fabric variations, or that the fabric must be axially symmetric about the vertical. The sonic velocity log does suggest that oriented fabrics are present. If fabric layering is present, it is still possible that the layers are isochrons since recrystallization rates are affected by impurity content Alley (1992), and so the layer development may in fact be stratified by depositional processes.

8.2 *Divide stability*

The modern accumulation rate at Taylor Dome shows a high degree of spatial variability (section 5.2.2). In the following chapter I assume that the radar internal layers are isochrons in order to use the depths of shallow layers to interpolate the modern spatial pattern between the measurements points. I then use this accumulation rate pattern in a flow-line parallel ice dynamics model to predict an isochron pattern. By comparing intermediate-depth radar layers with the calculated isochrons I show that a temporal variation of the spatial accumulation rate pattern has occurred. The numerical model calculates the velocity field which is in steady state with the applied accumulation rate and the modern ice sheet profile. Of particular concern is whether any significant shift in the flow divide position has occurred over the period of inference. The pattern of radar internal layers themselves can be used to justify both the isochron and steady-state flow field assumptions.

Much as standing waves form on the surface of a stream which flows over a rough bed, ice flow over the rough bed topography at Taylor Dome results in undulations at the surface (Jóhannesson, 1992). Interaction of surface winds with this topography results in localized accumulation rate variations (Whillans, 1976). For artificial surface features, such as buildings and fences, these take the form of familiar snow drifts.

(Weertman, 1993) showed that depths of shallow radar internal layers are correlated with local spatial accumulation rate variations. Examination of radar profiles show that even the most subtle surface features can cause accumulation rate variations. Temporally stable spatial patterns leave a record of their presence which can be detected with radar. Locally high (low) accumulation rates cause deep (shallow) layers near the surface. These layer anomalies become thick (thin) inter-layer spacing as they are buried.

The flow-line parallel radar profile shown in figure 2.5, which is the basis for the modeling in the following chapter, displays a wealth of such layer patterns. The depths of radar internal layers were picked using a manually-guided automatic picking algorithm. A series of cubic spline intervals were formed which visually approximate each radar layer. The spline knots are positioned by the amplitude maxima/minima within a small search radius of a manually identified location. Picked in this way, figure 8.6 shows the internal layers from the flow-line parallel profile. The flow divide in this north-south profile is at 19 km. Locations with relatively high accumulation rate occur at 15, 17.5, 22, and 26 km, these are indicated by the locally down-warped shallow internal layers. An accumulation low at 13.5 km is indicated by the locally up-warped layers.

Differencing adjacent layers reveals a sequence of inter-layer space maxima/minima, the positions of which are indicated in the figure by open circles. These maxima/minima can be traced to increasing distance from the divide with successively greater depths. The flow model presented in the following chapter was used to predict the particle trajectories labeled "a" through "e" in the figure. The agreement of these trajectories with traces of the buried accumulation rate maxima/minima is striking. Trajectories "a", "b", and "d" over lie their corresponding accumulation rate anomaly traces. The maxima-trace which originates near 17.5 km appears to jump from one trajectory to another which originates 300 meters further from the divide. The agreement of the southern-most trace with particle trajectory "e" is not

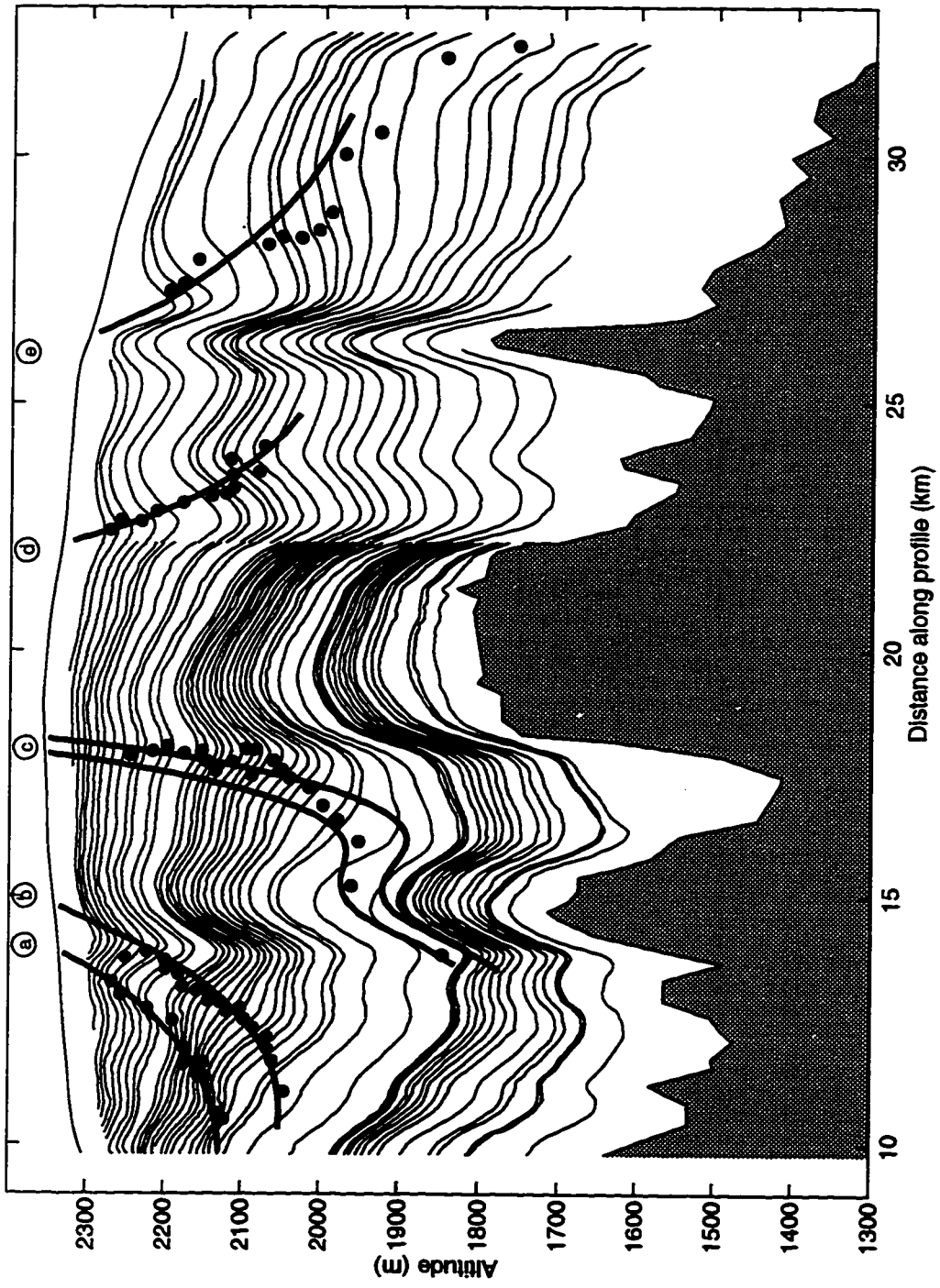


Figure 8.6: Internal layers from flow-line parallel radar profile (figure 2.5). Dots show locations of inter-layer space minima/maxima caused by accumulation rate variations. Bold lines are calculated particle trajectories.

as satisfying as the others, but is still reasonable. Overall, the coincidence of the accumulation rate anomaly burial traces with the calculated particle trajectories argues that the flow-field has been at or near steady state for the period including the age of the deepest anomaly traces. By comparing with figure 10.1, this interval extends at least to the early Holocene, and the "c" trajectory suggests the period extends to about 30 kabp. That its maxima-trace "jumps" trajectories may be an indication of a small divide location shift, limited to roughly the 300 meter displacement of trajectories origin.

Chapter 9

2-D PLANE STRAIN FLOW LINE MODELING

Ice flow calculations are the primary tool for glaciological contributions to ice-core paleoclimate programs. Prior to drilling, predicted depth-age relationships allow identification of sites with optimal maximum age, or optimal temporal resolution in a particular age range. The accuracy of such predictions is limited by poor knowledge of the flow field and accumulation rate history. Once the various core properties are sampled, and with the support of detailed geophysical measurements made in the vicinity of the coring operation, ice flow modeling becomes an important tool for interpretation of the ice core record. Notable examples from the GISP2 program include the work of Cuffey *et al.* (1995), who used borehole temperature measurements to calibrate the stable isotope “thermometer” and infer the magnitude of surface temperature change which occurred with the Wisconsin–Holocene transition, and Cutler *et al.* (1995) who used the physical spacing of annual layers to infer paleo-accumulation rates. In this chapter I focus on the paleoaccumulation rate record at Taylor Dome. In particular, ice flow modeling and timescales obtained by stratigraphic correlation with other dated records are combined to infer paleo-accumulation rates. These are compared with the ice core ^{10}Be concentration profile, which is believed to be a proxy for accumulation rate Steig (1996).

9.1 Model setup

The ice core site is a few ice thicknesses south of the flow divide. Due to horizontal ice flow, deeper ice in the core originated at greater distances from the core site.

Since the cross-flow divergence along the flow-line between the flow divide and the core site is small, the flow is approximately two-dimensional. In chapter 6 I used the two-dimensional, plane strain, flow model developed by Raymond (1983) to generate “synthetic” ice divide profiles. The same model was used by Waddington *et al.* (1993) to predict ice-core time-scales at Taylor Dome prior to drilling the core. The modeling presented here used the same code, but is improved over the earlier work by using better surface and bed topography profiles, measured accumulations rates, and finer grid resolution.

Surface and bed topography measured along the flow-parallel radar profile shown in figure 2.5 define the boundaries for the modeling in this chapter. The profile is discretized by the grid shown in figure 9.1. The nodes are oriented column-wise, with 15 nodes per column. The vertical node density increases with depth to accommodate enhanced strain rates near the bed. Horizontally, 73 nodes are used with inter-node spacing ranging from 250 to 750 meters. The mesh was chosen as a compromise: the nodes should be closely spaced to represent the steep topography and resulting flow gradients, yet too many nodes are computationally burdensome. The bed profile was smoothed after sampling to remove node-to-node roughness. The surface topographic crest at km 19 is taken to be the position of the flow divide, consistent with stake motion measurements. The section extends more than 15 kilometers in each direction from the divide to reduce the effects that the boundary might exert at the core site.

The model uses a Glen-type, isotropic, non-linear flow law of the form

$$\dot{\epsilon}_{ij} = EA\tau^{n-1}\tau_{ij}$$

The constant, n , is chosen to be 3. The softness parameter, A , has an Arrhenius temperature dependence with an activation energy of 60 kJ/mol. Values of A are given by Paterson (1994). The measured bore hole temperature, presented in chapter 5, varies nearly linearly with depth. I apply the observed temperature profile at the core site, elsewhere it is truncated at, or extrapolated to the bed. This simple

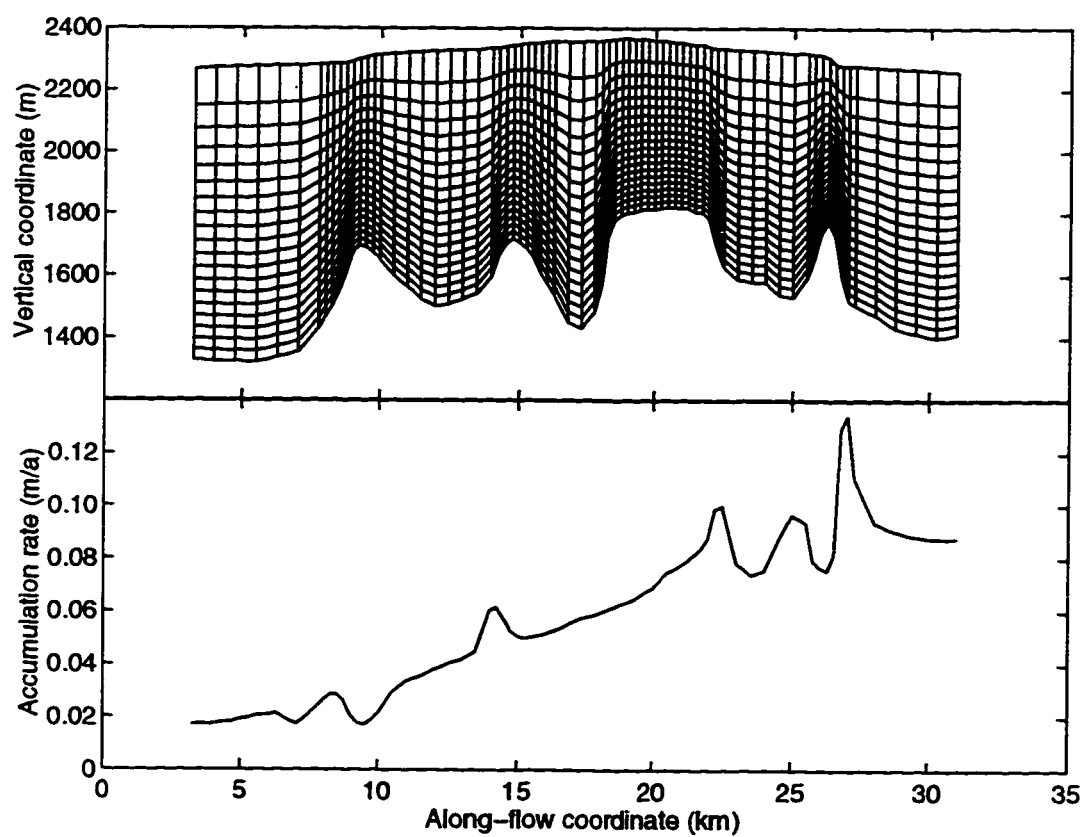


Figure 9.1: Finite element mesh (top) and applied accumulation rate function(bottom).

assumption is within 2° C of the 3-D finite difference temperature modeling results discussed in section 7.1.

A combination of velocity and stress boundary conditions are applied. The bed is frozen, so its velocity fixed at zero. The upper surface has zero traction. The horizontal component of velocity is specified on the vertical boundaries. Its shape is given by the fourth power of height above the bed. The outward flux along the sides is in balance with the applied accumulation rate. Shown in figure 9.1, the accumulation rate spatial pattern is formed by the depth of a continuous, shallow radar internal reflecting horizon normalized to its depth at the core site and scaled by the measured current accumulation rate at the core site. This accumulation function agrees with rates measured by marker burial and β -activity cores (section 5.2.2). The model calculates the internal velocity field consistent with the boundary conditions. The upper, free surface is allowed to evolve until the vertical velocity along the boundary is locally balanced by the accumulation rate.

A model “run” involved allowing the surface elevation profile to evolve to steady state with the applied accumulation rate. The primary model “tuning” parameter was the flow law rate enhancement parameter, E . For a given accumulation rate, softer ice implies lower surface slopes since lower stress is required to drive the required flow. The goal was to have the final surface geometry match the measured profile. In essence, finding the softness parameter which best matches the model geometry to the measured topography is an inversion for the “effective” flow law softness parameters. The mesh shown in figure 9.1 is a steady state topography achieved after 3000 models “years” of iteration. The surface topography in the region overlying the central sub-glacial plateau, which includes the ice divide and core site, is in good agreement with measured profile. For an assumed core-site accumulation rate of 8 cm/yr, the value of A needed to achieve this fit is nearly a factor of five softer than that recommended by Paterson (1994). This high value is accepted in light of surface velocity data which, as shown in chapter 7, suggest a factor of 3 is appropriate, and accumulation rate

measurements which suggest the assumed 8 cm/yr accumulation rate is too high. Also, the model run did not use the additional softening affected by the *generalized* form of the flow law as discussed in chapter 6. The goal in this case is not to find “the” flow law rate factor, but to find the strain rate field in the vicinity of the flow divide and ice core site. The stress regime, and hence the particle trajectories scale with the ice thickness and surface slope. Since the model topography in the vicinity of the divide is in good agreement with the measured profile, the strain rate pattern in this region is taken to be a good representation of the flow field leading to the ice core site.

The particle trajectories and thinning function presented in the remainder of this chapter were derived from this solution. Since the surface fit was biased toward matching the topography in the divide region, it is expected that the solution is a less reliable indicator of actual flow conditions away from the divide. In particular, the ice flows over a sharp bedrock pinnacle near km 27. The model predicts a much more pronounced surface undulation over this feature than is observed. This is likely the result of several factors which include the large discretization elements, the inaccurate temperature estimate, and three-dimensional flow effects.

9.2 Model results and ice core interpretation

Strain histories may be calculated using the velocity solution of the finite element model. In the previous chapter I argue that the position of the divide has been stable at least since the beginning of the Holocene. If the geometry of the flow has been constant through time, then ice recovered in the core traveled along the paths shown in figure 9.2. The *thinning function*, Λ , is a convenient tool for predicting layer thicknesses and time scales. It is obtained by integrating the total vertical strain along these paths between the surface and the core. The time scale is given by

$$\text{Age}(z) = \int_0^z \frac{1}{\lambda(z)} dz \quad (9.1)$$

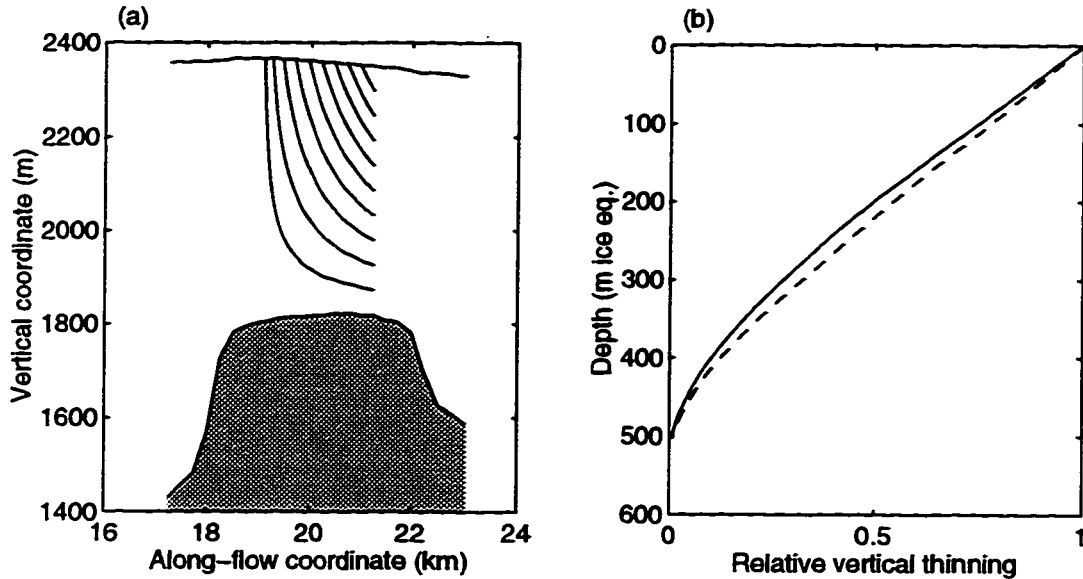


Figure 9.2: Particle trajectories intersecting ice core at 50 meter depth intervals (a), and ice core vertical thinning functions (b). The solid line is the *enhanced* thinning function Λ_e discussed in the text.

where $\lambda(z)$ is the annual layer thickness profile. With constant accumulation rate, the annual layer thickness is simply the product of thinning function, Λ , and the accumulation rate, \dot{b} . If the accumulation rate varies through time, but in such a way that the geometry is unaffected, then the annual layer thicknesses are given by $\lambda(z) = \Lambda \dot{b}(z) / \dot{b}(0)$ where $\dot{b}(z)$ is the accumulation rate at the time of deposition.

The modern spatial pattern of accumulation shown in figure 9.1 indicates the accumulation rate at the core site is approximately 20% higher than at the divide. This pattern is probably controlled by the surface topography as this is the up-slope side of the dome for moisture-bearing storm trajectories. If the geometry of the surface is temporally constant, this pattern should also be constant. The southward dip of internal layers suggests that this is the case. For later analyses, the effect of this spatial variation is removed from inferred temporal variations by using the *enhanced* thinning function, Λ_e , shown in figure 9.2. This function is obtained by scaling the

thinning function computed above by the ratio of the accumulation rates at the core site and the source region.

The thinning profile is controlled predominantly by the geometry of the flow. Thus I assume that Λ_e is independent of the rate of flow. If the geometry in fact changes, such as by overall ice sheet thickening, then the thinning function and hence paleo-accumulation inferences made from it will be in error. The layer thickness profile (or alternatively the time scale) and the accumulation rate history are linked by the thinning function. Complete knowledge of two of these exactly specifies the third. Steig (1996) used the concentration of ^{10}Be to infer paleo-accumulation rates and layer thickness profiles. Timescale estimates can be obtained by stratigraphic correlation with other ice cores. Together with the thinning function, these estimates over-specify the problem, yet they are each, no doubt, not without errors. In the following sections, I examine the consistency between these data.

9.3 Layer thinning profile

The accumulation regime at Taylor Dome is such that annual signals are at best poorly preserved. Firn cores show that seasonal variations of $\delta^{18}\text{O}$ become indistinguishable a few tens of meters below the surface (Grootes, pers. comm.). Unfortunately, time-scale based on annual counting, such as was spectacularly successful with much of the GISP2 ice core cores (Meese *et al.*, 1994), is not possible at Taylor Dome. However a counting timescale may be attainable by relying on natural variability with a longer timescale. The well known Schwabe solar variability causes polar stratospheric ^{10}Be concentration to vary with an approximately 11-year periodicity. Steig *et al.* (1996) showed that periodic ^{10}Be concentration variations in the Taylor Dome firn are synchronous with the solar cycle. In the main ice core, high resolution ^{10}Be concentration measurements were performed in four sections at depths down to 300 meters (Steig *et al.*, 1997). Regular variations in ^{10}Be concentration were present

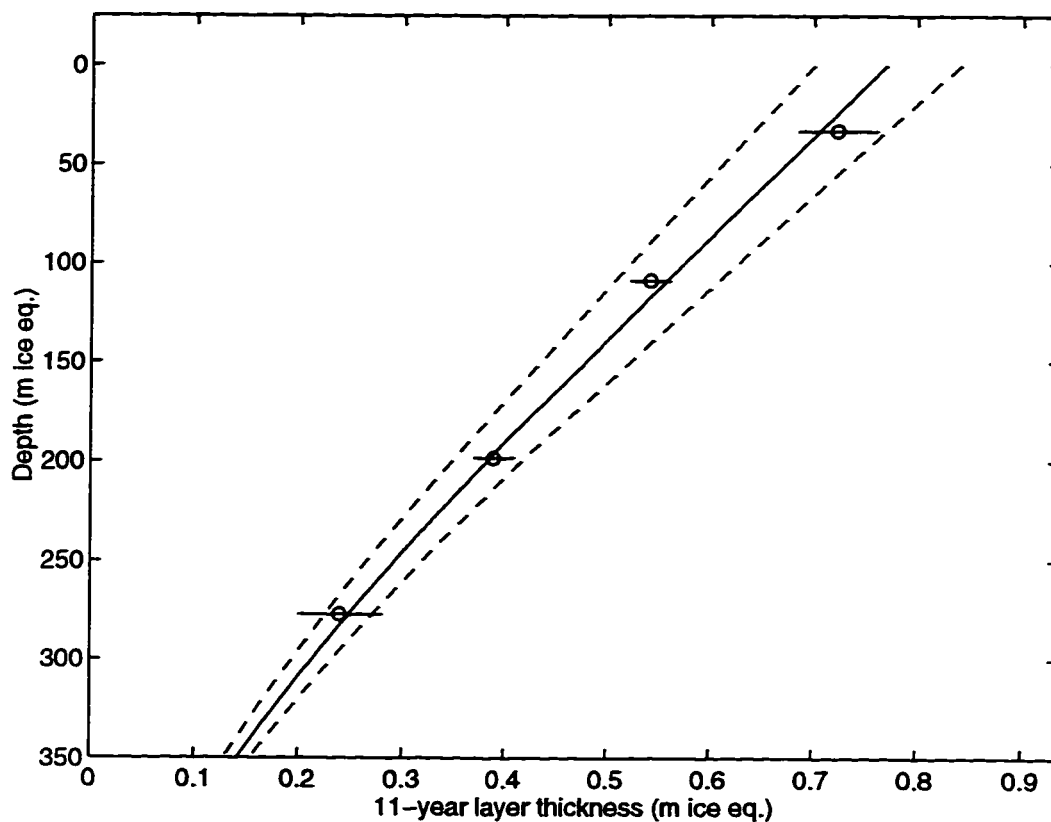


Figure 9.3: Eleven-year thickness predicted by flow model (solid curve) compared with ^{10}Be variation wavelengths (circles) in ice equivalent units.

in each of these sections; their wavelengths are shown in figure 9.3. In the figure, error bars are given primarily by the sample thickness. Assuming a constant 7 cm/a accumulation rate, the thinning function, Λ_e , presented above predicts the 11-year layer thickness profile also shown in figure 9.3. The curve is bracketed by 10 and 12 year layer thickness profiles, allowing for the \pm one year uncertainty commonly assumed for the period of the Schwabe solar cycle. Alternatively these bounds could be considered $\sim 10\%$ accumulation rate uncertainties. These data provide a direct test of the thinning function over the upper ~ 300 meters, the agreement of these curves argues that: (1) the cyclicity of ^{10}Be concentrations measured in the Taylor

Dome core are due to Schwabe-linked production rate variations, and (2) that the assumption of constant accumulation for the four samples, the shape of the thinning function, and the assumed stability of the Schwabe period are either mutually correct, or they are deviously in error such that their effects cancel to give the impression that they are.

9.4 Depth-age profile

Given an accumulation rate history, flow modeling can be used to predict the ice core time scale. These time scales can be greatly improved through identification of stratigraphic markers, such as dated volcanic events or climatic variations. With an independently determined time scale, paleo-accumulation rates Cutler *et al.* (1995); Cuffey *et al.* (1995), or ice flow variations can be determined.

Grootes (*pers. comm.*, 1995) formed a preliminary time scale estimate for the Taylor Dome core by correlation with the Vostok ice core. To illustrate this technique, the Vostok δD and Taylor Dome $\delta^{18}O$ profiles are shown on the EGT time scale (Jouzel *et al.*, 1993) in figure 9.4. The preliminary Taylor Dome time scale, referred to as "STD_TIME_7_95" is formed by assuming that climatic variations are recorded simultaneously at Vostok and at Taylor Dome. By visually comparing the profiles, the midpoints of matching distinct transitions are used as control points for interpolation. This technique is clearly subjective, and some of the matches are more convincing than others. But with care, and a little bit of luck, a reliable time scale can be obtained. By similar means, Bender and Brook (*pers. comm.*, 1997) correlated variations of atmospheric $\delta^{18}O$ and methane with the GISP2 core. Additional age control points come from two well defined ^{10}Be concentration spikes, which are thought to be anomalously high production rate events (Steig, 1996; McHargue *et al.*, 1995). These peaks appear in both the Vostok and GISP2 ice cores, one at 34.7 ka on the GISP2 timescale (Meese *et al.*, 1994), and the other at 64 ka on the EGT

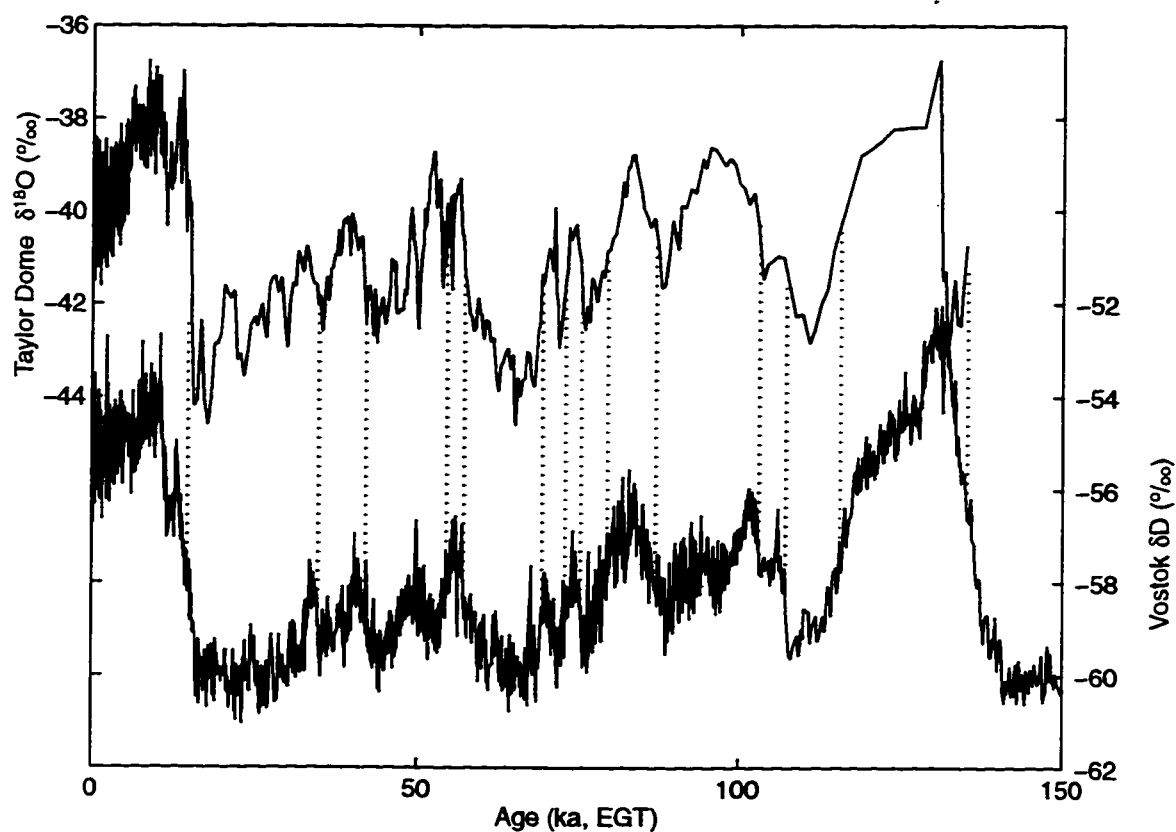


Figure 9.4: The lower curve is the Vostok δD profile on the EGT (Jouzel *et al.*, 1993) timescale, the upper curve is the Taylor Dome $\delta^{18}O$ profile. The timescale of the $\delta^{18}O$ record is a linear interpolation between the age control points shown as dotted lines.

timescale (Jouzel *et al.*, 1993).

These age determinations are collected in figure 9.5. The figure shows that there is some scatter to the predictions, but overall the agreement is remarkable. Significant features are the break in slope at ~ 13 ka, underlain by an ~ 20 m section showing a very steep age gradient. These ages are compared with a time scale calculated using Λ_e and a constant accumulation rate of 6 cm/a. The ratio of slopes for the predicted curve and the correlation time scale at a given depth gives the ratio of the assumed accumulation rate to that at deposition. The steep age gradient section between ~ 350 and 370 meters suggests very low accumulation rates in that interval.

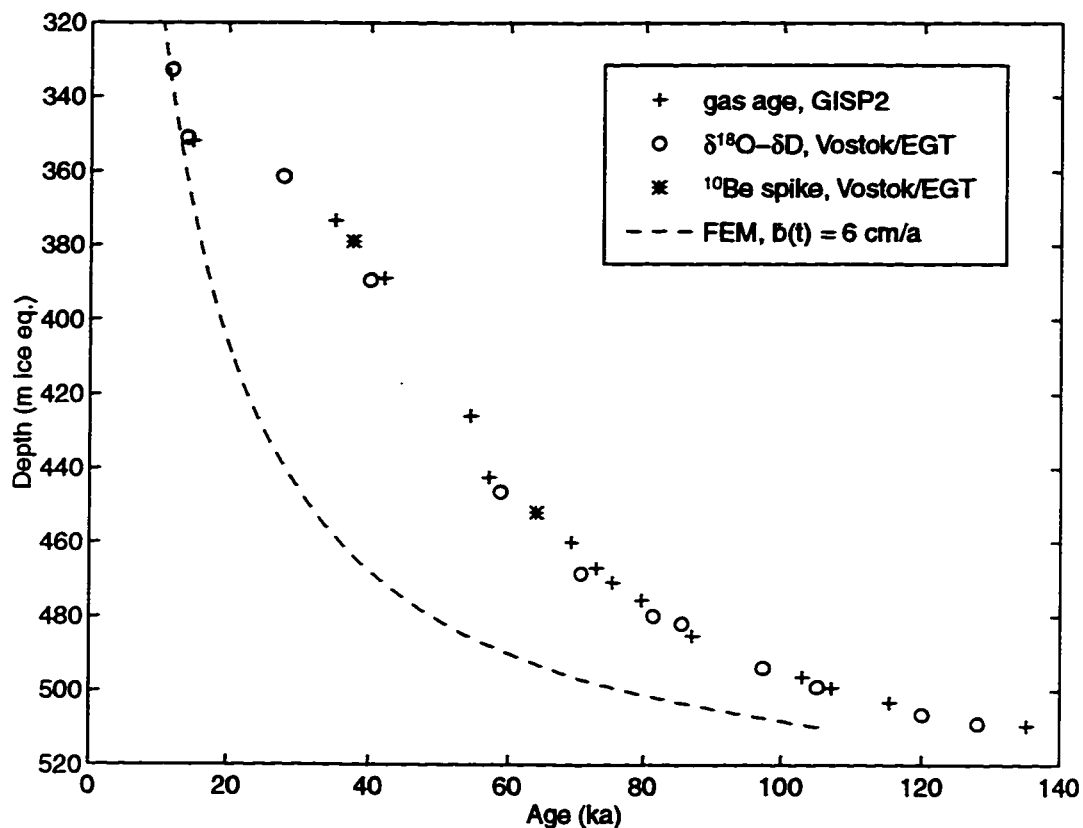


Figure 9.5: Taylor Dome ice core age determinations from stratigraphic correlation.

9.4.1 Determination of paleo-accumulation rates consistent with time scale and thinning function

The accumulation rate which produces an age-depth profile consistent with the correlation time scale can be found using the thinning function, Λ_e . The direct solution involves differentiating the measured time scale. This approach produces a rough accumulation rate profile since it amplifies age determination errors. Instead, an accumulation rate profile is sought that minimizes the discrepancy between the correlation time scale and the time scale it predicts. Unfortunately there are no correlation age determinations in the upper half of the ice column. This difficulty is overcome by requiring the solution to predict layer thicknesses consistent with the solar-cycle layer

thickness presented in the previous section. The accumulation rate function is formed as a sequence of C_0 continuous straight line segments. The segment knots are placed according to the data density. Four knots span the range constrained by the layer thickness data. Below 300 meters, 15 knots are constrained by 28 age determinations. A Levenberg-Marquardt algorithm is used to iteratively determine the accumulation rate profile which minimizes the performance parameter R .

$$\begin{aligned}
 R = & \alpha \sum_i \left(\frac{\text{Age}_i^{\text{obs}} - \text{Age}_i^{\text{calc}}}{\sigma(\text{Age}_i^{\text{obs}})} \right)^2 \dots \\
 & + \beta \sum_j \left(\frac{\lambda_j^{\text{obs}} - \lambda_j^{\text{calc}}}{\sigma(\lambda_j^{\text{obs}})} \right)^2 \dots \\
 & + \gamma \sum_k \left(\frac{\Delta^2}{\Delta z_k^2} \dot{b}_k \right)^2 \quad (9.2)
 \end{aligned}$$

Age discrepancies are determined by interpolating the model predictions to the depths of the i age determinations, and layer thickness discrepancies by interpolation to the j layer thickness determinations. Age discrepancies are weighted by their estimated precision, $\sigma(\text{Age}_{\text{obs}}(z_i))$, taken to be 5% of the determined age. Layer thickness discrepancies are similarly weighted; their precisions are shown in figure 9.3. The third term in (9.2) is the second derivative of the accumulation profile in the k knots. This is a smoothness condition used to damp solution oscillations which result from exact satisfaction of the age data. The non-negative factors, α, β, γ , weight the relative importance of the age, layer thickness, and smoothness conditions. The relative values of α and β primarily affect details of the solution in the 300–330 meter depth range, The relative size of γ to α and β controls the tradeoff between smoothness and goodness of fit to the observed values ages/layer thicknesses.

The accumulation rate function obtained by this minimization procedure is shown in figure 9.6. As indicated by the error bars, the robust features of the inferred accumulation rate profile are the nearly constant Holocene values, the low values in the LGM period, and the steady decrease leading into the LGM. The error estimates

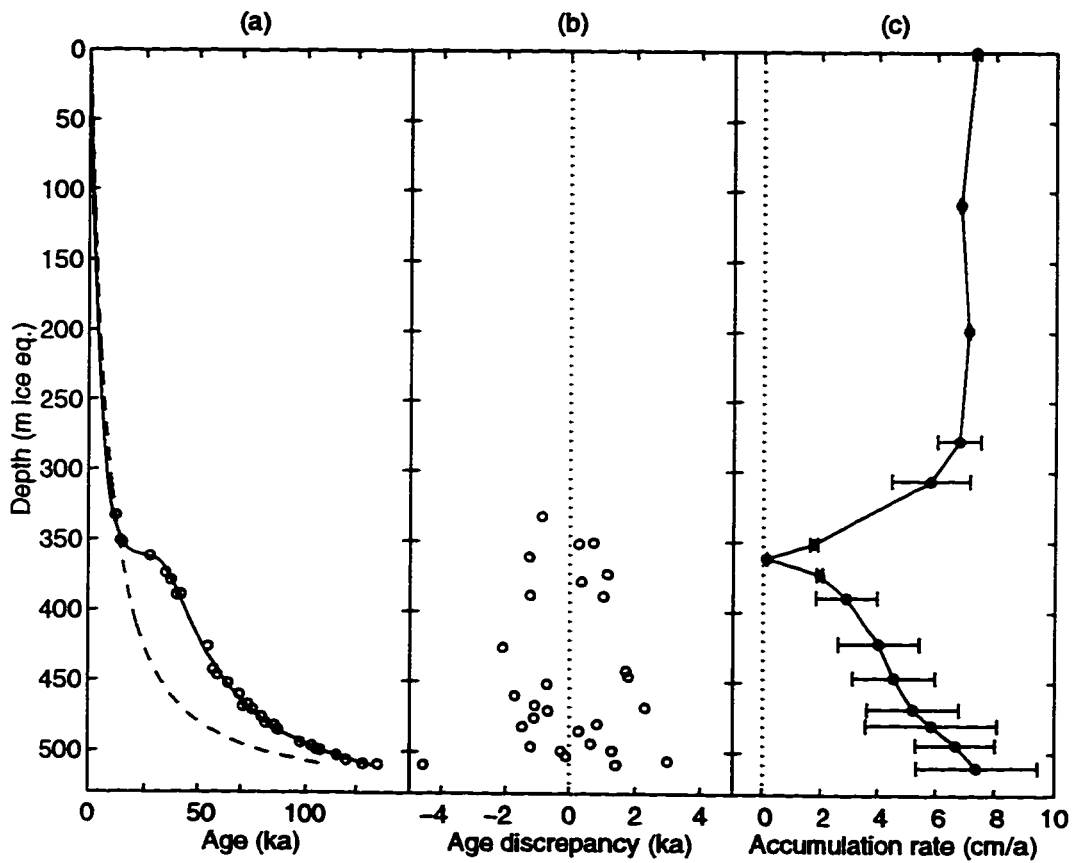


Figure 9.6: Preferred accumulation rate profile inferred from timescale. (a) Ice core age control points (circles) and timescale calculated by assuming constant accumulation rate (dashed). The solid curve in (a) is the timescale corresponding to the inferred accumulation rate profile shown in panel (c). Panel (b) is the discrepancy between this timescale and control points

are calculated by first linearizing the age and layer thickness discrepancy calculation about the solution values. Then standard error propagation analysis is used to determine the effect of age and layer thickness determination on the inferred accumulation rate (see for example, Menke, 1989, pp. 65). Accumulation rates for depths in the core less than ~ 250 meters are exactly specified by the layer thickness data. The large error bars near 300 meters occur at the suture of the layer thickness and age control data. The position of the minimum at 360 meters, corresponding to an age of 27.6 ka, is pinned by the single corresponding gas age control point. The timing of, and accumulation rate slope at the Holocene transition are not resolvable with the existing age and layer thickness data.

Comparison with geochemical accumulation rate records

Given the FEM derived thinning function, the accumulation rate profile shown in figure 9.6 are the rates required to produce a time scale consistent with the ages determined from the stratigraphy. This profile is compared with the accumulation rate profile predicted by geochemical means. The flux of cosmogenic ^{10}Be to the surface is assumed constant on time scales longer than the solar wind periodicity (11 yr), and shorter than for geomagnetic intensity variations ($\sim 10^5$ yr). Steig (1996) showed that the deposition of ^{10}Be at the Taylor Dome is primarily by dry deposition, therefore its concentration in the firn gives snow accumulation rate because ^{10}Be is diluted by higher snow accumulation rate. To infer paleo-accumulation rates from ^{10}Be concentration, he used an expression of the form

$$\frac{\dot{b}(t)}{\dot{b}(0)} = \frac{[^{10}\text{Be}(0)] - W}{[^{10}\text{Be}(t)] - W} \quad (9.3)$$

in which $[^{10}\text{Be}(0)]$ is the modern concentration, and W is a wet flux correction. Steig recommended values of $.065 \pm .01$ m/a and 5000 ± 2000 mol $^{-1}$ for $\dot{b}(0)$ and W , respectively. The two values for these which minimize the least-squared discrepancy between (9.3) and the inferred accumulation rate profile (figure 9.6) are 0.053 m/a

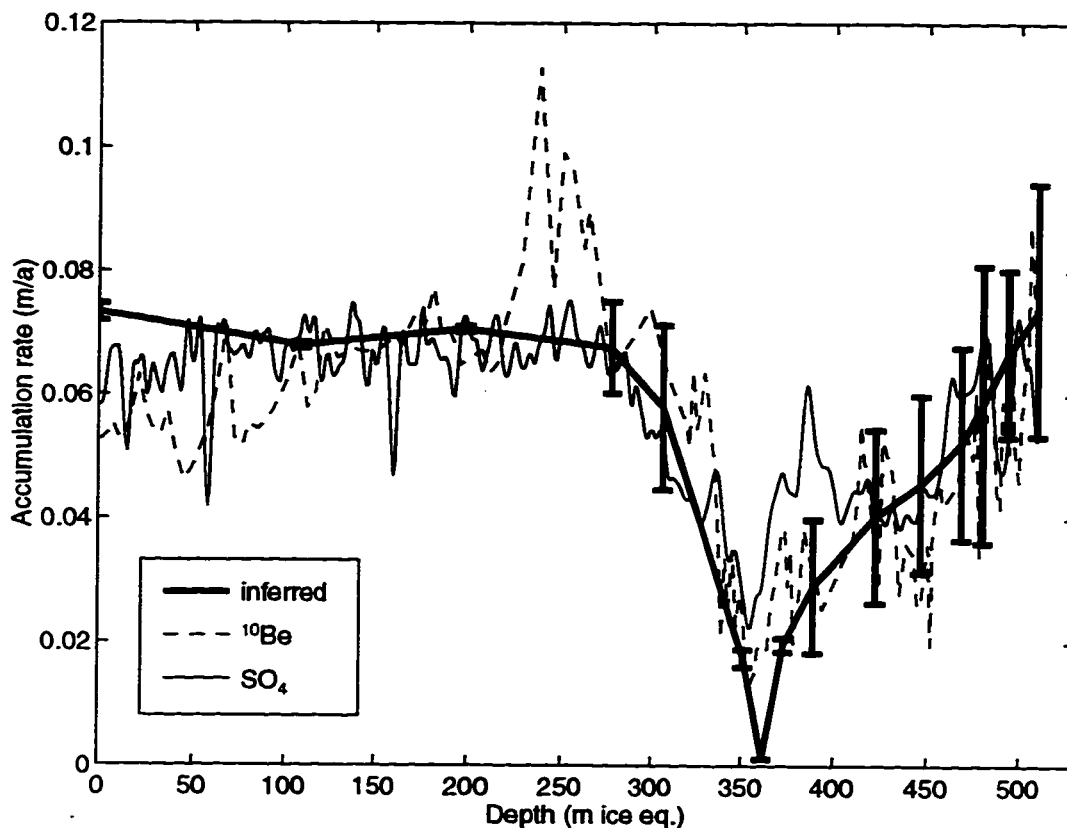


Figure 9.7: Preferred accumulation rate profile compared with accumulation rates inferred from ^{10}Be and SO_4^{2-} concentrations.

and 0 mol/g, respectively. Using these, the Taylor Dome ^{10}Be concentration profile predicts the accumulation rates shown in figure 9.7. Steig's values predict an accumulation rate profile which agrees with the solar-cycle layer thickness profile, but which is not consistent with matching the time scale. The difficulty comes from the high accumulation rates predicted by the low ^{10}Be concentrations in the early Holocene, and that the wet flux correction term increases this discrepancy. An unconstrained minimization produces non-physical, negative values for W .

It is generally assumed that Beryllium atoms are attached to sulfate aerosols (McHargue and Damon, 1991). In polar conditions, sulfate is often assumed to be

deposited by dry flux (and, by association, so too is ^{10}Be), thus its concentration should also give snow accumulation rate. A SO_4^{2-} -derived accumulation rate profile is compared with the inferred and the ^{10}Be -accumulation rates in figure 9.7. This curve is predicted using (9.3) but with ^{10}Be concentration replaced with that of SO_4^{2-} . The free parameters $\dot{b}(0)$ and W are again found by minimizing the misfit between the curve and the inferred accumulation rate; the values are 0.058 m/a and 0.0005 mol/g, respectively.

Overall, the agreement of the three curves shown in figure 9.7 is very good, but significant differences exist. Within the resolution of the model, the curves are similar below about 400 meters; the greatest disagreement between the curves lies above. Two prominent lows in the SO_4^{2-} -derived profile, at ~ 60 and at ~ 170 meters. These are due to SO_4^{2-} concentration spikes which are probably caused by volcanic events, and may be disregarded for this comparison. The SO_4^{2-} -derived profile does not support the high early Holocene accumulation rates suggested by the ^{10}Be -derived profile. From these data, I conclude that the ^{10}Be production rate was reduced during that period. This is counter to the constant-flux assumption which underlies expression (9.3). The ^{10}Be and SO_4^{2-} -derived profiles agree very well elsewhere, but they differ from the inferred profile. Both the ^{10}Be and SO_4^{2-} -derived profiles show decreasing values in approximately the upper 100 meters. This is inconsistent with the uppermost solar-cycle layer thickness which support a slightly higher recent accumulation rate. Over the 350–370 meter depth interval, the very low accumulation rates required by the age control estimates are not supported by either of the geochemically determined profiles.

9.4.2 Determination of thinning function consistent with time scale and geochemically-determined accumulation rates.

The agreement of the inferred accumulation rate profile with the profiles predicted by ^{10}Be and SO_4^{2-} is encouraging. It is tempting to accept the $\dot{b}(0)$ and W values used

above as calibrations for the ^{10}Be and SO_4^{2-} -derived snow accumulation rates. However first the validity of the thinning function must be questioned. I begin by posing the minimization procedure presented in the previous section in the opposite way: what is the thinning function that is consistent with the geochemically-determined accumulation rates and the ages determined from the stratigraphy? The same technique is applied using the same performance parameter (9.2), but in this case, the accumulation rate is given by the ^{10}Be or SO_4^{2-} concentrations using expression (9.3) by allowing the modern accumulation rate, $\dot{b}(0)$, to be a free parameter. The wet flux correction is not used. The form of the desired thinning function is again a series of C_0 piecewise linear segments. Additional constraints are that the surface value of the thinning function is fixed at unity and that it is non-negative elsewhere. The ^{10}Be and SO_4^{2-} concentrations are used separately to determine the “effective” thinning functions shown in figure 9.8. These fits predicted modern accumulation rates of 0.074 and 0.075 m/a for the ^{10}Be and SO_4^{2-} concentration derived profiles, respectively. The solutions are similar, reflecting the overall similarity of the species concentrations. These functions differ from the modeled profile above ~ 300 meters since the concentrations of both species predict decreasing Holocene accumulation rates. The difference between the curves is greatest near 300 meters, where their concentration-inferred accumulation rates differed most. The notable feature of both of these inferred thinning functions are the near zero values at 360 meters, below which they increase with depth. The “effective” thinning functions require that the ice has undergone decreasing total vertical strain with increasing depth, *i.e.* they have undergone thickening. Such a thinning function seems unlikely given “reasonable” assumptions regarding the flow history and ice rheology, especially since the radar layer data (section 8.2) support near steady-state Holocene divide geometry.

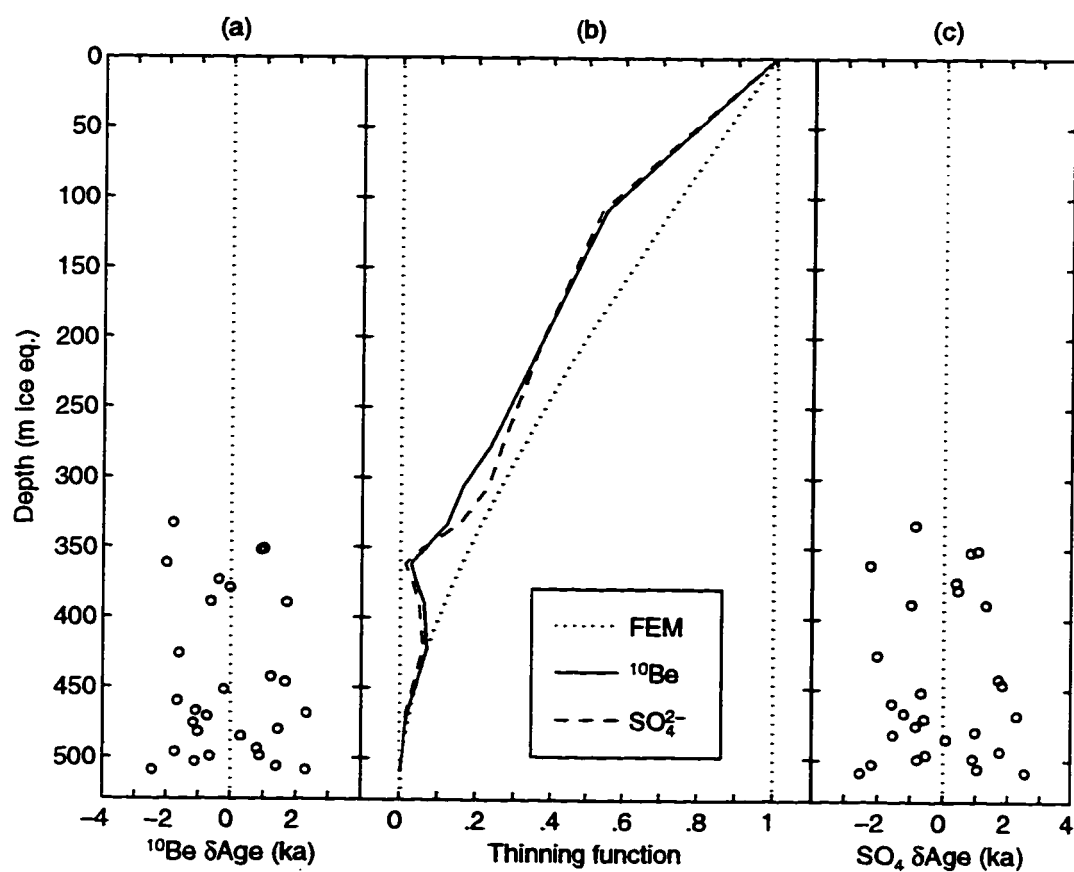


Figure 9.8: (b) Thinning functions implied by ^{10}Be and SO_4^{2-} -derived accumulation rate profiles (center panel). Dotted curve is thinning function calculated from finite element model. Panels (a) and (c) show age discrepancies for the thinning function required by ^{10}Be and SO_4^{2-} -derived accumulation rates.

9.4.3 Thinning function for non-steady state ice thickness

A thinning function that strain that increases with depth, such as in figure 9.8, is unexpected. However, the thinning function, Λ_e is calculated assuming that the divide geometry is in steady state, and with the large accumulation rate variations suggested by the ^{10}Be concentrations, steady state geometry does seem unlikely. Non-steady flow could contribute to the shape of the thinning profile, but by how much? In this section I test the sensitivity of the thinning function to ice sheet thickness variations.

For the test, I need to construct a simple but physically based model which describes ice sheet thickness response to mass balance variations. Consider a simple forward calculation:

$$\frac{dH}{dt} = \dot{b}(t) - v(t)$$

The surface vertical velocity $v(t)$ is a function of ice rheology and ice sheet geometry. If the accumulation rate exceeds $v(t)$ then the ice sheet thickens. For similar analysis regarding the Greenland ice sheet, Cutler *et al.* (1995) assumed that the surface maintains a steady-state profile given by Vialov (1958): $H \propto v^{1/2n+2}$. In this expression, the constant of proportionality is determined by modern values. I will apply a similar approach.

I apply a synthetic accumulation rate history to drive ice thickness evolution. The history, shown in figure 9.9a, contains both an accumulation rate low similar to what is suggested for the LGM, and a shorter doubling of accumulation rate. The evolution of ice thickness is solved numerically for ice thickness at the next time step, H_{n+1} , using values at the current times step n using the “improved Euler” method summarized by

$$\begin{aligned} \frac{dy}{dt} &= \mathcal{F}(x, y) \\ \hat{y}_{n+1} &= y_n + \Delta t \mathcal{F}(x_n, y_n) \\ y_{n+1} &= y_n + \frac{\Delta t}{2} (\mathcal{F}(x_n, y_n) + \mathcal{F}(x_{n+1}, \hat{y}_{n+1})) \end{aligned} \tag{9.4}$$

The \hat{y}_{n+1} term is an estimate of the value of y at the new time step. The ice thickness history solved by this procedure, shown in figure 9.9b, is intended to give plausible upper bounds on ice sheet response to accumulation rate variations. It is important to note that I have not included temperature forcing variations which would tend to reduce the amplitude of ice sheet thickness variations if temperature and accumulation rate covary.

The ice thickness history is then used to calculate thinning functions for one dimensional, time varying flow fields. Three different analytic expressions for vertical velocity profile are compared. For the Camp Century ice core, Dansgaard and Johnsen (1969) used a flow model which has a vertical strain rate that is constant down to a height h above the bed, and then decreases linearly to zero at the bed. The vertical profile calculated by the FEM for modern conditions at Taylor Dome is well approximated by a Dansgaard-Johnsen profile with a value of h equal to 185 meters. The Dansgaard-Johnsen profile is adapted for time-varying ice thickness by

$$\begin{aligned}
 h(t) &= h_0 \frac{H(t)}{H_0} \\
 w(z, t) &= -\dot{b}(t) h(t) \frac{z - h(t)/2}{H(t) - h(t)/2} & H(t) \geq z \geq h(t) \\
 w(z, t) &= -\dot{b}(t) h(t) z^2 & h(t) \geq z \geq 0
 \end{aligned}$$

where H_0 and h_0 are given by their modern values. Particle trajectories were numerically tracked through the time-varying velocity field using the time stepping scheme of equations (9.5). Finally, thinning functions were determined from the resulting depth-age profiles (as discussed in section 9.2). Bounding thinning functions are calculated using vertical velocity profiles which are linear in depth (Nye, 1957) and quadratic in depth (Raymond, 1983).

Figure 9.9 shows the thinning functions which result from the time-varying ice thickness, which in turn, was driven by time-varying accumulation rates. Since the three different velocity profile models predict different depth-age profiles, corresponding features appear at different depths, but the conclusion is the same. When an

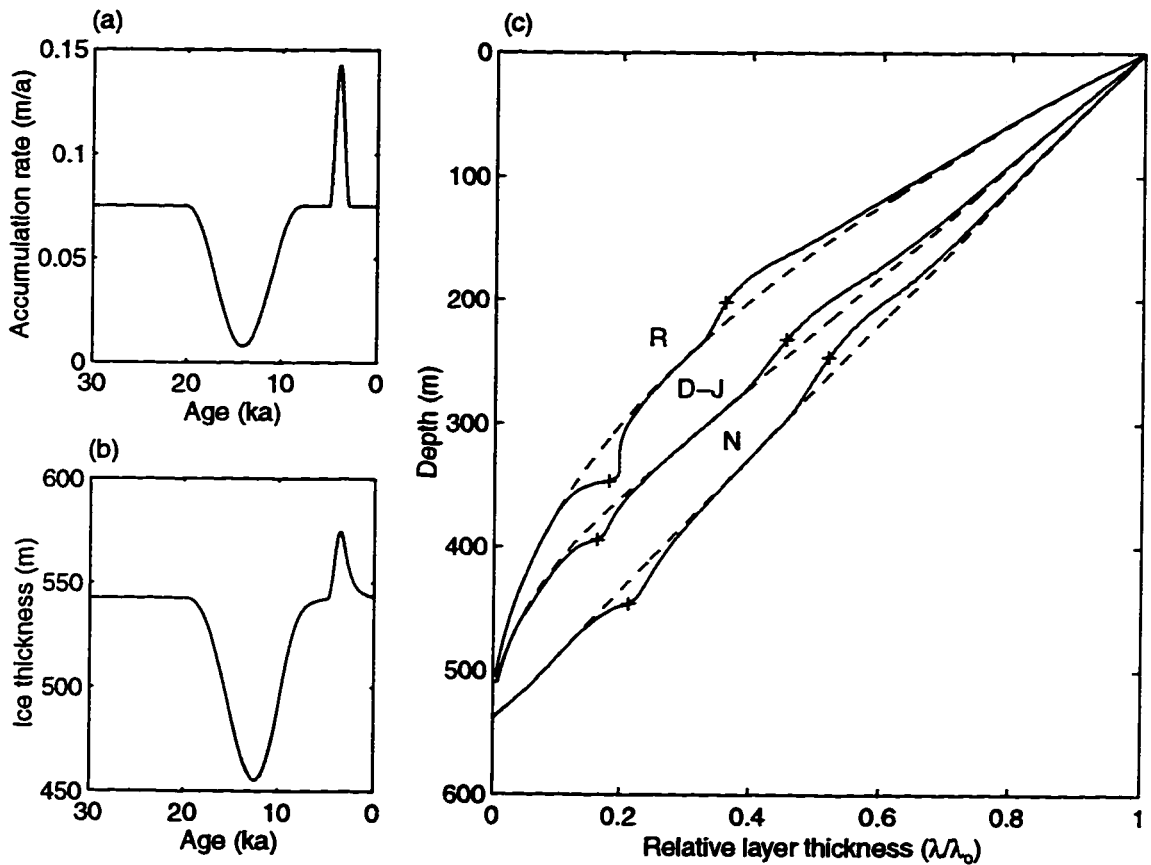


Figure 9.9: Thinning functions for time varying ice sheet thickness driven by accumulation rate variations. (a) Imposed accumulation rate history. (b) Ice thickness response. (c) Resulting Nye, Raymond, and Dansgaard-Johnsen thinning functions. The "+" symbols on these curves indicate depths corresponding to the ages of the accumulation rate maxima/minima.

accumulation rate low (high) occurs, the ice sheet thickness response causes thicker (thinner) layers at the corresponding depth. This is the opposite of what is required to match the thinning functions implied by believing the geochemical accumulation rates indicators; they require exceedingly small thinning functions for the low-accumulation rate LGM period.

9.4.4 Determination of accumulation rate consistent with time scale and ice sheet thickness variations

In the previous section (9.4.3), I estimated the ice sheet thickness response to accumulation rate variations and showed that the resulting thinning functions are inconsistent with those required by the minimizations of the penultimate section (9.4.2). This analysis brings up the question: how sensitive is the accumulation rate history inferred in section 9.4.1 to ice thickness variations? I couple the thickness response model with the accumulation rate inversion of section 9.4.1 to derive an accumulation rate history which agrees with the correlation timescale, and which has time-varying ice sheet thickness. I use a Dansgaard-Johnsen vertical thinning profile as discussed above. The resulting thinning functions and accumulation rate profile are shown in figure 9.10. Compared with the accumulation rate profile of section 9.4.1, these rates are somewhat lower, but the difference is not significant considering the model uncertainty.

9.5 Discussion

In this chapter I present the result of finite element modeling calculations and compare these for consistency with the ages determined from the stratigraphy and with geochemically determined accumulation rates. The analysis of the layer thickness section (9.3) confirmed the solar-cycle layer thickness measurements and suggested that the modern accumulation rate of 0.07 m/a was approximately constant through the

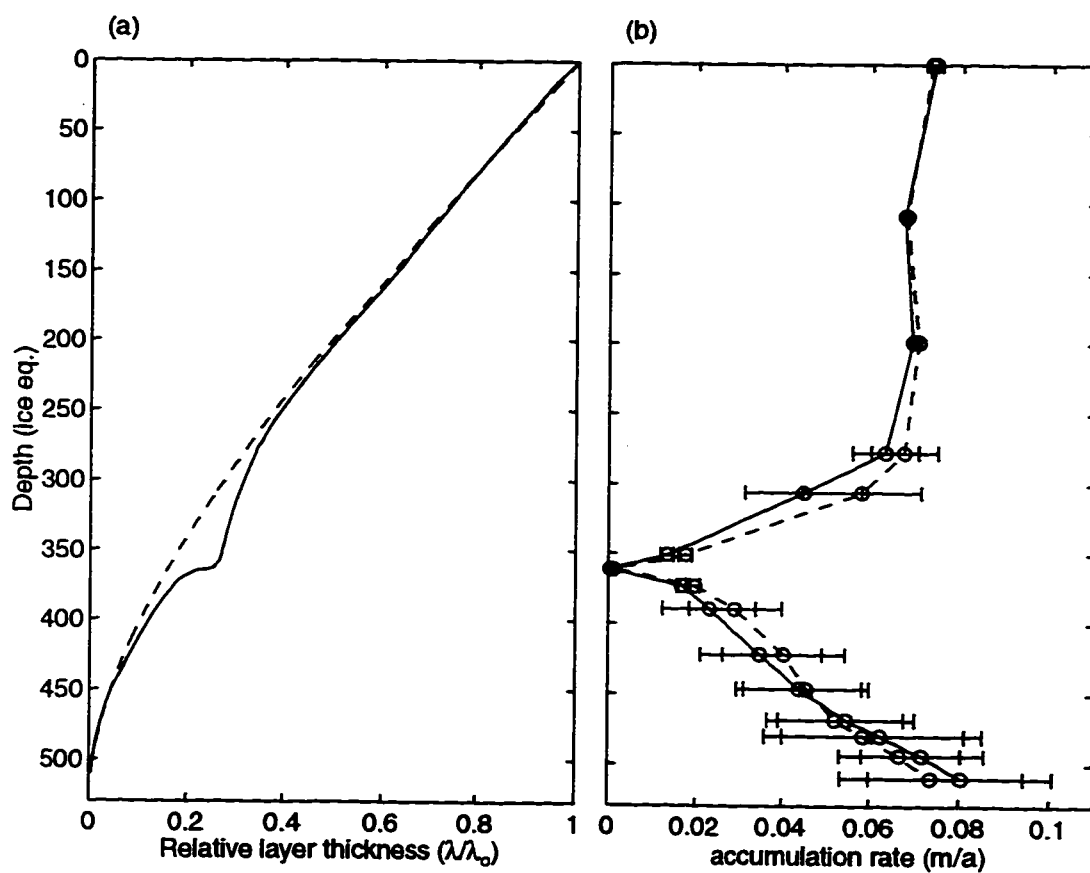


Figure 9.10: Thinning function (a) and accumulation rate profile (b) allowing for ice sheet thickness evolution (solid line) compared with constant thickness case (dashed).

Holocene. In the next section, the geochemically-determined accumulation rate profile and the timescale are shown to agree mostly very well, except in two sections. In the early Holocene, ^{10}Be measurements suggest erroneously high accumulation rates, and during the LGM, the time scale requires much lower accumulation rates than are predicted by ^{10}Be or SO_4^{2-} concentration profiles. I showed that the accumulation rate inferred from the thinning function and the timescale were relatively insensitive to “reasonable” time-varying flow field, thus either the timescale estimates, or the geochemically determined accumulation rates are wrong. Since the timescale estimates are mutually consistent, and are derived from four different chemical properties, I tend the latter hypothesis, and question the geochemically determined accumulation rate profile during this low-accumulation rate period.

Chapter 10

THE NORTHERN-FLANK VIRTUAL ICE CORE

The agreement of the geochemically-determined accumulation rates with those inferred from the timescale and the flow model (figure 9.6) largely confirm the ^{10}Be -snow accumulation rate technique. A surprising result of the ^{10}Be -derived accumulation rate profile was the very low LGM values (Steig, 1996). The LGM accumulation rate was reduced by a factor of five relative to the Holocene. This is in contrast to the factor of about 2.5 accumulation rate reduction observed at Byrd, Dome C, and Vostok (Jouzel, 1989; Hammer *et al.*, 1994). The primary difference between the inferred and the ^{10}Be snow accumulation rate profile is during LGM period. The inferred accumulation rates were lower still, near-zero in fact. A problem with geochemical accumulation rate proxies, such as ^{10}Be concentration, is that the method only works for positive mass balance. Obviously, the species must be preserved. The fidelity of the climate record at Taylor Dome has been a concern since the project's inception. In modern conditions, the accumulation is a tenuous balance between two competing weather states. The scouring action of the Katabatic flow system was likely even more effective during the more arid conditions of the LGM. Does the discrepancy between these accumulation rate profiles during the LGM indicate that net ablation occurred at the core site during the LGM?

An important lesson of the recent companion ice cores, GRIP and GISP2, is that, by combining the results of two nearby ice cores, a record can be obtained which is greater than the sum of its parts. A second ice core at Taylor Dome could address the question of LGM mass-loss. Such an ice core has not been drilled, but the radar data can provide clues as to what such a core might reveal.

The flowline-parallel radar profile (figure 2.5) shows a complex pattern of radar internal layering. In section 8.2, I show that the relative spacing of near-surface radar internal layers provides information on spatial patterns of accumulation rate. Consistency between the flow modeling results, the radar layering, and accumulation rate measurements establish that these layers are isochrons. In the preceding chapter, I show that absolute accumulation rates can be inferred from timescale estimates combined with flow modeling. By assuming that the deeper radar internal layers are also isochrons, timescales can be obtained throughout the profile by mapping the ice core site timescale along these layers. The internal layering pattern revealed in the flowline-parallel radar profile is highlighted by shading selected sections with common-ages. This is shown in figure 10.1. The ages of these bands are shown in the figure by comparison with the ice core $\delta^{18}\text{O}$ profile. The relative thickness of the uppermost band clearly shows the strong modern north-south accumulation rate gradient. Compared with the other shaded bands however, the LGM section appears to be relatively thicker to the north, and thinner to the south.

Ice from the LGM period is shallower on the north side of the dome. The section of LGM ice northward of about km 15 is thicker than at the core site. Is the LGM layer thicker to the north because of decreased vertical strain (a flow effect) or because of a change in accumulation rate (a climatic effect)? I chose the site over the bedrock peak at about km 15 for a “hypothetical” north-flank ice core to address this question.

The ages of several prominent radar layers at the core site are shown mapped to their corresponding depths at km 15 in figure 10.2(a). In section 9.4.1, I inferred the accumulation rate profile at the ice core site from the stratigraphic timescale. This method was applied at the north-flank site using the radar-interpolated ages as control points. The thinning function for this site was determined the same way as at the core site. The accumulation rate profile which is consistent with this timescale and thinning function is shown in figure 10.2(b). This profile is shown along with the corresponding ^{10}Be -determined snow accumulation rates. The agreement of the

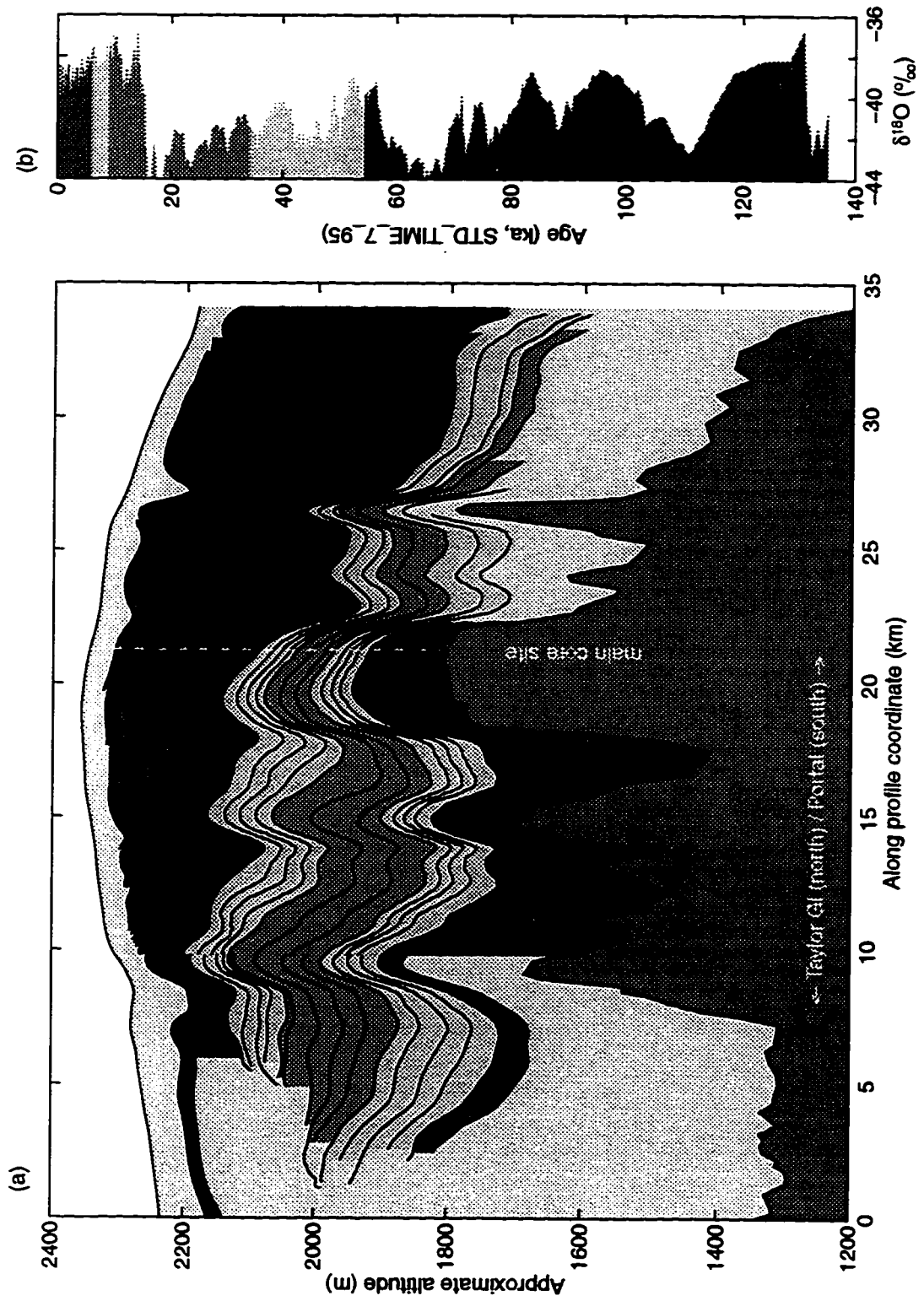


Figure 10.1: Radar internal layers painted by common age. Right panel shows $\delta^{18}\text{O}$ profile painted in same color scheme.

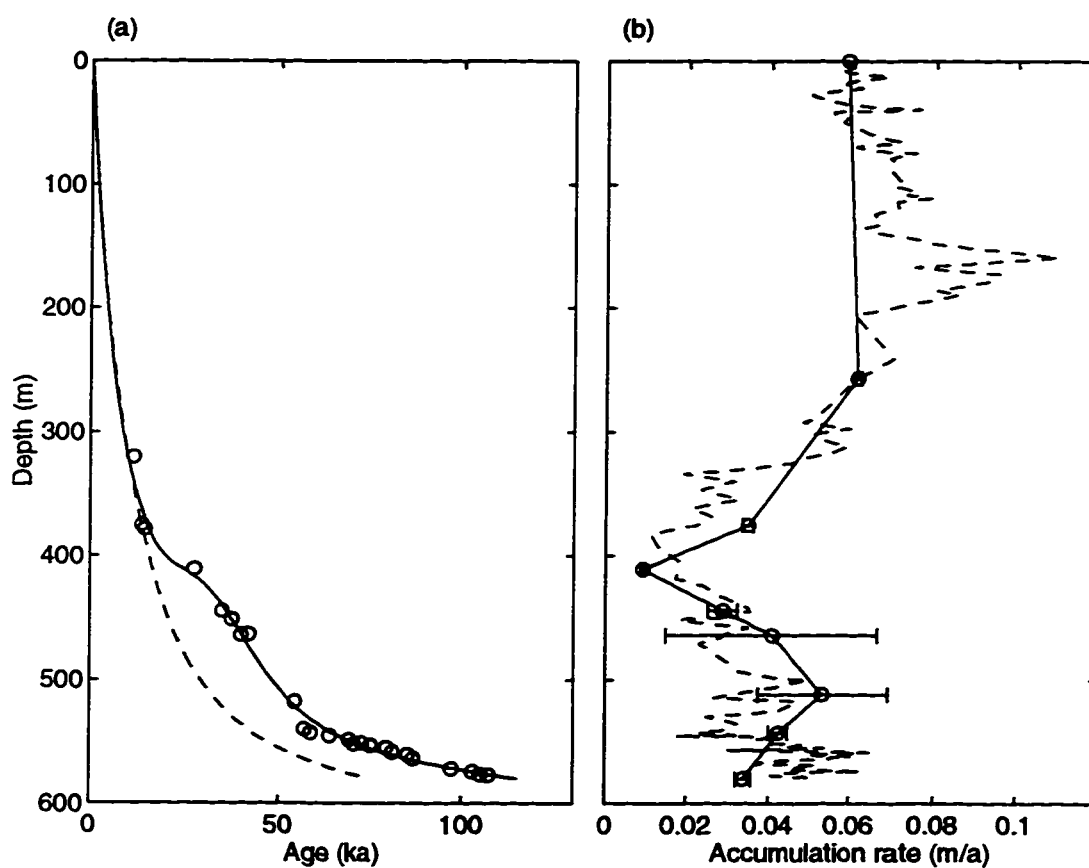


Figure 10.2: Accumulation rate profile inferred from timescale on northern flank. Panel (a): Circles are age control points mapped along radar layers from core site. The dashed line is the timescale predicted with the FEM for constant accumulation rate, and the solid line is the timescale predicted by accumulation rate profile shown with the solid line in panel (b). The dashed line in panel (b) is the core-site accumulation rates from ^{10}Be concentration interpolated along radar layers.

inferred accumulation rates with the ^{10}Be -determined accumulation rates over much of the depth is comparable to that at the core site (figure 9.6). At this site, the LGM interval is about 400 meters deep. The agreement in this interval is very good, in fact better than at the core site. The near-zero accumulation rates required by the age control points at the ice core site are not required here.

10.1 The ^{10}Be snow paléo-precipitation rate gauge

The modern accumulation rate of 0.07 m/a at the core site is a multi-year mean. The scatter of stake measurements (figure 5.4(c)) is about 0.04 m/a, *i.e.* about half the mean. The actual deposition in any individual year could be substantially more, or less. In some years, it may even be negative. The ^{10}Be method is conceptually reasonable for always-positive accumulation, and clearly it must fail for net ablation. The core-site accumulation rate discrepancy during the LGM may be an indication of failure of the ^{10}Be method at very low accumulation rates.

If the accumulation rate at a site were low, but always positive, then ^{10}Be would continue to be deposited at the surface (presumably sticking). The resulting relatively high ^{10}Be concentrations would be interpreted correctly as very low snow accumulation rates. On the other hand, if occasional episodes of ablation occur, then high surface ^{10}Be concentrations would be removed. The balance of accumulation rate with frequency and efficacy of erosion would determine an upper limit of ^{10}Be concentration, and thus a lower limit of inferred snow accumulation rate.

Another contributing effect could be reworking of surface snow. Erosion and redeposition would cause the ^{10}Be concentration of local snow to reflect a spatial average of accumulation rates at upwind locations. The area of averaging will depend on the distance of snow transport.

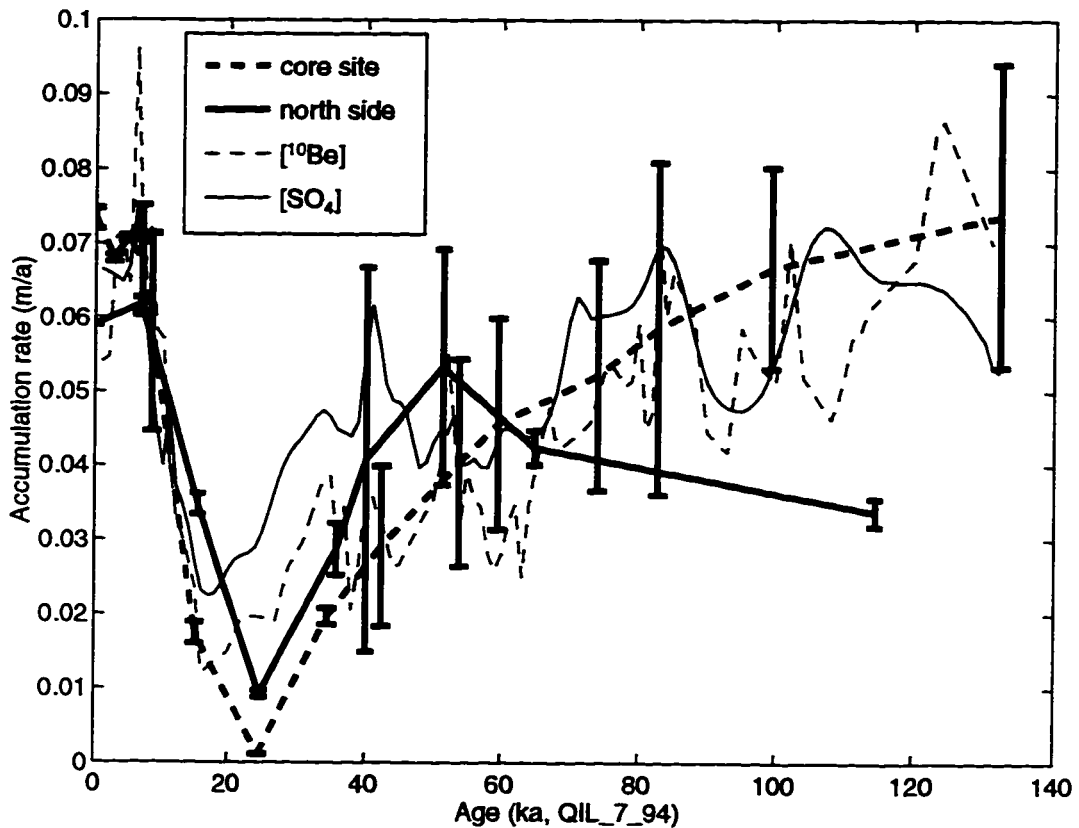


Figure 10.3: Comparison of accumulation rate histories inferred from timescale at core site and on northern flank.

10.2 Reversal of accumulation rate spatial gradient

In figure 10.1, the relative thickness of the uppermost band clearly shows the strong modern north–south accumulation rate gradient. Compared with the other shaded bands however, the LGM section appears to be relatively thicker to the north, and thinner to the south. The inferred accumulation rate profiles from the core site and the north-flank site are compared on a common timescale in figure 10.3. The geochemically-determined accumulation rate histories are also shown in the figure. Focusing on the record since about 60 kabp, an interesting pattern is evident. The modern accumulation rate gradient persisted through most of the Holocene. However,

the pattern was reversed for the period of ~15–40 kabp. The figure suggests that the accumulation rate was also higher to the south prior to 60 kabp, but this seems less certain given uncertainties with the inversion.

The modern condition at Taylor Dome is for the south side to have relatively higher accumulation rate than the north. This is the up-hill side of the dome for moisture-bearing storm systems which penetrate the Transantarctic Mountains to the south of the Royal Society Range. The pattern of radar internal layering suggests that the accumulation rate gradient was reversed during the LGM, suggesting that the direction of moisture-bearing storm tracks at the time was from the north. This would be a significant re-organization of synoptic-scale weather patterns. Is it reasonable to think that this has occurred?

The modern atmospheric circulation over the Ross Sea and Ross Ice Shelf is dominated by a persistent low pressure over the Ross Sea. Cyclonic systems arrive from the north-west and spiral rightward over the ice shelf, finally penetrating the Transantarctic Mtns. to the south of the Royal Society Range. The McMurdo Dry Valleys lie to the north of the Royal Society Range. It is speculated that they owe their snow-free nature to accumulation shadowing by the high peaks of the range. A working hypothesis of the group of Taylor Dome researchers, which goes back to the original proposal, is that an expanded Ross Ice Sheet would displace the Ross sea low northward, and block the passage of these systems, in effect, causing Taylor Dome to be in the accumulation shadow of the extended ice sheet. This is consistent with the “out of phase” (Drewry, 1980) response of the Dry Valleys geologic record, *i.e.* that the East Antarctic outlet glaciers advance into the Dry Valleys during interglacials and retreat during glacial periods. This response is supported by relatively high accumulation rates during interglacial periods and the very very low accumulation rates observed during the LGM. Steig (pers. comm.) attributed a drop in the ratio of Taylor Dome to Vostok ^{10}Be -derived accumulation rates at about 60 kabp to the advance of the Ross Ice Sheet.

A dilemma of the geologic record of the Dry Valleys, however, is the high stand of lakes which were dammed by the advanced Ross Ice Sheet. It is thought that high lake levels occur during more "humid" periods, and the low levels during "arid" periods (Lawrence and Hendy, 1985). Why did lakes form during the arid LGM? Several hypothesis have been advanced, including basal flow from the ice sheet (Denton *et al.*, 1985, 1989) and surface runoff from the ice sheet (Stuiver *et al.*, 1981). Perhaps the answer lies in the reversed moisture-bearing storm track directions suggested by the Taylor Dome radar layer data. A tantalizing clue is in the timing of cessation of the storm reversal period. Thus far I have loosely referred to the reversal period as "LGM"; however, inspection of the corresponding anomalous band in figure 10.1 shows that in fact the period continues well into the Holocene. The cessation appears to occur about two thousand years prior to the decline of $\delta^{18}\text{O}$ values near 6 kabp. Because the temporal resolution of the inferred accumulation rates is poor, these events cannot be reliably distinguished. Together, these events seem to be synchronous with the retreat of the expanded Ross Ice Sheet from the McMurdo sound region (Stuiver *et al.*, 1981). The change in $\delta^{18}\text{O}$ may be related to changes in air mass trajectories or to changes in ocean source regions. A change of accumulation rate may also be related to a change in moisture source region. However the change of storm track direction is probably physically linked to the position of the ice sheet.

Chapter 11

SYNOPSIS

An extensive program of geophysical observations were carried out at Taylor Dome. The first three chapters discuss the collection and reduction of morphological data. Ground radar profiles were collected along orthogonal grid-lines to facilitate mapping of bedrock and internal layers. Once surface topography and ice motion were known, then a radar profile was collected along a flowline that passes through the ice core site. These data provided high resolution maps of internal layer and bed topography in the vicinity of the core site. Regional surface and bed topography was provided by an airborne survey. A strain net was established to provide ice motion to constrain later ice dynamics modeling. The array was re-surveyed in sections over several seasons by both optical and GPS techniques. I presented a new algorithm to combine these disparate data types, and formed a simultaneous solution of the pole positions and velocities.

Thermal modeling, presented in the fourth chapter completes the “glaciological setting” of Taylor Dome. This is a transitional chapter between direct measurement of physical parameters, and calculation of derived quantities. Both surface and borehole temperatures, combined with accumulation rate measurements were used to model ice temperatures throughout the survey area. These results were used to reexamine the thermal regime of the sites identified as subglacial lakes by Drewry (1982), and to specify the temperature dependent ice rheological rate factor in later calculations.

In the following two chapters, the surface and bed geometry, ice motion, and temperature data are combined in an inverse problem. A generalized formulation of Glen’s flow law is proposed which includes a crossover to linear behavior at low

stresses. The ice sheet geometry data, a simple ice dynamics model, and the proposed flow law are used to predict a surface velocity field. Fitting this with the measured surface velocities gives values for the underlying rheological parameters. First the inversion scheme is tested using synthetic geometry and motion data, *i.e.* the results from a numerical ice dynamics model. Then, inversion of the actual survey data indicated a value of 0.23 bar for the crossover stress at the divide.

The final chapters involve interpretation of the ice core results. Numerical flow modeling along the flowline-parallel radar profile is the central element of this analysis. With this model, I calculated the flowfield that is in steady-state with the modern geometry and accumulation rates. The vertical thinning function derived from this flow field is then used to support timescale estimates which were determined by stratigraphic correlation with other dated records. By then combining the thinning function and the timescale, an accumulation rate profile was inferred that was then compared with a profile determined by geochemical techniques. The comparison in general supported the geochemical results, but differed from it in two important points. First, the ^{10}Be -derived profile suggested high early Holocene accumulation rates which were not supported by the inferred profile. This discrepancy is attributed to ^{10}Be production rate variations. Second, the inferred profile suggested much lower accumulation rates than the ^{10}Be profile during the Last Glacial Maximum. This difference is attributed to failure of the ^{10}Be method at low accumulation rates. In the final chapter, the radar layers are used to interpolate the ice core timescale along the flowline-parallel profile. An accumulation rate profile was inferred at a site to the north of the divide. This analysis indicated that a significant reconfiguration of the local storm pattern occurred during the Last Glacial Maximum, which was attributed to a local climatic response to the advanced stand of the West Antarctic Ice Sheet.

11.1 Future work

The order of presentation in this dissertation was dictated by logical flow, rather than time-sequential fidelity. In fact the order that these analyses occurred is nearly reversed from their presentation. The finite element flow field, which is the foundation for the final analyses, was determined prior to obtaining the final velocity solution, and prior to the detailed thermal modeling. It turned out that the assumed temperature field was remarkably close to the later calculated result. The model rheology was tuned by matching the ice sheet geometry alone. The preferred “softening” parameter determined by this procedure was consistent with the parameters determined by matching the velocity field. Thus performing another suite of model runs was not warranted on this basis, though a new model run that included the linear rheology would be desirable. However, the effects of the linear rheology are primarily limited to within one ice thickness of the divide. Since the ice core was drilled approximately three ice thicknesses away, little difference to the ice core timescale analyses would be realized.

The very low LGM accumulation rates at the core site and the accumulation gradient reversal are robust results. Repeating any particular step of the analyses would achieve incremental improvement, but the conclusions would likely be unchanged. In any case, a modest gain would be achieved by returning to the flow-line modeling. I recommend using a “2.5-D” flow model to incorporate flow spreading around bed topography. This model should use the generalized Glen flow law, and be tuned to fit the surface topography, the surface velocity data, and the accumulation rate anomaly trajectories in combination. Repeating the timescale-accumulation rate profile analyses using thinning functions obtained from this velocity field might give a different north-flank LGM accumulation rate, which in turn may give a better ^{10}Be snow accumulation rate calibration.

BIBLIOGRAPHY

- Alley, R. B. (1992). Flow-law hypotheses for ice-sheet modeling. *Journal of Glaciology*, **38**(129), 245–256.
- Anandakrishnan, S., Fitzpatrick, J. J., Alley, R. B., Gow, A. J., and Meese, D. A. (1994). Shear wave detection of *c*-axis fabrics in the GISP2 ice core, Greenland. *Journal of Glaciology*, **40**(136), 491–495.
- Anderson, J. B., Shipp, S. S., Bartek, L. R., and Reid, D. E. (1992). Evidence for a grounded ice sheet on the Ross Sea continental shelf during the Late Pleistocene and preliminary paleodrainage reconstruction. In D. H. Elliot, editor, *Contributions to Antarctic research III*, pages 39–62. American Geophysical Union, Washington D.C. (Antarctic Research Series 57).
- Azuma, N. (1994). A flow law for anisotropic ice and its application to ice sheets. *Earth and Planetary Science Letters*, **128**(3–4), 601–614.
- Barrett, P. J., Adams, C. J., McIntosh, W. C., Swisher III, C. C., and Wilson, G. S. (1992). Geochronological evidence supporting Antarctic deglaciation three million years ago. *Nature*, **359**, 816–818.
- Bindschadler, R. A., Harrison, W. D., Raymond, C. F., and Crosson, R. (1977). Geometry and dynamics of a surge-type glacier. *Journal of Glaciology*, **18**(79), 181–194.
- Blankenship, D. D., Bell, R. E., and the CASERTZ group (1994). Corridor aerogeophysics in the Interior Ross Embayment of West Antarctica. *Terra Antarctica*, **1**(3), 507–508.

- Bogorodsky, V. V., Bentley, C. R., and Gudmansen, P. E. (1985). *Radioglaciology*. D. Reidel.
- Broecker, W. S., Peteet, D., and Rind, D. (1985). Does the ocean-atmosphere system have more than one stable mode of operation? *Nature*, **315**, 21–25.
- Budd, W. F. (1968). The longitudinal velocity profile of large ice masses. *IAHS*, **79**, 58–75.
- Budd, W. F. and Jacka, T. H. (1989). A review of ice rheology for ice sheet modeling. *Cold Regions Science and Technology*, **16**, 107–144.
- Clow, G. D. and Waddington, E. D. (1996). Acquisition of borehole temperature measurements from Taylor Dome and the Dry Valleys for paleoclimate reconstruction. *Antarctic Journal of the U.S.* (in press).
- Cuffey, K. M., Clow, G. D., Alley, R. B., Stuiver, M., Waddington, E. D., and Saltus, R. W. (1995). Large arctic temperature change at the Wisconsin-Holocene glacial transition. *Science*, **270**, 455–458.
- Cutler, N. A., Raymond, C. F., Waddington, E. D., Meese, D. A., and Alley, R. B. (1995). The effect of ice sheet thickness change on the accumulation history inferred from GISP2 layer thicknesses. *Annals of Glaciology*, **21**, 26–32.
- Dansgaard, W. and Johnsen, S. J. (1969). A flow model and a time scale for the ice core from Camp Century, Greenland. *Journal of Glaciology*, **8**(53), 215–223.
- Decker, E. R. and Bucher, G. J. (1982). Geothermal studies in the Ross Island-Dry Valley region. In C. Craddock, editor, *Antarctic Geoscience*, pages 887–894. International Union of Geological Sciences.

- Denton, G. H., Armstrong, R. L., and Stuiver, M. (1985). Radiocarbon chronology of the last glaciation in McMurdo Sound, Antarctica. *Antarctic Journal of the U.S.*, **19**, 59–61.
- Denton, G. H., Blockheim, J. G., Wilson, S. C., and Stuiver, M. (1989). Wisconsin and early Holocene Glacial history, Inner Ross Embayment, Antarctica. *Quaternary Research*, **31**, 151–182.
- Drewry, D. J. (1980). Pleistocene bimodal response of Antarctic ice. *Nature*, **287**(5997), 214–216.
- Drewry, D. J. (1982). Ice flow, bedrock, and geothermal studies from radio-echo sounding inland of McMurdo Sound, Antarctica. In C. Craddock, editor, *Antarctic Geoscience*, pages 977–983. International Union of Geological Sciences.
- Drewry, D. J. (1983). Antarctica: Glaciological and Geophysical Folio. Technical report, Scott Polar Research Institute, Cambridge.
- Firestone, J. F., Waddington, E. D., and Cunningham, J. (1990). The potential for basal melting under Summit, Greenland. *Journal of Glaciology*, **36**(123), 163–168.
- Fitzpatrick, J. J. (1994). Preliminary report on the physical and stratigraphic properties of the Taylor Dome ice core. *Antarctic Journal of the U.S.*, **29**(5), 84–86.
- Fujita, S. and Mae, S. (1993). Relation between ice sheet internal echo reflections and ice fabric at Mizuho Station, Antarctica. *Annals of Glaciology*, **17**, 269–275.
- Fujita, S. and Mae, S. (1994). Causes and nature of ice-sheet radio-echo internal reflections estimated from the dielectric properties of ice. *Annals of Glaciology*, **20**, 80–86.
- Glen, J. and Paren, J. (1975). The electrical properties of snow and ice. *Journal of Glaciology*, **15**(73), 15–38.

- Grotes, P. M., Steig, E. J., Stuiver, M., Waddington, E. D., and Morse, D. L. (1996). New 130,000 year climate record from Taylor Dome, Antarctica shows rapid global climate fluctuations and dynamic Antarctic ice age climate. in prep.
- Gudmandsen, P. E. (1975). Layer echos in polar ice sheets. *Journal of Glaciology*, **15**(73), 95–101.
- Hammer, C. U., Clausen, H. B., and Langway, Jr., C. C. (1994). Electrical conductivity method (ECM) stratigraphic dating of the Byrd Station ice core, Antarctica. *Annals of Glaciology*, **20**, 115–120.
- Harrison, C. H. (1973). Radio echo sounding of horizontal layers in ice. *Journal of Glaciology*, **12**(66), 383–397.
- Hughes, T. (1973). Is the West Antarctic Ice Sheet disintegrating? *Journal of Geophysical Research*, **78**(33), 7884–7910.
- Hutter, K., Legerer, F., and Spring, U. (1981). First-order stresses and deformations in glaciers and ice sheets. *Journal of Glaciology*, **27**(96), 227–270.
- Jóhannesson, T. (1992). *Landscape of temperate ice caps*. Ph.D. thesis, Univ. of Washington.
- Jouzel, J. (1989). A comparison of deep Antarctic ice cores and their implications for climate between 65,000 and 15,000 years ago. *Quaternary Research*, **31**(2), 135–150.
- Jouzel, J., Barkov, N. I., Barnola, J. M., Bender, M., Chappellaz, J., Genthon, C., Kotlyakov, V. M., Lipenkov, V., Lorius, C., Petit, J. R., Raynoud, D., Raisbeck, G., Ritz, C., Sowers, T., Sievenhard, M., Yiou, F., and Yiou, P. (1993). Extending the Vostok ice-core record of paleoclimate to the penultimate glacial period. *Nature*, **364**, 407–411.

- Kamb, B. and Echelmeyer, K. A. (1986). Stress-gradient coupling in glacier flow: I. longitudinal averaging of the influence of ice thickness and surface slope. *Journal of Glaciology*, **32**(111), 267–284.
- Kellogg, T. B., Hughes, T. J., and Kellogg, D. E. (1996). Late Pleistocene interactions of East and West Antarctic ice flow regimes: evidence from the McMurdo Ice Shelf. *Journal of Glaciology*, **42**(142), 486–500.
- Lawrence, M. J. F. and Hendy, C. H. (1985). Water column and sediment characteristics of Lake Fryxell, Taylor Valley, Antarctica. *New Zealand Journal of Geology and Geophysics*, **28**(3), 543–552.
- Lliboutry, L. A. and Duval, P. (1985). Various isotropic and anisotropic ices found in glaciers and polar ice caps and their corresponding rheologies. *Annals of Geophysics*, **3**, 207–224.
- Manabe, S. and Broccoli, A. J. (1985). The influence of continental ice sheets on the climate of an ice age. *Journal of Geophysical Research*, **90**(D1), 2167–2190.
- McHargue, L. R. and Damon, P. E. (1991). The global beryllium 10 cycle. *Rev. Geophys.*, **29**(2), 141–158.
- McHargue, L. R., Damon, P. E., and Donahue, D. J. (1995). Enhanced cosmic ray production of $\delta^{10}\text{Be}$ coincident with the Mono Lake and Laschamp geomagnetic excursions. *Geophysical Research Letters*, **22**, 659–662.
- Meese, D. A., Alley, R. B., Gow, A. J., Grootes, P. M., Mayewski, P. A., Ram, M., Taylor, K. C., Waddington, E. D., and Zielinski, G. (1994). Preliminary Depth-Age Scale of the GISP2 Ice Core. Technical Report 94-1, CRREL.
- Menke, W. (1989). *Geophysical Data Analysis, Discrete Inverse Theory*, volume 45 of *International Geophysics Series*. Academic Press.

- Millar, D. H. M. (1981). Radio-echo layering in polar ice and past volcanic activity. *Nature*, **292**, 441–443.
- Moore, J. C. (1988). Dielectric variability of a 130m Antarctic ice core: implications for radar sounding. *Journal of Glaciology*, **11**, 95–99.
- Morse, D. L. and Waddington, E. D. (1992). Glacier geophysical studies for an ice core site at Taylor Dome: year two. *Antarctic Journal of the U.S.*, **27**(5), 59–61.
- Morse, D. L. and Waddington, E. D. (1994). Recent survey of brine infiltration in McMurdo Ice Shelf, Antarctica. *Annals of Glaciology*, **20**, 215–218.
- Neal, C. S. (1976). Radio-echo power profiling. *Journal of Glaciology*, **17**(77), 527–530.
- Nereson, N. A., Waddington, E. D., Raymond, C. F., and Jacobson, H. P. (1996). Predicted age-depth scales for Siple Dome and inland WAIS ice cores in west Antarctica. *Geophysical Research Letters*, **23**(22), 3163–3166.
- Nye, J. F. (1957). The distribution of stress and velocity in glaciers and ice-sheets. *Proceedings of the Royal Society of London, Ser A*, **239**(1216), 113–133.
- Oeschger, H., Beer, J., Siegenthaler, U., Stauffer, B., Dansgaard, W., and Langway, C. C. (1984). Late glacial climate history derived from ice cores. In J. E. Hansen and T. Takahashi, editors, *Climate Processes and Climate Sensitivity*, pages 299–306. American Geophysical Union. Geophysical Monograph 29.
- Paren, J. G. and Robin, G. (1975). Internal reflections in polar ice sheets. *Journal of Glaciology*, **14**(71), 251–259.
- Parker, R. L. (1994). *Geophysical Inverse Theory*. Princeton University Press, 1st edition.

- Paterson, W. S. B. (1994). *The Physics of Glaciers*. Pergamon Press, Oxford, 3rd edition.
- Paterson, W. S. B. and Clarke, G. K. C. (1978). Comparison of theoretical and observed temperature profiles in Devon Island ice cap, Canada. *Geophys. J. R. Astr. Soc.*, **55**, 615–632.
- Phillips, N. A. (1957). A coordinate system having some special advantages for numerical forecasting. *Journal of Meteorology*, **14**, 184–185.
- Picciotto, E. A. and Wilgain, S. (1963). Fission products in Antarctic snow, a reference level for measuring accumulation. *Journal of Geophysical Research*, **68**(21), 979–987.
- Rasmussen, A. L. (1986). Refraction correction for radio-echo soundings of ice overlain by firn. *Journal of Glaciology*, **32**(111), 192–194.
- Raymond, C. F. (1983). Deformation in the vicinity of ice divides. *Journal of Glaciology*, **29**(103), 357–373.
- Raymond, C. F. (1996). Shear margins in glaciers and ice sheets. *Journal of Glaciology*, **42**(140), 90–102.
- Remondi, B. W. (1984). Using the Global Positioning System phase observable for relative geodesy. Technical report, NOAA, Rockville, MD.
- Robin, G. (1955). Ice movement and temperature distribution in glaciers and ice sheets. *Journal of Glaciology*, **2**(18), 523–532.
- Schøtt, C., Waddington, E., and Raymond, C. F. (1992). Predicted time-scales for GISP2 and GRIP boreholes at Summit, Greenland. *Journal of Glaciology*, **38**(128), 162–168.

- Shackleton, N. J. (1987). Oxygen isotopes, ice volume and sea level. *Quaternary Science Reviews*, **6**, 183–190.
- Steig, E. J. (1996). *Beryllium-10 in the Taylor Dome ice core: Applications to Antarctic Glaciology and Paleoclimatology*. Ph.D. thesis, Univ. Washington.
- Steig, E. J., Polissar, P. J., Stuiver, M., Grootes, P. M., and Finkel, R. (1996). Large amplitude solar modulation of ^{10}Be in Antarctica: implications for atmospheric mixing processes and interpretation of the ice core record. *Geophysical Research Letters*, **23**(5), 523–526.
- Steig, E. J., Morse, D. L., and Waddington, E. D. (1997). Using the sunspot cycle to date ice cores. Submitted.
- Stuiver, M., Denton, G. H., Hughes, T. J., and Fastook, J. L. (1981). The history of the marine ice sheet in West Antarctica: A working hypothesis. In G. H. Denton and T. J. Hughes, editors, *The Last Great Ice Sheets*, pages 319–436. Wiley, New York.
- Sugden, D. E., Marchant, D. R., and Denton, G. H., editors (1993). *The Case for the Stable East Antarctic Ice Sheet*, *Geographisca Annaler*, volume 75A, no. 4. Scandanavian University Press.
- Taylor, K. C., Morse, D. L., and Jacobel, R. W. (1996). On the use of ice core paleoclimate electrical measurements for modeling ice-penetrating radar profiles. in prep.
- USGS (1975). Taylor Glacier 1:250000 Satellite image map. 77198-S1-SI-250.
- Vialov, S. S. (1958). Regularities of glacial shield movement and the theory of plastic viscous flow. *International Association of Hydrological Sciences*, **47**, 266–275.

- Waddington, E. D. and Morse, D. L. (1994). Spatial variations of local climate at Taylor Dome, Antarctica: implications for paleoclimate from ice cores. *Annals of Glaciology*, **20**, 219–225.
- Waddington, E. D. and Rasmussen, L. A. (1993). Inferring a velocity field from basic stake measurements. in preparation.
- Waddington, E. D., Morse, D. L., Balise, M. J., and Firestone, J. (1991). Glacier geophysics for an ice core site at Taylor Dome. *Antarctic Journal of the U.S.*, **26**(5), 71–73.
- Waddington, E. D., Morse, D. L., Grootes, P. M., and Steig, E. J. (1993). The connection between ice dynamics and paleoclimate from ice cores: a study of Taylor Dome, Antarctica. In W. R. Peltier, editor, *Ice in the Climate System*, volume 12 of *NATO ASI series I*, pages 499–516. Springer-Verlag.
- Waddington, E. D., Raymond, C. F., Morse, D. L., and Harrison, W. F. (1996). Flow law for ice at low deviatoric stress, and implications for ice divide and ice core studies. EOS 77(46), Fall Meeting Supplement, F196 (abstract).
- Watts, R. D. and Wright, D. L. (1981). Systems for measuring thickness of temperate and polar ice from the ground or from the air. *Journal of Glaciology*, **27**(97), 459–469.
- Weertman, B. R. (1993). *Interpretation of Ice Sheet Stratigraphy: A radar-echo sounding study of the Dyer Plateau, Antarctica*. Ph.D. thesis, University of Washington.
- Weertman, J. (1973). Creep of ice. In E. Whalley, S. J. Jones, and L. W. Gold, editors, *Physics and Chemistry of Ice*, pages 320–337. Royal Society of Canada, Ottawa.

- Weertman, J. (1974). Stability of the junction of an ice sheet and ice shelf. *Journal of Glaciology*, **13**(67), 3–11.
- Wessel, P. and Smith, W. H. F. (1995). New version of the Generic Mapping Tools released. *EOS*, **76**, 329.
- Whillans, I. M. (1976). Radio-echo layers and the recent stability of the West Antarctic Ice Sheet. *Nature*, **264**, 152–155.
- Wilson, T. J. and Bradford, S. C. (1993). Satellite-image analysis of the Transantarctic Mountains, southern Victoria Land. *Antarctic Journal of the U.S.*, **28**(5), 23–26.

Appendix A

RADIATION IN DIELECTRIC MEDIA

The following is a brief review of electromagnetic radiation which can be found in any undergraduate E&M text. The governing equations of classical electrodynamics are collectively termed Maxwell's Equations, which in the SI system of units are:

$$\nabla \cdot \mathbf{D} = \rho \quad (\text{A.1})$$

$$\nabla \cdot \mathbf{B} = 0 \quad (\text{A.2})$$

$$\nabla \times \mathbf{E} = -\frac{\partial}{\partial t} \mathbf{B} \quad (\text{A.3})$$

$$\nabla \times \mathbf{H} = \frac{\partial}{\partial t} \mathbf{D} + \mathbf{J} \quad (\text{A.4})$$

where \mathbf{E} and \mathbf{H} are the electric and magnetic fields, respectively. The constitutive relations are $\mathbf{D} = \tilde{\epsilon} \mathbf{E}$, and $\mathbf{B} = \tilde{\mu} \mathbf{H}$, where ϵ and μ are the electric permittivity and magnetic permeability, respectively. Current in a conducting media is given by Ohm's Law

$$\mathbf{J} = \tilde{\sigma} \mathbf{E} \quad (\text{A.5})$$

where σ is the conductivity. In this review, vector fields are written in boldface-type (\mathbf{E}), vector components are subscripted (E_z), tensor quantities appear in tilde-boldface ($\tilde{\epsilon}$), and complex quantities are designated with a "hat" ($\hat{\epsilon}$).

First I will consider propagation of plane waves in the $+z$ direction in a linear, isotropic, non-conducting medium with no free charges, i.e. an ideal dielectric. By assuming sinusoidal time dependence ($\mathbf{E}(\mathbf{x}, t) \propto \exp(-i\omega t)$), combining (A.3) with (A.4) and making use of the scalar form of the constitutive relations yields a

wave equation.

$$\nabla^2 \mathbf{E} + \omega^2 \mu \epsilon \mathbf{E} = 0 \quad (\text{A.6})$$

which has a solution given by

$$E_z(\mathbf{x}, t) = E_0 \exp \left[-i\omega \left(t - \frac{n_0}{c} z \right) \right].$$

In this form, the phase velocity, $v = \frac{1}{\sqrt{\mu\epsilon}}$, is written in terms of the speed of light in a vacuum $c \equiv \frac{1}{\sqrt{\mu_0\epsilon_0}}$, and an index of refraction n_0 .

In a conductive dielectric which obeys Ohm's law, the wave equation (A.6) becomes

$$\nabla^2 \mathbf{E} + \omega^2 \mu \hat{\epsilon} \mathbf{E} = 0$$

where $\hat{\epsilon} = \epsilon + \frac{\sigma}{j\omega}$ may be viewed as a complex permittivity. This has a solution

$$E_z(\mathbf{x}, t) = E_0 \exp \left[-i\omega \left(t - \sqrt{\mu \hat{\epsilon}} z \right) \right].$$

Expanding the complex permittivity, this becomes

$$E_z(\mathbf{x}, t) = E_0 \exp \left(-\frac{\omega k}{c} z \right) \exp \left[-i\omega \left(t - \frac{n}{c} z \right) \right] \quad (\text{A.7})$$

where,

$$\begin{pmatrix} n \\ k \end{pmatrix} = \frac{n_0}{\sqrt{2}} \left[\left(1 + \frac{\sigma^2}{\epsilon^2 \omega^2} \right)^{\frac{1}{2}} \pm 1 \right]^{\frac{1}{2}}$$

The form of (A.7) may be simplified in two limits. For good conductors:

$$\frac{\sigma}{\epsilon\omega} \gg 1, \quad n = k = n_0 \left(\frac{\sigma}{2\epsilon\omega} \right)^{\frac{1}{2}}.$$

And for poor conductors:

$$\frac{\sigma}{\epsilon\omega} \ll 1, \quad n = n_0, \quad k = \frac{n_0 \sigma}{2\epsilon\omega}.$$

For reference, seas water at 5 MHz gives $(\sigma/\epsilon\omega \approx 7000 \gg 1)$.

Reflection from dielectric interfaces

The Fresnel reflection equations for dielectric interfaces are applicable to radar sounding of glacial ice in two forms. Reflections from a smooth bed can be described by a single dielectric interface (the half-space model). Internal reflectors may be thought of as thin dielectric layers embedded within another dielectric (the thin layer model).

Following the standard treatment found in any optics or E&M text, the amplitude reflection coefficient \hat{r} of plane waves at normal incidence to a dielectric interface is given by the difference of the index of refraction of the two media (subscripted 1 and 2, respectively) divided by their sum. Here I have generalized the form to allow both materials to be lossy dielectrics.

$$\hat{r}_{12} = \frac{\hat{n}_2 - \hat{n}_1}{\hat{n}_2 + \hat{n}_1} = \frac{(n_2 - n_1) + i(k_2 - k_1)}{(n_2 + n_1) + i(k_2 + k_1)}$$

writing this in polar phasor form

$$\hat{r}_{12} = |\hat{r}_{12}| \exp(i\phi), \quad |\hat{r}_{12}|^2 = \frac{(n_2 - n_1)^2 + (k_2 - k_1)^2}{(n_2 + n_1)^2 + (k_2 + k_1)^2}, \quad \tan\phi = \frac{2(n_1 k_2 - n_2 k_1)}{n_2^2 - n_1^2 + k_2^2 - k_1^2}$$

where $|\hat{r}_{12}|^2 \equiv R_{12}$ is the power reflection coefficient (PRC).

Reflection from a conducting layer embedded in a dielectric is the superposition of reflections from both interfaces. If the dielectrics are poor conductors, the attenuation within the conducting layer and phase change from transmission through the first interface can be neglected. The PRC is given by

$$R_{121} = 4 \sin^2 \left(\frac{2\omega n_0 d}{c} \right) R_{12}.$$

The sine term accounts for the phase lag of the wave reflected from the second interface relative to the first (Paren and Robin, 1975). The PRC of a layer can range between 0 and 4 times (6 dB) the PRC of the half-space interface depending upon the thickness of the layer. Typically, the layer is thin compared to wavelengths, so this can be further approximated as

$$R_{121} = 16 \left(\frac{\omega n_0 d}{c} \right)^2 R_{12}.$$

VITA

Name: David L. Morse

Date: August 12, 1997

Education

B. Sc.: Physics, California Polytechnic, 1987

M. Sc.: Geophysics, University of Washington, 1990

Ph. D.: Geophysics, University of Washington, 1997

Thesis Titles

B. Sc.: Total vector analysis of the Olduvai Termination Geomagnetic Field Reversal from Molokai, Hawaii.

M. Sc.: Charge Neutralization of a Current emitting Rocket Payload: ESA Particle measurements from BEAR.

Ph. D.: Glacier Geophysics at Taylor Dome, Antarctica